The new version of the Radiation Monitor system for the electronics at the CERN : electronic components radiation hardness assurance and sensors qualication

Salvatore Danzeca

THÈSE

Pour obtenir le grade de

Docteur

Délivré par l'**UNIVERSITE MONTPELLIER 2**

Préparée au sein de l'école doctorale **Information, Structures et Systèmes (I2S)**

Et de l'unité de recherche **Institut d'Électronique du Sud (IES)**

Spécialité: **Electronique**

Présentée par **Salvatore Danzeca**

The new version of the Radiation Monitor system for the electronics at CERN. Electronic components radiation hardness assurance and sensors qualification.

La nouvelle version du système de monitorage des radiaitons pour l'électronique au CERN. Garantie de tenue aux radiations des composants électroniques et qualification des capteurs.

Prof. Laurent Dusseau	UM2 I2S	Directeur
Dr. Giovanni Spiezia	CERN	Supervisor
Prof. Laurent Béchou	Université de Bordeaux	Rapporteur
Dr. Karine Castellani-Coullié	Université de d'Aix-Marseille	Rapporteur

Acknowledgments

This thesis is the results of three years of research at CERN, which for me has been an enriching and challenging experience.

I want to express a deep and sincere gratitude to my CERN supervisor, Giovanni Spiezia. He has been more than a mentor, a real friend. He supported me in all the activities and, with his wide knowledge, followed my work constantly. He gave me the opportunity to be autonomous, responsible and to grow up as a better engineer. I am thankful to him also for his big humanity and comprehension of all the problems, related or not to the work.

I want to express a sincere gratitude to my Professor in Montpellier, Laurent Dusseau. I felt always supported by him and my work has always been encouraged. His advices and support have always been important to me.

I am deeply grateful to the section leader Alessandro Masi who gave me the opportunity to work in his group on diverse exciting projects. He is a reference point for me, not only, on the technical side but also on the management side. His organization skill and attitude is really inspiring and this pushes me to give the best on all the projects I am involved in.

My gratitude goes also to the R2E project leader Markus Brugger. His outlook and ability to follow different projects are very inspiring. I am grateful for the responsibilities he gives to me and for the confidence placed in me.

Part of this work was possible also thanks to the fruitful collaboration with IC-Malaga and in particular to Alvaro Pineda and Joan Cesari. They really believe in the project we carry on and it is always a pleasure work with them.

Big thanks goes also to my friend and colleague Ruben. He is a very good friend and a really skilled physicist. His knowledge of radiation environments and radiation effects bring us to investigate on a myriad of components. We shared many really good moments at work and also outside.

I want to thank what I call “my second family” in Geneva: Riccardo, Rosario and Nicola. They supported me in all the moments of the day, from the first coffee in the morning up to the dinner. They make me a better person and I am grateful to have met them. The “Neapolitan Sunday” lunch with them is something that I will never forget.

I want to thank all my colleagues, Mario, Mark, Julien, Alessandro D. and Alessandro G., Clement , Gilles, Ricardo, Philippe, Ana Sofia, Alex, Thimotee. They create a very nice working environment and I love to work with them.

I want to thank my closest friends, without them, my life in Geneva would not be the same. Carlo, Raffo, Damiano, Francesca, Andrea, Fabrizio, Marcello, Stefano the time spent with them is invaluable. I hope that we will always be together.

Particular thanks goes to Paul Perronnard, who is the most skilled engineer I have ever met. Any questions or problems are solved thanks to his help and for him everything is possible. A big thanks goes also to another colleague and good friend, Christophe Mitifiot. The talks related to our common sport addiction are the things that lighten the hard office work. He is a great a person that I can always trust.

Finally, I would like to thank my parents Ester and Pasquale, my brother Francesco, my aunt Marina and my grandmothers Susy and Maria. They are always supporting me and encouraging me with their best wishes always pushing me to do the best.

Summary

The measurement of the radiation levels is an essential requirement in the LHC and its injection lines in order to quantify radiation effects on electronics and provide a detailed knowledge of the radiation field. The radiation monitoring system for the electronics at CERN, the "RadMon", was installed in critical areas where equipment is or will be placed. Issues experienced in the last years of Radmon operation, the obsolescence of a few fundamental components of the electronic board and the necessity to improve both the accuracy and the resolution of measurements led to the launch of a new design of the monitor.

This work describes the architecture of the new RadMon (V6), its reliability in radiation environments and the strategy adopted to choose and qualify the sensors, used for monitoring the mixed radiation field of the LHC accelerators. The CERN guidelines were adopted to qualify the RadMon components under radiation in order to develop a new architecture both more tolerant to radiation and more versatile than that of the previous version. In this context, the challenges that radiation tests impose for measuring Single Event Effects (SEUs) on a complex mixed-signal component such as the Analog to Digital converter, led to the development of an innovative test technique, which will be described in this thesis.

The reliability of the RadMon measurements strongly depends on the calibration of its sensors. The complex radiation environment of the LHC imposes a peculiar qualification process which will be described and discussed in this work for the RadFets (Total Ionizing Dose sensor) and the SRAM memories (High Energy Hadrons fluence sensor).

The use of the RadFet in a mixed field radiation environment has been studied and analyzed by means of ^{60}Co sources as well as proton beams at different energies. The RadFets have been re-calibrated by studying the dose rate, particle sources, temperature, annealing and fading effects as a function of the oxide thickness. Furthermore, thanks to the new architecture of the RadMon, new biasing configurations have been tested to improve the resolution. Two types of SRAM memories with technology nodes of 400nm and 90nm have been tested and calibrated by following a strict qualification methodology which includes tests with protons in the range 30–400 MeV, and with neutrons from thermal energies up to intermediate energies ($\sim$14 MeV). The 90nm memory improves the accuracy and resolution of the hadrons fluence measurements.

Moreover, the simultaneous use of both types of memories permits an improvement on the accuracy of the thermal neutron detection with respect to the previous version, as a result of a procedure which will be detailed in this work.

The efforts towards the improvement of the TID measurements resolution for the new RadMon lead to the research and study of a new type of dosimeter sensor: the Floating Gate dosimeter (FGDOS). The sensor embeds complex circuitry, thus a full radiation qualification was necessary. Mixed field radiation tests, ^{60}Co and protons tests have been carried out in order to evaluate the performance and the possible issues of the sensor. In this context, an analytical model of the sensor was developed to prove that the floating gate structure can be used as charge yield measurement instrument at room temperature and at low electric fields.

The radiation tolerance characterization of the hardware, the qualification and calibration process of the sensors have significantly improved the overall reliability and quality of the measurements of the new RadMon. These improvements turned it into a reference instrument for radiation monitoring of complex mixed fields, such as the one encountered in the LHC, its injectors chain, and other particle physics research centers, such as JLAB in US, J-PARC in Japan.

Résumé

La mesure des niveaux de rayonnement est une exigence essentielle dans le LHC et ses lignes d'injection afin de quantifier les effets des radiations sur l'électronique et de fournir une connaissance détaillée du champ de rayonnement. Le système de surveillance des rayonnements pour l'électronique au CERN, le " RadMon ", a été installé dans les zones critiques où l'équipement est ou sera placé. Les problèmes rencontrés au cours des dernières années d'utilisation du Radmon, l'obsolescence de quelques éléments fondamentaux de la carte électronique et la nécessité d'améliorer la précision et la résolution des mesures a conduit au lancement d'une nouvelle conception du moniteur.

Ce travail décrit l'architecture du nouveau RadMon (V6), sa fiabilité dans les environnements radiatifs et de la stratégie adoptée pour choisir et qualifier les capteurs utilisés pour surveiller le champ de rayonnement mixte des accélérateurs du LHC. Les directives du CERN ont été adoptées pour qualifier les composants RadMon sous rayonnement afin de développer une nouvelle architecture à la fois plus tolérante au rayonnement et plus polyvalente que celui de la version précédente. Dans ce contexte, les défis que les tests de rayonnement imposent pour mesurer les Single Event Upsets (SEUs) sur un composant complexe à signaux mixtes tels que le convertisseur analogique-numérique, ont conduit au développement d'une technique de test innovant, qui sera décrit dans cette thèse.

La fiabilité des mesures effectuées par le RadMon dépend fortement de l'étalonnage des capteurs. L'environnement radiatif complexe du LHC impose un processus de qualification particulier qui sera décrit et discuté dans ce travail pour les RadFets (capteur dose ionisante) et les mémoires SRAM (capteur de fluence High Energy Hadrons).

L'utilisation du RadFet dans un champ mixte de rayonnement a été étudié et analysé au moyen de sources de ^{60}Co et de faisceaux de protons de différentes énergies. Les RadFets ont été ré–étalonné en étudiant le débit de dose, les sources de particules, la température, la guérison thermique en fonction de l'épaisseur d'oxyde. En outre, grâce à la nouvelle architecture de la RadMon, de nouvelles configurations de polarisation ont été testées pour améliorer la résolution.

Deux types de mémoires SRAM avec des nœuds technologiques de 400 et 90 nm ont été testés et calibrés en suivant une méthode de qualification stricte qui comprend des tests protons, dans la plage de 30 à 400 MeV et neutrons, depuis les énergies thermiques jusqu'à des énergies intermédiaires ($\sim$14 MeV). La mémoire 90 nm améliore la précision et la résolution de la mesure de la fluence hadronique. En outre, l'utilisation simultanée des deux types de mémoires améliore la précision de la détection des neutrons thermiques par rapport à la version précédente, grâce à une procédure qui sera détaillée dans ce travail.

Les efforts en vue de l'amélioration de la résolution des mesures de TID pour le nouveau RadMon conduisent à la recherche et à l'étude d'un nouveau type de dosimètre : le dosimètre a Grille Flottante (FGDOS). Le capteur intégrant une électronique complexe, une qualification complète sous rayonnement était nécessaire. Des tests en champ mixte, des tests au ^{60}Co et des tests au protons ont été réalisés afin d'évaluer les performances et les problèmes potentiels du capteur. Dans ce contexte, un modèle analytique du capteur a été conçu pour démontrer que la structure à Grille Flottante pouvait être utilisée comme instrument de mesure du "charge yield" à température ambiante et sous des champs électriques faibles.

La caractérisation de la tolérance au rayonnement du matériel, le processus de qualification et les étalonnages des capteurs ont considérablement amélioré la fiabilité globale et la qualité des mesures sur la nouvelle version du RadMon. Ces améliorations font du RadMon un instrument de référence pour la surveillance des rayonnements des champs mixtes complexes, tels que ceux rencontrés dans le LHC et sa chaîne d'injecteurs, mais aussi pour d'autres centres de recherche en physique des particules, comme JLAB aux États-Unis, J-PARC au Japon.

Contents

Chapter 1

Introduction

At the Conseil Européen pour la Recherche Nucléaire or European Council for Nuclear Research (CERN) the fundamental structure of the universe is being studied by researchers and physicists of all around the world. To perform this task a particle accelerators of unprecedented energy and intensity are required. For this reason at CERN, an accelerator complex uses a succession of accelarator machines that accelerate particles to increasingly higher energies. Each machine boosts the energy of a beam of particles, before injecting the beam into the next machine in the sequence. This machine sequence is also referred as the "injector chain". The last accelerator is the Large Hadron Collider, the largest accelerator in the world where particle beams are accelerated up to the energy of 4 TeV per beam and in the future to 7 TeV (the nominal LHC energy). Inside the four detectors – called ALICE, ATLAS, CMS and LHCb placed around the LHC ring the beams interact giving the physicist the possibility to study the elementary particles of the universe.

While accelerating beam losses can occur throughout this chain of accelerators at several locations and through three general categories:

1. beam collision in the "cleaning point" where part of the beam intercepts a collimator (or collimator–like objects) in order to avoid distributed losses in other parts of the accelerator;

2. beam collision at the experimental areas;

3. beam interaction with residual gas inside the pipe.

Beam interactions thus result in a complex radiation field composed of different particle types and energies. High radiation levels encountered at CERN in various LHC underground areas, as well as its injector chain, in particular the integrated flux (hereafter referred to as fluence) of high-energy hadrons (particles with an energy

beyond the MeV) pose a significant risk to all electronics if they are not specifically designed or tested for such radiation levels.

The negative impact of radiation on electronic devices in the LHC was underestimated until 2007. A failure in the ventilation system of the CNGS (CERN Neutrinos to Gran Sasso) facility in 2007 forced the experiment to be stopped for 5 days. Three incidents due to Single Event Upset (SEU) were recorded on the programmable logic controller (PLC) of the ventilation control electronics. The failures were induced by high-energy hadrons. The successive counter-measurements were to move most of the electronics out of CNGS tunnel area, create a radiation safe area and add shielding.

This incident underlined the potential problems due to radiation on all electronic systems installed in all the LHC underground areas. The Radiation to Electronics project (R2E) started with the main objectives of limiting the failures due to radiation impacting operation of the LHC and the injector chain. The main target of the project is also to assist the LHC operations and equipment groups in the field of radiation effects/damage to electronics. The different groups are supported in the assessments of the radiation–induced failures in electronics, and in the development of radiation–tolerant systems. The R2E also provides a radiation map of the accelerator complex by means of simulation and monitoring stations.

The CERN radiation environments are unique in terms of mixed particle types and energies involved, but also because of the different ranges of fluxes and dose which is possible to have in the different zones of the accelerators. In the Figure 1-1 an overview of the radiation levels which is possible to measure in the accelerators complex is reported. The high fluxes of high-energy hadrons and the high doses in zones like the injectors chain (PS, SPS , PSB) and several zones in the LHC tunnel such as the collimators [1], require a system which is capable of measuring without saturating fluxes in the order of 1×10^{10} particles per hour and cumulated doses up to 1 KGy per year. On the other side, as depicted in Figure 1-1, there are the so called "protected zones" where the radiation levels go as low as 1×10^{6} particles per hour and below 1 Gray per year for the cumulated dose.

A reliable radiation monitoring system is required to measure these radiation levels at the location of electronics and provide a detailed knowledge of the radiation field in the accelerator tunnel and adjacent areas. This information is important not only for the design and installation of equipment, but also to decide on possible relocation or shielding requirements of electronics sensitive to radiation. The existing monitoring systems for accelerators are optimized to allow for proper beam steering and the detection of beam losses, with limited performance for the measurement of the radiation fields and respective quantities important for radiation damage issues.

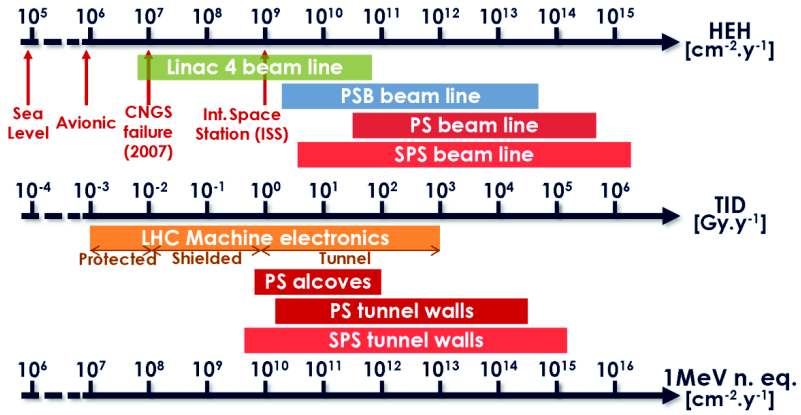

Figure 1-1: Radiation levels per year along the CERN accelerator complex expressed in term of TID, HEH and 1-MeV neutron equivalent fluences [1].

For this reason, the RadMon system has been developed by the CERN ENgineering (EN) department [2].

The RadMon system allows continuous monitoring of the three quantities important for radiation damage to electronics (high-energy hadron fluence, total ionizing dose and 1 MeV-neutron fluence equivalent), thus anticipating instantaneous radiation failures as well as long-term degradation of the electronics equipment exposed to the CERN radiation fields. This monitoring system has also been used in the CERN past and future experimental test areas (H4IRRAD, CNRAD, and CHARM) where accelerator-like radiation fields can be reproduced and the radiation tolerance of equipment and systems that will be used around CERN accelerators is tested.

This work is focused on the development of the new version of the RadMon (V6) and the improvement of its dosimetry and acquisition chain [3]. The older version of the RadMon (V5) imposes some constraints and issues that have been discovered only in operation. One of the main issues was the limited radiation tolerance of the embedded electronics. This and other problems have been faced and solved with the development of the new version of RadMon based on a new hardware development, compliant with the CERN policy on the radiation qualification process.

In addition to the the new hardware development, the main objective was to improve the dosimetry part. Indeed, the wide ranges of the quantities to be measured in the CERN complex require a proper selection of the sensors to be used and a strict calibration process. This thesis shows how the overall accuracy of the measurements has been improved by carrying new calibration campaigns for each sensor.

In this sense, the RadFets and the SRAM memories used on the RadMon have been calibrated in different radiation fields which are representative of the LHC radiation

environment. As already mentioned, the radiation levels in some protected zones are very low and for this reason there is a continuous effort to reach higher sensitivity. This research lead to scope other sensors configuration, as the case of the RadFet, and also other type of sensor as the new Cypress memory, both embedded on the new version of RadMon. The effort put in the research of a better sensor drove the investigation of a new kind of dosimeter, the floating gate. This sensor has been analyzed deeply in this work and its suitability for the implementation on the future version of the RadMon has been investigated.

Chapter 2 of this work gives an overview on the radiation effects on the electronics and the sensors which are used to measure the quantities related to them. The second part of the chapter is dedicated to the policy and strategy adopted at CERN in order to qualify the electronics equipment installed in the radioactive zones, such as the RadMon. The qualification and calibration process, which the RadMon and its sensors are subject to, foresee the use of several irradiation facilities both inside and outside CERN. These facilities are described in the last part of the second chapter.

The hardware development of the RadMon V6 is described in Chapter 3, highlighting the new features and improvements with respect to the previous version. The qualification strategy imposes the radiation tests of all the hardware components, thus in the last part of the chapter, the radiation tests results of some important components such as the FPGA, the ADC and the voltage regulators are reported and analyzed.

Chapter 4 is dedicated to the RadFets; the working principles are described in the first part along with the technique used to read them. The calibrations for different configurations and the study on the annealing after irradiation are reported. A study on the temperature coefficient as function of the cumulated dose is also performed in order to correct for it during operation. The last part of the chapter is dedicated to the study on the effect of the mixed radiation field on the RadFet response.

The results on the SRAM memories used in the RadMon V6 as hadron fluence counters are reported in Chapter 5. The SRAM memories from Toshiba and Cypress have been tested in several radiation facilities. The improvement on the accuracy given by the use of both memories at the same time on the RadMon V6 has been analyzed and discussed in a dedicated paragraph of this chapter.

The last chapter (Chapter 6) is dedicated to the floating gate sensor which has a different working principle from the RadFet, thus, a deep analysis of the physics behind it is given. The sensor is embedded in a complex readout system and all its functionalities are described in this chapter. The test results obtained with a ^{60}Co and proton beam irradiation are reported and discussed. An analytical model is

presented to understand the key parameters of the sensor. Furthermore, it has been demonstrated that the floating gate structure is also a good instrument to measure the charge yield at very low electric field.

Chapter 2

Radiation Effects on Electronics, Test Strategy and Test facilties

2.1 Radiation Effects on electronic components

The three categories of radiation effects are Total Ionizing Dose (TID), Displacement Damage (DD), and Single Event Effects (SEE). The SEE and TID effect are associated with direct or indirect ionizing energy, while the displacement damage is associated with the Non Ionizing Energy Loss (NIEL) that is a quantity that describes the rate of energy loss due to atomic displacements as a particle traverses a material. The importance of understanding the radiation effects in the LHC environment on the electronic components is not limited to the quality assurance and test strategy, described later in this chapter, but is also necessary to understand how the radiation levels are measured. Indeed, for each quantity to be measured is associated a sensor. The presence of all three radiation effects points out the necessity of characterizing the equipment to be installed in the tunnel, thus a strategy for radiation testing is necessary. Naturally, the testing strategy has to be applied to the RadMon system and to each one of its components. The radiation testing and sensor characterization usually are carried out in external facilities which are presented in the last part of this chapter.

2.1.1 Basic TID effects on MOS

The standard definition for the TID effect is a "circuit degradation or failure resulting from radiation-induced charge trapping in insulating layers (usually oxides)" [4]. The insulating oxide layer has a strong influence on the Metal Oxide Semiconductor (MOS) working function. The most important mechanisms in the degradation of

the MOS performances are caused by ionizing radiation in the dioxide layers and by the photocurrent generation in the source and drain junction of a MOS transistor. The effects due to the ionizing radiation in the SiO_2 layer will be deeply analyzed in Chapter 4; in this paragraph a short review is given in order to present a complete overview of all the radiation effects.

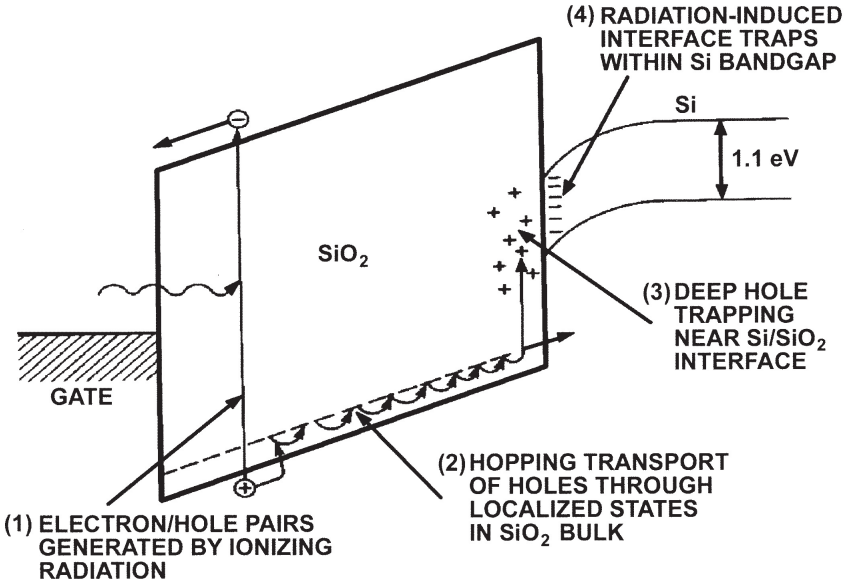

Figure 2-1: Energy band diagram for a biased MOS structure with the physical processes involved in the radiation response. [5].

The Figure 2-1 is a schematic representation of the energy band diagram for a MOS structure with a positive bias applied at the gate [5]. The processes involved in the radiation response of a MOS are labeled (1)–(4). Processes (1)–(3) deal with the generation, transport and trapping of holes within the SiO_2 film, and (4) has to do with the radiation-induced buildup of interface traps at the SiO_2–Si interface. The first two processes constitute what is referred to as the short-term response, and they will be analyzed in Chapter 4. Processes (3) and (4) are the two components involved in the long-term radiation response of MOS systems. The main actors of the processes (3) and (4) are the holes that reaching the SiO_2 interface can be captured in a long–term trapping sites. The fourth and final component of the MOS response is the buildup of interface traps at the Si/SiO_2 interface.

Long–term radiation effects are manifested through parametric shifts in MOS devices and can last from hours to years. Indeed, a major electrical consequence of the radiation induced charging of the SiO_2 layers is a shift of the threshold voltage.

The threshold voltage after the irradiation can be written as:

$$V_{th}(t) = V_{th}(0) + \Delta V_{th}(t) \tag{2.1}$$

where $V_{th}(0)$ is the threshold voltage before the irradiation and $\Delta V_{th}(t)$ is the shift after the irradiation. The pre–irradiation voltage threshold depends on the work function potential of the MOS, oxide thickness and temperature [6]. The initial threshold depends also on the oxide charges and interface traps already existing before the irradiation, but usually for actual devices their density is fairly low.

The most important effect of the variation of the MOS threshold voltage is the change in its current–voltage characteristic. The TID effect on the drain current as a function of the gate potential for an n–MOS type transistor is depicted in Figure 2-2. As the cumulated TID increases, the I–V curves are shifted to a more negative voltage and their slope decreases. In addition to the threshold voltage shift, the subthreshold curves and the midgap potential also change [7]. In particular, the leakage current when the transistor is in the OFF condition can increase. This, in turn, can have a drastic impact on the characteristic and lifetime of the integrated circuit of which the MOS is part of. The change in the slope of the I–V curve characteristic is due to the degradation of the carrier mobility in the channel of the transistor. It has been shown that the mobility degradation correlates with the radiation–induced interface traps [8]. The TID is a cumulative effect of particular importance in the zone in which the radiation levels are quite high and where component life time is of particular importance.

In accordance with the International System of Units (SI), the Gray (Gy) is the unit for the ionizing radiation dose. It is defined as the absorption of one joule of radiation energy by one kilogram of matter. The equivalent cgs unit, the rad (equivalent to 0.01 Gy), remains common in the space community. In this work both the notations have been used. The measured TID is always referred to the dose in Silicon material (Si). In the RadMon, the TID is measured by the RadFets which will be described in the Chapter 4, along with a deeper analysis of the physics behind this effect.

2.1.2 Single Events Effects

The single event effect is initiated by a single particle, which interacting with the surrounding material can produce many different effects in an electronic circuit. Destructive and non–destructive events due to single particle strike are reported in Table 2.1.

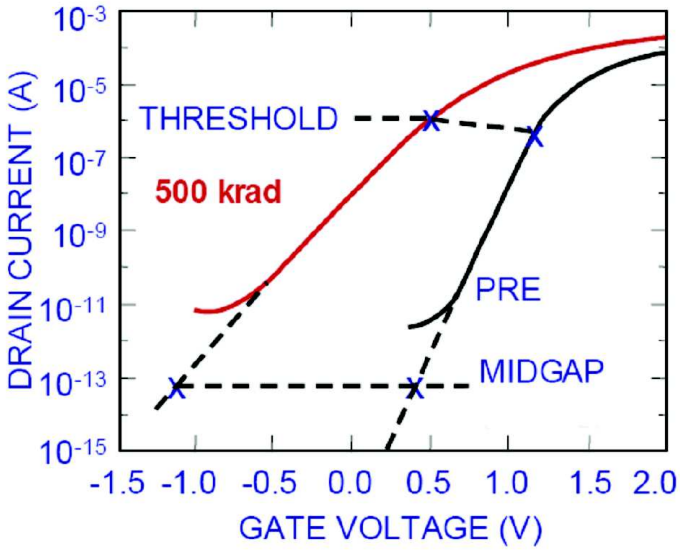

Figure 2-2: $I_d - V_{gs}$ curve for a n–type MOS. The threshold voltage and the midgap voltage shift before and after the irradiation are depicted [9].

There are two primary methods by which carriers are released: direct ionization by the incident particle and ionization by secondary particles created by nuclear reactions between the incident particle and the target material. Direct ionization can cause an SEU if the incident particle is ionizing enough to free a very high density of carriers. For lighter particles, such as the protons, direct ionization may produce an insufficient amount of charge to cause an upset directly and an SEU may instead be due to ionization produced by secondary particles.

Looking deeper at the direct ionization process, when an energetic particle passes

Table 2.1: List of destructive and non–destructive single events effects on electronic components.

Result	Achronym	Effect name	Description
Non-Destructive	SEU	Single Event Upset	Switching of a digital logic state
Non-Destructive	SET	Single Event Transient	Voltage transient at circuit node
Non-Destructive	SEFI	Single Event Functional Interrupt	Functional failure of control logic
Destructive	SEB	Single Event Burnout	High Current condition in bipolar and Power MOSFET
Destructive	SEGR	Single Event Gate Rupture	Destruction of Insulated Gate in power MOSFET
Destructive	SEL	Single Event Latchup	High current in parasitic thyristor

through a semiconductor material it releases charged carriers along its path as it loses energy. When all of its energy is lost, the particle comes to rest in the semiconductor, having traveled a total path length referred to as "range". The terms linear energy transfer (LET) or dE/dx describes the energy loss per unit path length of a particle as it passes through a material. LET has units of MeV-cm^2/mg. We can easily relate the LET of a particle to its charge deposition per unit path length, because for a given material it takes a certain amount of energy to release an electron-hole pair. Direct ionization is the primary charge deposition mechanism for upsets caused by heavy ions, where we rather loosely define a heavy ion as any ion with atomic number Z $\geq$ 2. Direct ionization by light particles usually does not produce a high enough charge density to cause upsets, although for latest technology nodes the direct ionization due to lighter particles can be possible [10].

Protons and neutrons can produce upsets due to indirect mechanisms. A high–energy proton or neutron entering the semiconductor lattice may undergo an inelastic collision with a nucleus. This may result in the emission of alpha or gamma particles and the recoil of a daughter nucleus or a spallation reaction, in which the nucleus is broken into two fragments. Any of these reaction products can now deposit energy along their paths by direct ionization causing an SEU. Once the electron–hole pairs are created, there are three mechanisms that take place:

1. carriers can move by drift in response to applied or built-in fields in the device.

2. carriers can move by diffusion under the influence of carrier concentration gradients within the device

3. carriers can be annihilated by recombination through direct or non-direct processes

When a particle strikes a microelectronic device, the most sensitive regions are reverse biased p/n junctions, as illustrated in Figure 2-3. The high field present in a reverse–biased junction depletion region can very efficiently collect the particle-induced charge through drift processes, leading to a transient current at the junction contact. An important discovery was that charge generated along the particle track can locally collapse the junction electric field due to the highly conductive nature of the charge track and separation of charge by the depletion region field. This funneling effect can increase charge collection at the struck node by extending the junction electric field away from the junction and deep into the substrate, such that charge deposited some distance from the junction can be collected through the efficient drift process.

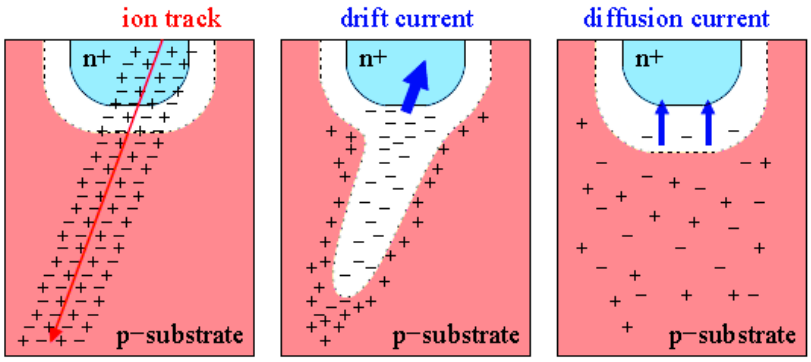

Figure 2-3: Reverse biased p/n junction hit by a ion strike. The strike is followed by a drift and diffusion current.

In terms of single event what really matters is determining whether the event actually causes an error in circuit operation. The most known example of the upset is the one taking place in the SRAM cells. An SRAM is made by two cross–coupled inverters; the coupling produces a stable loop and thus a stable output. When an energetic particle strikes a sensitive location in a SRAM, usually the charge collected at the reverse biased drain junction of the MOS in the OFF state (see Figure 2-4), charge collected by the junction results in a transient current in the transistor hit. As this current flows through the struck transistor, the restoring transistor ("ON" p-channel transistor in Figure 2-4) sources current in an attempt to balance the particle-induced current. Unfortunately, the restoring transistor has a finite amount of current drive, and equally importantly, a finite channel conductance. Current flow therefore induces a voltage drop at the drain of the restoring transistor. This voltage transient in response to the single–event current transient is actually the mechanism that can cause upset in SRAM cells. Single-event multiple-bit upsets (MBUs) occur when a single particle causes more than one error. For example, diffusion of charge to junctions placed very close can upset more than one bit in both SRAM. When testing for SEUs a common way is to define the device cross section. The cross section is defined as the number of SEU divided by the number of particles (or fluence) which the device is exposed to, expressed in particles/cm^2 or simply as p/cm^2. The cross section for a memory usually is expressed per bit, thus dividing for the size of the memory. The cross section for a memory will have the unit of cm^2/bit. The heavy ions test of an IC is a mandatory test for space qualification [11] and the cross section is usually reported as a function of the LET. In an acccelerator–like environment, it makes sense to test the device with protons, because of the absence of heavy ions in the radiation environment. The cross section, is reported as a function of

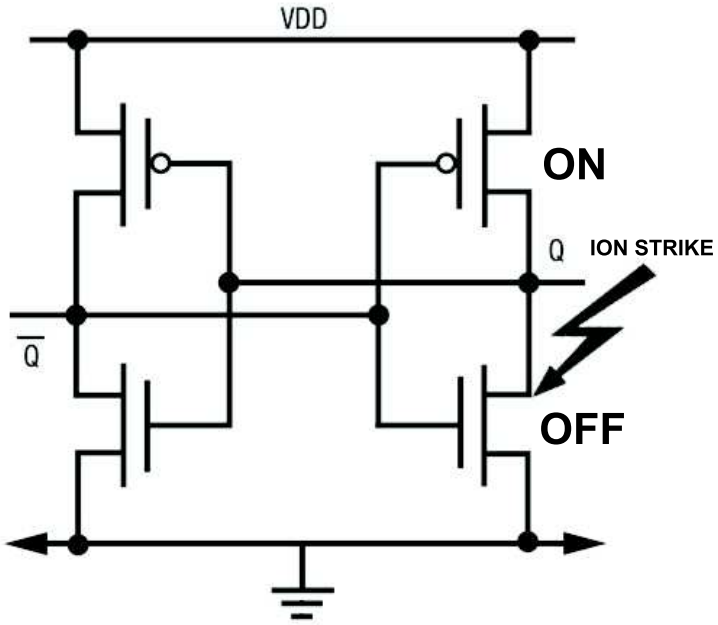

Figure 2-4: SRAM cell hit by a ion strike on its off node.

the incoming proton energy. The number of SEUs or the SEU rate represents the number of bits flipped, for example, in a memory device. If the memory has been previously characterized and its cross section is known, then the memory can become an instrument (or we can define it as a "sensor") that is capable of measuring the fluence of particles passing through it. The number of SEU can be converted to the number of particles passing through the memory using the cross section of the device. In order to have a good sensor, it is necessary to have a cross section which is as high as possible; a good memory can be qualified as a fluence sensor if its cross section is around $10^{-13} - 10^{-14}$ cm^2/bit. The entire Chapter 5 is dedicated to the requirements, characterization and measurements of the RadMon SRAM memories.

We focused on the "soft" errors due to single–particle strikes, but great attention should be also be paid to destructive events, above all in the electronic devices testing strategy. "Hard" events such as a Single Event Latchup, very common in memory devices, should be well characterized and the possible energy dependency of their cross section assessed, as we will see in the paragraph 2.2.

2.1.3 Basic Displacement Damage effect

Bulk damage mechanisms result mostly from atomic displacement mechanisms, so called displacement damage (DD). Particles impinging on a crystalline material lose

a part of their energy by displacing an atom out of its lattice position leading in a silicon interstitial and left over vacancy. A vacancy is the absence of an atom from its normal lattice position. If that displaced atom moves into a nonlattice position, the resulting defect is called an interstitial. The combination of a vacancy and an adjacent interstitial is known as a close pair or a Frenkel pair. The incident particle and the recoil nucleus can migrate through the material and may finally provide the building block for extended defects [12]. The change observed in semiconductor conductivity is associated with the formation of defect clusters. Damage can induce performance degradations in many electronic devices, such as silicon bipolar transistor, solar cells, and silicon detector [13, 14].

The displacement damage is proportional to the total number of particles hitting the devices per unit surface. Non Ionizing Energy Loss (NIEL) "rule" [12] links the radiation damage produced by different particle types and energies with respect to the change measured in the material (commonly Silicon for the electronics). By knowing the displacement damage cross section, it is possible to define a hardness factor allowing to compare the damage efficiency of different radiation sources with different particle energies [12]. The hardness factor is used in such a way that the damage produced by a specific source or environment can be reported as the the damage which would have been produced by monoenergetic neutrons of 1 MeV. The displacement damage is measured by the RadMon by means of commercial PIN diodes biased in forward mode. The topic has been deeply analyzed in the [15, 16] and it will be not subject of this thesis work.

2.2 Strategy for quality assurance of the electronics components in the LHC accelerator environment

As already discussed in the previous paragraphs, electronic components exposed to a radiation field such as the one in the LHC, will experience all three different types of radiation damages. Care should be taken in considering not only the particle type, but also the respective energy distribution when testing for the radiation tolerance and for the sensor characterization. A qualification strategy is necessary for a successful project in the LHC environment [17]. Being a system that has to be installed in radioactive areas, the RadMon system and its sensors should pass all the tests foreseen for the quality assurance of the LHC equipment. The test of the components and/or the system is part of a process that starts with the definition of the system requirements. Once the designers specify the type of systems to be used and

its components, the radiation effects to be considered are analyzed by knowing the environment, which depends on the installation area. The test strategy is planned keeping in mind the system complexity and the environment.

The LHC equipment and its subsystems can be classified into two main categories:

- Fully commercial system, here referred to as COTS system
- Custom electronic systems based on COTS components.

COTS systems are fully commercial devices. Programmable logic controllers (PLC), Uninterruptable Power Supplies (UPS), commercial Voltmeter, temperature monitors and fire detectors, fit in this category. The traceability of this equipment is difficult. These products are purchased from external companies and there is no control of the single components used in the design, which moreover can change from one purchase order to another.

Custom systems are electronic boards which are developed by CERN engineers based on COTS components. The developers knows all the components used in the projects and is not like a "black box" as in the case of the COTS systems. Whenever it is possible, the designers use the components, which have already been tested or qualified. If the components have to be qualified, then a qualification process, as it will be discussed, has to be planned. The radiation hardened components usually developed for the military and space industry are evidently advisable for custom solutions, but their high cost prevents the use in projects were hundreds or thousands components have to be used. The RadMon system belongs to this category since it is completely built on COTS.

In order to define the radiation tolerance required it is necessary to know the radiation levels which the equipment is exposed to. This depends substantially from the location in which the system is planned to be installed. We defined two main categories, the tunnel areas and the shielded areas.

1. Accelerator tunnel areas
    - LHC areas close to experiments or areas with high losses, for example collimators areas: very high radiation levels generally excluding the installation of electronic systems
    - LHC Dispression suppressor (DS): tunnel area with higher radiation doses
    - LHC ARC: tunnel area with lower doses
    - Injectors: usually higher radiation doses, partly excluding the installation of electronic devices

- Shielded areas
- Critical zones (areas with annual fluences above 10^6 n/cm^2)
- Safe zones

All the locations in which the beam intercepts and interacts with the machine belong to the first category of the tunnel areas. Some of these zones have a very harsh radiation environment and in this zone no electronics is usually installed. Conversely the shielded areas are the zones with a low radiation field where usually the electronic systems are installed. Based on these assumptions it can be concluded that commercial systems are installed in shielded and relatively low radiation areas, providing some mitigation measures to reduce the impact on accelerator operation. These kinds of equipments should be tested in order to estimate the overall failure rate. The COTS based systems can be installed in tunnel areas but require a respective radiation tolerant design and dedicated radiation test planning. For all the installations after obtaining the complete list of the locations, the radiation levels are simulated by means of FLUKA. In any case certain safety margins have to be taken into account:

1. the uncertainty of the radiation levels (if only simulations are available: a factor of 2 has to be taken in consideration)
2. the low dose rate effects (a factor of 3 has to be considered only for bipolar devices)
3. the traceability of the components (a factor of 3, absence of lot codes or respective characterization).

In order to obtain an estimate for the expected failure rate, it is needeed also to specify the number of exposed systems or components. This collected information can then either be used to estimate the failure rate and life–time based on radiation test results, or to determine the target levels required for radiation tests as happens for to the RadMon system where the TID level and the maximum fluence before the death are set as target.

In the shielded and low–radiation areas where the radiation levels do not overcome the 10^9 HEH/cm^2/year TID and DD are not a concern for the equipment, while the SEEs remain the source of problems. In the safe areas the cumulated fluence per year does not overcome the 10^6 HEH/cm^2/year thus in these zones there are no issues in the installation of the electronics which do not need any radiation test. In these areas the COTS system could be used but it is required to qualify the entire system for

their SEE vulnerability. The cross section measurement for the different types of soft SEEs and the knowledge of the expected radiation levels provide a good indication if the system failure rate is acceptable in terms of mean time between failures (MBTF). If the cross section found is not acceptable, mitigation techniques at the system level, such as the implementation of automatic resets, software fault diagnostics and use of redundant subsystems, have to be put in place.

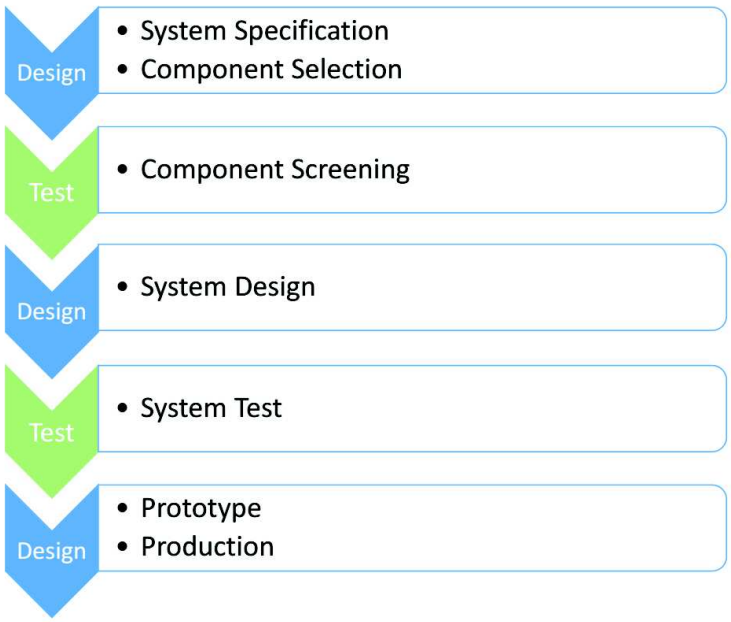

Figure 2-5: Strategy for the qualification process of the tunnel COTS custom boards (i.e. the RadMon).

For tunnel and high radiation areas (where the flux is higher than 10^9 HEH/cm^2 per year), all the radiation effects on electronic components have to be considered. In these areas, the installation of the equipment is allowed only when electrical and functional constraints make it necessary or if the purposes of the equipment is of the radiation monitoring, as the case of the RadMon. The use of fully commercial systems is not allowed. All custom developed systems must be radiation tolerant and the traceability and the qualification of the lots of the critical components used in the design are required, or the respective safety margins are to be taken. The qualification process is depicted in Figure 2-5.

Taking as an example the RadMon system, the test process foresees a component screening test, the lot qualification after the purchase and then an additional verification of the entire board/system with the chosen components. The component

selection is a phase of the system design and depends on the project specifications. The research of the most suitable components is carried out on the databases of the radiation tolerant devices available at CERN itself via the knowledge sharing of the Radiation Working Group (RADWG) [18], or outside CERN on the NASA database [19] or any other vendors who make the radiation data available [20]. Finally, a prototype board is produced, populated with the qualified components, and tested. If the final prototype passes the qualification test, it will be possible to start the production.

As mentioned before after having understood the location and the possible effects that can concern the electronics components, the radiation tests need to be performed. The best solution will be to test in a facility which allows the test of all three types of radiation effects. Two types of facilities are available; the first is a proton beam facility and the second is a CERN mixed field facility. Both the facilities will be analyzed in the successive subsections. If only TID is a concern for the device under test, then a ^{60}Co source can be used. The DD test is used as a screening test only if the device under test has to work up to relatively high fluences (higher than 10^{13} n/cm^2) or is known to be very sensitive to non-ionizing damage (i.e. bipolar and optical components).

While this testing process is efficient for the components of a custom development, things get more complicated when the RadMon sensors have to be characterized. Several other issues have to be faced. Indeed, for each sensor described in the next chapters, the motivation of each radiation test will be described. All the facilities used in this work for the qualification of the RadMon components and for the sensors characterization will be described in the next paragraphs.

2.3 Test Facilities

The process of components and systems qualification imposes to carry radiation tests in order to measure their susceptibility to SEE, TID and DD effects. As previously said the proton test is a complete test which permits to test the three effects at the same time. The main proton facilities used by the CERN groups are the Paul Scherrer Institute "PIF" facility in Villigen (Switzerland), and the TRI-University Meson Facility (TRIUMF) in Vancouver (Canada).

The calibration of a dosimeter sensor is usually carried out in Co^{60} gamma field; for two main reasons: a) the precise calibration provided by the facility (usually the dose is given with an uncertainty of around 1-2%), b) DD and SEE will not affect the "Device Under Test" DUT avoiding synergies among the three effects. The ^{60}Co

gamma irradiation facilities used in this work are at Fraunhofer INT (Germany) and at the University of Santiago de Campostela (Spain).

The SRAM memories used as HEH and thermal fluence sensor have been tested for SEUs in several facilities. The neutron facilities are the LVR–15 in Czech Republic and the Physikalisch-Technische Bundesanstalt (PTB) PIAF facility (Germany). Finally, the test carried out in a mixed radiation field are done at CERN facilities, called H4IRRAD and CNRAD.

2.3.1 Paul Scherrer Institute PIF Facility

The main proton irradiation facility used by CERN is located at the Paul Scherrer Institute (PSI) in Villingen (Switzerland). The facility has been built in cooperation between the Paul Scherrer Institute and the European Space Agency (ESA) [21]. The irradiation area of the PIF facility is located in the experimental area of the superconducting cyclotron-type accelerator COMET dedicated to tumor therapy [22]. The initial proton beam is 230 MeV which is delivered from the COMET accelerator, an energy degrader consisting of 7 Cu-plates of various thicknesses between 0.5 mm and 32 mm allows for a quasi continuous setting of the energy on the target down to approximately 10 MeV. The maximum beam intensities allowed by the radiation safety officers for the PIF site is 5 nA. The minimum beam intensity is around 0.1 nA, below this value the beam starts to be unstable. The intensity and the energy can be remotely set from the operating console in the PIF barrack. The week day shifts are reserved for biomedical applications, thus the facility is used during the weekends. The beam size and shape can be modified by means of copper collimators. The collimator used in this work have a diameter of 5 cm, 2 cm and 1 cm. The dosimetry of the facility is given by means of two flat, air filled ionization chambers. The beam profiles and uniformity is measured with a plastic scintillator detector. The profile measurement is done without the collimator. An example of profile shape is depicted in Figure 2-6 The detector is centered in the same position of the DUT.

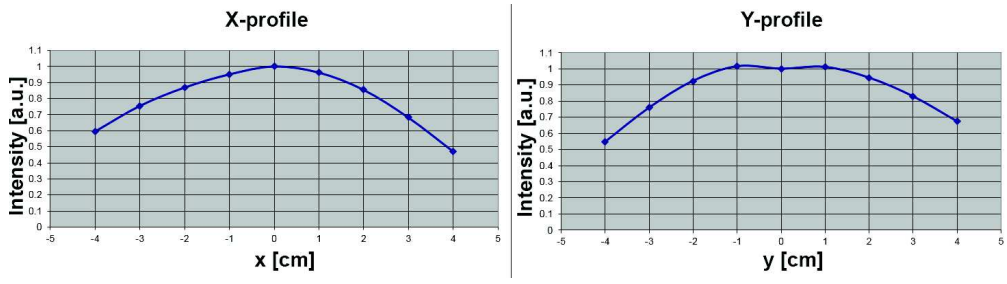

Figure 2-6: Beam profile at PSI without the collimator

A calibration phase is performed before starting the DUT irradiation for all energies and for all the collimators used in the tests. The verification of the proton flux is carried out with the ESA SEU monitor [23]. The experimental bench consists of a standard frame for user devices fixed on a XY-table. Two lasers for device positioning are aligned with the beam line. They illuminate the user setup from the back.

2.3.2 TRIUMF – PIF Facility

In 1995, TRIUMF has built up several beam lines that provide energetic proton and neutron beams to test electronic components emulating a radiation exposures either in space or terrestrial environments. One of the beam lines is used for the cancer treatment of ocular melanoma at the Proton Therapy Centre which is operated in conjunction with the BC Cancer Agency and the UBC Department of Ophthalmology (see Figure 2-7). Two beam lines are dedicated to proton test, BL2C and BL1B [25]. They mainly differ for the extraction energies. The BL2C is capable of providing initial proton energies from 65 to 120 MeV, lower energies (up to few MeV) can be reached with a degrader. In the BL1B beam line the initial proton energy can be set at 480, 355 and 210 MeV. Energies up to 120 MeV can be reached by degradation. The beam line used in this work is the BL1B.

A thin multi–wire ionization chamber gives a real time indication of the beam position and size in the two transverse dimensions. The chamber is used to center the beam and to monitor the profile. The chamber measures with a resolution of 3 mm by means of 16 wires. The facility has two irradiation stations, one called "Front location" which stands upstream and the "Back location" which stands downstream. The maximum current allowed is 3 nA, the maximum flux in the front location is 7×10^8 pp/cm^2/s, while for the back location is 4×10^7 pp/cm^2/s. The back location has a larger beam size (3 to 7 cm) with respect to the front location (2 cm). Each test configuration requires a beam calibration at the beginning of the run, a portable ionization chamber is used to calibrate each location; a ionization chamber placed at the end of the beam pipe is kept running for the entire irradiation. The facility provides an MC counter proportional to the fluence and a secondary–emission monitors (SEM) counter proportional to the flux.

2.3.3 LVR–15 Thermal neutron facility

The LVR–15 is a research reactor, situated at the site of the Research Center Řež near Prague. The LVR–15 is a light water tank–type research reactor placed in a stainless steel vessel under a shielding cover. It has forced cooling, IRT-4M fuel and

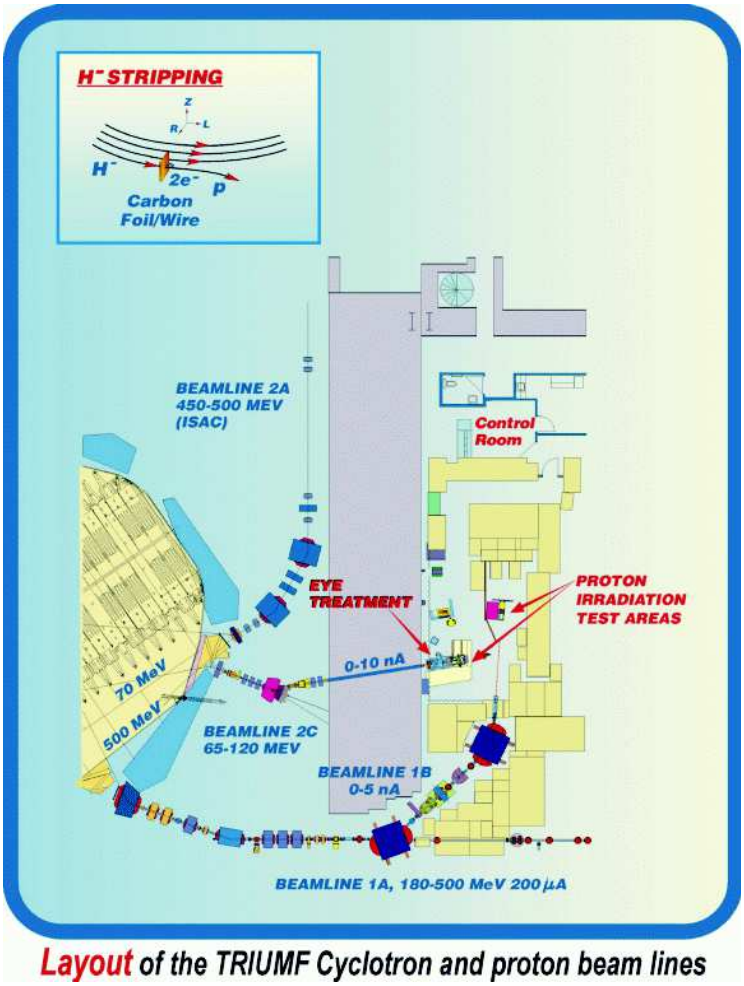

Figure 2-7: Beam Line at TRIUMF PIF facility in Canada [24]

an operational power level of 10 MW. De–mineralized water is used as moderator and absorber, a reflector is composed of a water, or beryllium block, depending on the operation configuration. The reactor has ten horizontal channels. The horizontal neutron channel HC1 is the one dedicated to the production of thermal neutrons. The channel leads neutrons from the reactor core with 3 m long and 100 mm in diameter tube. In 2012, a special filter was mounted in HC1 and a radiation shielding box was established around the channel in order to take preparations for a future neutron transmission radiography and tomography facility. The filter suppresses the fast neutrons and gamma radiation coming from the reactor and transmits thermal neutrons. For this purpose a silicon filter of a length of 100 cm was installed [26]. The test location is situated at the end of the beam outlet surrounded by a shielding of borated polyethylene 2-8. The neutron beam size is 4 cm [27]. The neutron spectra

measured by means of activation foils at the test location is reported in Table 2.2.

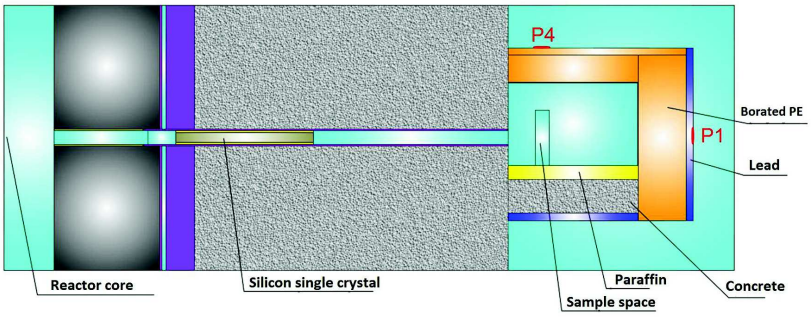

Figure 2-8: LVR–15 Nuclear Reactor and its horizontal channels [26].

Table 2.2: HC1 Neutron Spectra

Energy	Neutron flux (n/cm^2/s)
<0.501 eV	1.73×10^8
0.501 eV – 10 keV	1.28×10^6
10 keV – 0.1 MeV	6.70×10^6
0.1 MeV – 0.5 MeV	3.15×10^7
0.5 MeV – 1 MeV	5.00×10^3
1 MeV – 20 MeV	3.17×10^5

2.3.4 PTB — PIAF facility

The PTB is the German National Metrology Institute. They run two particle accelerators for the production of charged particles, an ion–microbeam as well as neutron and high-energy photon reference fields. Their mission is the production of mono-energetic neutron reference fields according to the standard ISO 8529 for the characterisation and calibration of detectors and dosimeters.

The monoenergetic or quasi-monoenergetic reference fields are produced by accelerating light ions such as deuterium or protons with a Van-de-Graaf (VdG) accelerators or cyclotrons. The accelerated particles hit a low-Z targets such as deuterium, tritium or ^{7}Li producing monoenergetic neutrons [28]. The neutrons energy used in our tests are reported in Table 2.3 along with the neutron fluxes. The facility is built around a very large dimensions of the hall with a grid floor in order to minimize the impact of neutrons scattering off the walls (See Figure 2-9).

The measurements of the neutron peak fluence are performed by means of a proton recoil proportional counter or a recoil proton telescope depending on the energy [29].

Table 2.3: List of neutron energies used during the tests and their associated capture reactions. The energy spread is represented by the FWHM. Flux rates correspond to a distance of 1 m from the source. Ti(T) stands for tritiated titanium.

Reaction	**Energy**	**FWHM**	**Target**	**Flux**
	[MeV]	**[MeV]**		**cm2/s-1**
^{2}H(d,n)^{3}He	5	0.2	D_2–Gas	5.2×10^3
^{2}H(d,n) ^{3}He	8	0.2	D_2–Gas	1.9×10^4
^{3}H(d,n)^{4}He	14.8	0.43	Ti(T)	1.3×10^4

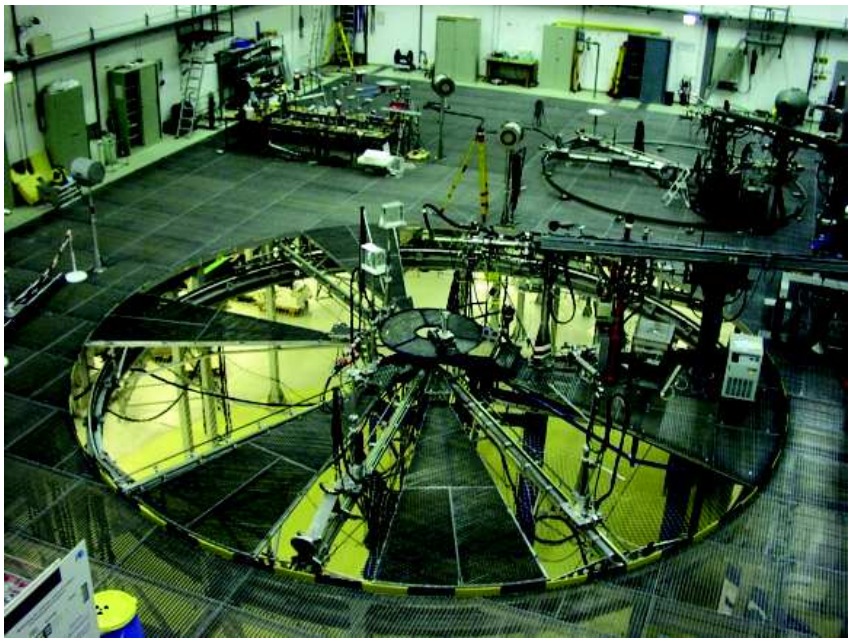

Figure 2-9: PTB low–scattering quasi–monoenergetic neutron facility neutrons test facility.

2.3.5 Fraunhofer Institute ^{60}Co facility

The Fraunhofer institute provides two irradiation facilities for ^{60}Co tests: TK100 and TK1000A. The TK100 and the TK1000A are ^{60}Co gamma irradiators manufactured by Sauerwein Isotopentechnik. Inside the shielding containers there are small radioactive pellets of a few millimeters diameter. They can be considered as point sources for distances between source and target larger than a few centimeters. The activity of the sources decreases with a half-life of 5.27 years. The radioactive ^{60}Co isotopes decay by emitting beta radiation into highly excited Ni-60 isotopes which emit two gamma photons to reach the stable ground state. The gamma radiation has two energy levels of 1.172 and 1.332 MeV but often only the mean value of 1.25

MeV is mentioned.As gamma radiation of around 1 MeV is considered as penetrating and therefore gamma particles will pass through the complete device, no measurable absorption inside the device under test (DUT) is expected. The radiation is emitted from a point-like source leading to a decreasing dose rate with increasing distance. The dose rates at two distances are proportional to the inverse square root of the corresponding distances. The dosimetry is checked with calibrated dosimeters and ionisation chambers manufactured by Wellhofer, and PTW, traceable back to national standards. The uncertainties of the reported dose rates, are typically below 3%.

2.3.6 University of Santiago de Campostela ^{60}Co Facility

The facility of the University of Santiago de Campostela (USC) is equipped with a therapy Cobalt unit: AECL Theratron 780. The source is mounted on a rotational head which permit to irradiate along the room (see Figure 2-10). The maximum dose rate reachable is 400 Gy/h with a maximum irradiation area of 13×13 cm^2. The minimum dose rate is set by the maximum distance from the source and it is around 0.12 Gy/h, with an irradiation area of 242×242 cm^2. The dose is measured with a PTW TM30013 0.6 cm^3 air filled therapy level ionization chamber. The USC hall and the irradiation zone in which the DUT can be placed is depicted in Figure 2-11.

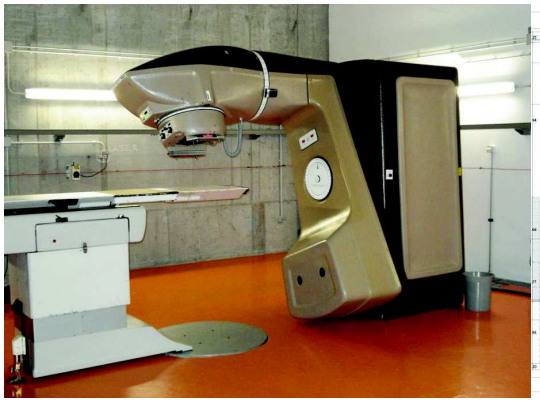

Figure 2-10: AECL Theratron 780 with its rotative arm. The rotation of the arm permits to point the source along the room.

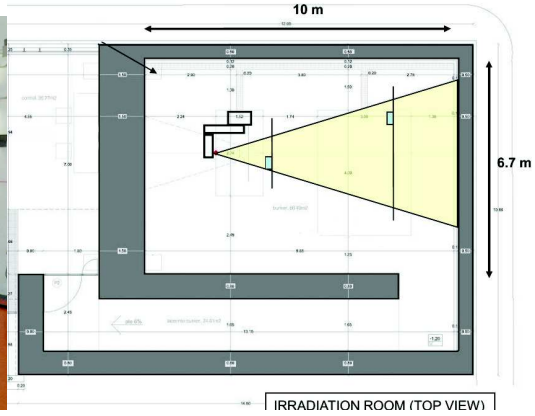

Figure 2-11: Schematic of the USC irradiation hall with the irradiation areas when the head is positioned horizontally with respect to the ground.

2.3.7 H4IRRAD - CERN mixed field Facility

H4IRRAD is a mixed-field irradiation area at CERN, designed for testing LHC electronic equipment, especially large volume racks such as the one for the power converters. The area uses alternatively an attenuated primary 400 GeV/c proton beam slowly extracted from the CERN SPS, or a secondary, mainly proton, beam of 280 GeV/c, both directed towards a 1 m long, 7.5 cm diameter Cu target. The beam that impinges on the target is pulsed; it consists of proton spills that last 9.6 s with a repetition period of around 45 s. At H4IRRAD, during the tests performed in the scope of this work, two pulse intensities were used. The first period was called "low intensity" and was characterized by an intensity of 5.2×10^8 protons per spill, the second period was called "high intensity" with 3.7×10^9 protons per spill. This facility permits to reproduces a radiation field similar to the LHC "tunnel" and "shielded" areas. The "internal zone" close to the target reproduces the tunnel spectra, while the "external area" reproduce the shielded areas. This is possible thanks to a 20 cm thick concrete wall that shields the external zone (see Figure 2-12). Dedicated FLUKA simulations are performed with the geometry information including the specific equipment positions.

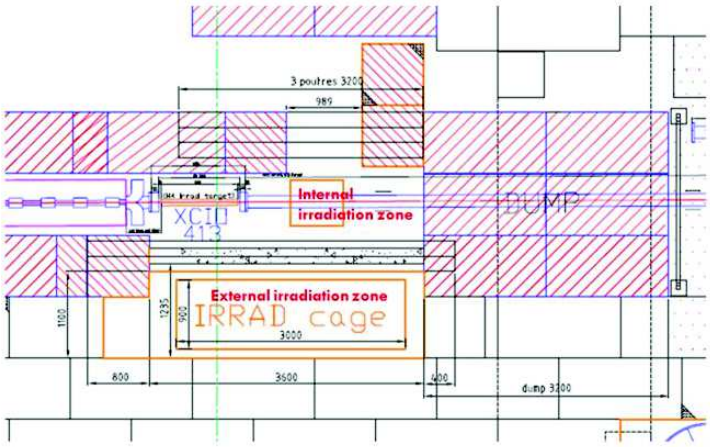

Figure 2-12: PTB low–scattering quasi–monoenergetic neutron facility neutrons test facility

2.3.8 CNRAD - CERN mixed field Facility

The CNRAD test areas [30], depicted in Figure 2-13 are located adjacently to the CNGS (CERN Neutrino to Gran Sasso) target area [31] and offer mixed radiation fields similar to the ones expected in the LHC shielded areas, with the same objective as H4IRRAD of testing bulky electronic equipment. Two 400 GeV/c Super Proton Synchrotron (SPS) primary beam extractions of 10.5 μs duration separated by 50 ms hit the CNGS target with a repetition cycle of 6 seconds. The maximum high energy hadron fluence measured close to the target is equal to 1.9×10^{11} HEH/cm2/week, for a nominal intensity of 2×10^{13} proton on target per extraction and the absorbed dose is between 20 and 25 Gy/week.

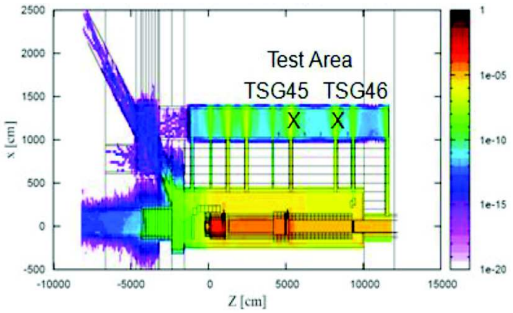

Figure 2-13: FLUKA layout and pictures of the CNRAD test area. The two tunnel locations for the equipment installation are marked with a cross.

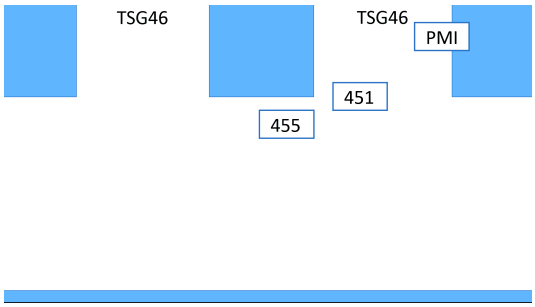

Figure 2-14: CNRAD test positions calibrated with the RadMons with respect to the TSG tunnels.

The test areas are parasitically located with respect to the neutrino production in two tunnel side galleries, named TSG45 and TSG46 (see Figure 2-13). Several positions inside the side gallery and both TSG(45-46) have been calibrated using the RadMons. The positions with respect to the TSG galleries are depicted in Figure 2-14. The operation of CNRAD was linked to the life cycle of the CNGS experiment, which stopped its operation in the 2012.

Chapter 3

Radiation Monitoring System RadMon

A reliable monitoring system is required to maintain the performance, reliability and lifetime of the accelerator infrastructure. The main goal of the RadMon is to measure the distribution and rates of radiation in the accelerator and in its injection chains. A detailed knowledge of the radiation field is necessary for the installation design, relocation or shielding. Radiation monitors were proposed in 2003 [32] with the aim to measure radiation where the equipment is installed and to evaluate the performance of the electronics used under irradiation. Other accelerators had shown that monitoring is indeed very useful to characterize radiation induced failure and measure the efficiency of the shielding structure [33]. The RadMon scope is also to anticipate the possible device degradation and identify instantaneous failures of electronic equipments as caused by radiations. The RadMons are also used to verify the shielding efficiency and benchmark FLUKA Monte-Carlo calculations, used to predict the present and future radiation levels for the LHC locations. Moreover, the RadMon is exploited to monitor the radiation levels in the CERN test facilities where the peculiar LHC radiation mixed field is reproduced for radiation assurance purposes. The RadMon radiation detection network consists of more than 400 monitors that provide an online evaluation of the radiation levels in the LHC and of its injector chain.

In the first section of this chapter the architecture of the previous version of the RadMon is briefly described and then compared with the new version. The test of critical components such as FPGA, voltage regulators and ADC are described and the radiation–induced error mitigation techniques are discussed.

3.1 The RadMon System

The RadMon system is an embedded system with multiple features. Starting from 2003 several developments and revisions have been made to improve the RadMon. In this paragraph we will describe the RadMon Version 5 (V5). We will focus the attention on the hardware side in order to point out later in the chapter the difference with the new RadMon Version 6 (V6).

3.1.1 RadMon V5

The RadMon V5 depicted in Figure 3-1 has been developed starting from 2005 and it started to be operational in the LHC in the 2008. More than 300 units have been installed in the LHC tunnel areas. The key characteristics of the RadMon V5 are:

1. It is a fully commercial system.

2. It has to be radiation tolerant up to a certain dose and certain HEH fluence (detailed later in this paragraph).

3. It has to be able to communicate with an industrial bus present in the LHC.

4. It has to be capable of monitoring the three axes of the radiation effects (SEE, TID and DD).

The first and the second requirements are the most important part for the development of the RadMon. Indeed, due to the high number of units to be installed in the LHC, the RadMon has to be developed entirely using COTS components. This implies a great care in choosing the right components and qualify them with the strategy described in Chapter 2.

The architecture of the RadMon should include a way to communicate with the other systems in the LHC, for this reason the RadMon is equipped with a WorldFIP fieldbus [34, 35] communication link. The WorldFIP bus can communicate up to 1 Mbit/s over 1 km of distance, and it can communicate with 32 stations connected on the same bus.

The RadMon has to embed sensors and commercial components for the measurements of the TID, DD and finally the High Energy hadrons fluence. As already mentioned in the Chapter 2, the RadFets, the PIN diodes and commercial memories are used to pursue the scope.

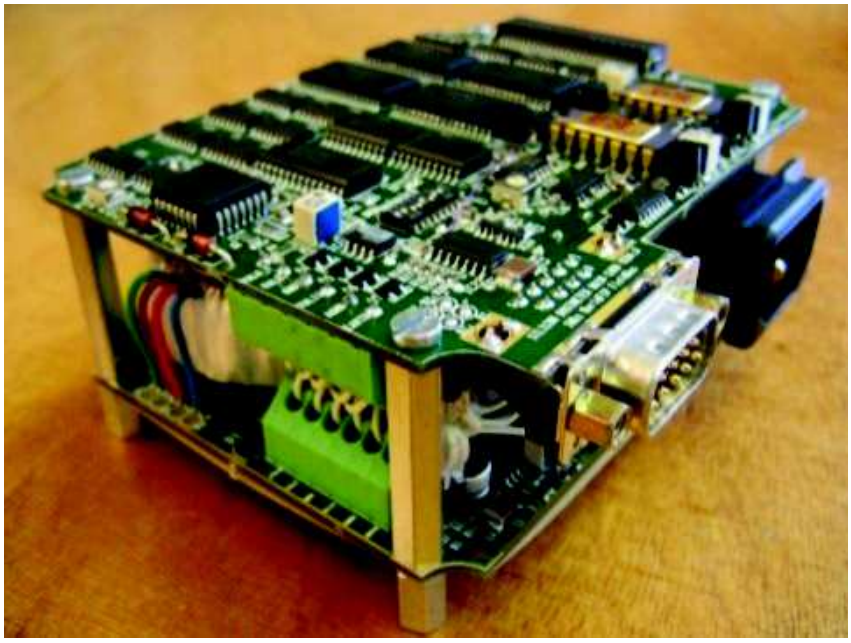

Figure 3-1: RadMon V5 form factor and structure.

3.1.2 RadMon V5 architecture

The architecture of the RadMon V5 is depicted in Figure 3-2. Three main blocks can be recognized in the design.

1. The communication block made by the WorldFIP controller.
2. The readout circuit for the memories used as HEH fluence monitor.
3. The readout circuit for the RadFets and PIN diodes which includes an Analog to Digital converter.

The communication block is the core of the design. Indeed, the MicroFip controller, which implements the WorldFIP communication protocol, manages the entire communication stack and is in charge of the readout timing for the sensors. The controller is able to recover from a deadlock status by means of a watch–dog timer.

The circuit for the readout of the memories is developed using discrete components and is based on a 24 bits free runner counter (made out of three 8 bits counters) which is used to read the addresses of the SRAM memories used as HEH sensors. The value at the output of the SRAM memories is latched in D-flipflop registers and then compared with the initialization pattern. In the version V5 of the RadMon only the pattern “all 0s” was implemented. The single event upsets are stored in a

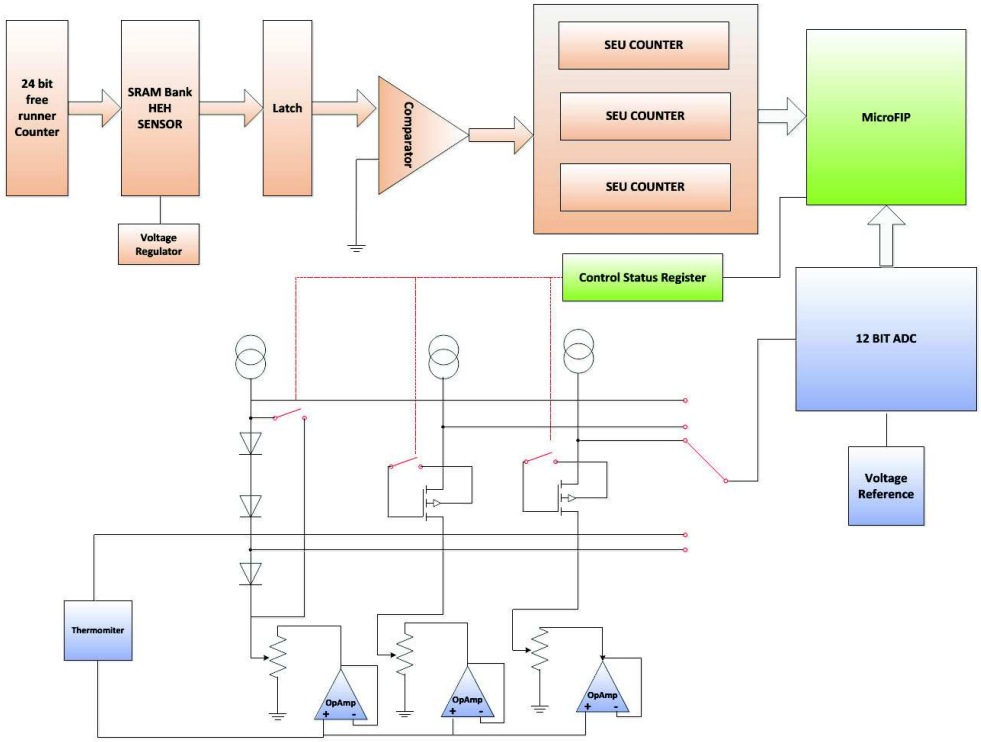

Figure 3-2: Block diagram of the RadMon V5.

triplicated registers directly accessed by the MicroFip. The triplication of the registers introduces a redundancy that is necessary to retrieve the correct value of the SEUs even if a single event occurs on one of the registers. Usually, as we will see for the RadMon V6, along with the triplication a voting circuit is necessary; in the RadMon V5 the votation is carried out at software level on the data read from the MicroFip bus.

The SRAMs used as sensor are grouped in one bank of four devices. The maximum size of a single addressable memory is 512 kbit $\times$ 8 bit, considering four memories the total becomes 16 Mbits. As it will be discussed in the Chapter 5, having more memories increases the resolution of the system and improves the relative uncertainties. The bank of memories is connected to a voltage regulator that can be set to two different voltages (5 V and 3 V) by means of a mechanical switch placed on the RadMon.

The part of RadMon developed to read the TID and DD is entirely analog. In order to communicate with the WorldFip and thus with the external world, a conversion with an Analog to Digital Converter (ADC) is necessary. The ADC mounted on the

RadMon V5 is a 12 bit ADC with a resolution of 2.44 mV and a maximum sampling rate of 125 kSPS. The implication of having a 12 bit ADC will be discussed in Chapter 4.

The analog paths coming from PIN diodes and P–Mos RadFets are connected to the ADC by means of a multiplexer because the ADC has only one channel. The multiplexer is developed using single discrete switches which are closed only one at time. The analog chain is roughly the same for both the PIN diodes and for the P–Mos RadFet. It consists of a current source which feeds the sensors. The main difference is that the current supplied to the PIN diodes is 1 mA while the current supplied to the RadFet is 10 μA. The motivation of using this value of current for the RadFets will be explained in the Chapter 4. The current supply is thermo–compensated in order to have a stable current regardless any variation of temperature. Nonetheless, a temperature compensation has to be done on the RadFets and PIN diodes because of their temperature coefficient (TC). The method used is to compensate the temperature variations by tracking them with an analog thermometer. The temperature is connected to an operational amplifier in buffer configuration, the voltage induced by the temperature sensor is weighted by the potentiometer value and added to the RadFet output. The same structure is used for the PIN diode. The readout electronics for the PIN diodes permits reading the series of three diodes to achieve high sensitivity, while in zones where the fluence of HEH is high a single PIN can be read such as to not saturating the ADC.

In the version V5 of the RadMon a deported module was added in order to measure in zones where the radiation level is high (Figure 3-3). The cable connecting the "motherboard" and the module can be as long as 200 meters but the standard solution is 50 meters. On the deported module the RadFet and PIN diodes can be mounted. The memories can only be mounted on the motherboard because of the strict timing constraints that have to be met.

3.1.3 RadMon V5 operational issues and controversy

The RadMon V5 was developed following some radiation test strategies but not so much documentation is available. The main components such as the ADC, voltage references and analog switches have been tested but few information on the tests are available. Some of the issues related to the radiation effects were seen in operation.

The deterioration of some components performance invalidated the life–time of the RadMon. One of the worst effects was the increase of the current consumption of the voltage regulators which are used to feed several components of the RadMon. This was the main cause of failure for the RadMon which resulted in only being able

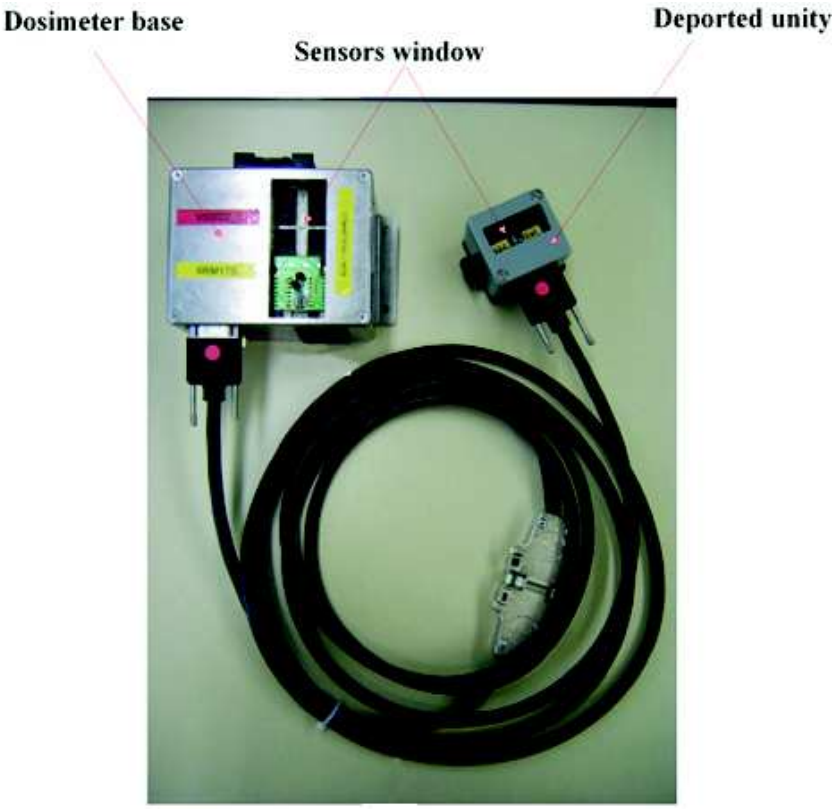

Figure 3-3: Main Board of the RadMon V5 with the deported module.

to stand 80 Gy of TID during the LHC operation. The possibility to operate at higher radiation level, as said in the previous paragraph, was exploited by using a deported module.

Some SEUs on the MicroFip controller have been noticed during the operation but they are not critical since they lasted for one reading cycle only. The watch–dog worked in several cases showing that a reset of the controller was necessary to establish the correct working functions.

One of the main hardware problems with the RadMon V5 is the necessity to manually change the switches on the board to operate with different settings. For instance to change the supply voltage of the SRAM memories it is necessary a manual intervention, that can take long and requires accessing in the location of the LHC where the RadMon is placed (the access usually is restricted).

These, along with the necessity of higher sensor resolution, are some of the reasons that led to develop another version of RadMon, which can be more radiation tolerant and that can be configured remotely without the need of human intervention.

3.1.4 RadMon V6

In addition to the requirements inherited from the RadMon V5, the RadMon V6 has to fulfill further constraints to face the problems encountered during the operation of the RadMon V5, integrate new features to improve the maintainability of the system and improve the measurements accuracy of the system.

The new requirements for the RadMon V6 are:

1. Higher radiation tolerant design ($>$ 200 Gy).
2. Modular architecture for an easy replacement and easy integration of new sensors.
3. Remote reconfigurability.
4. Improved measurement accuracy.

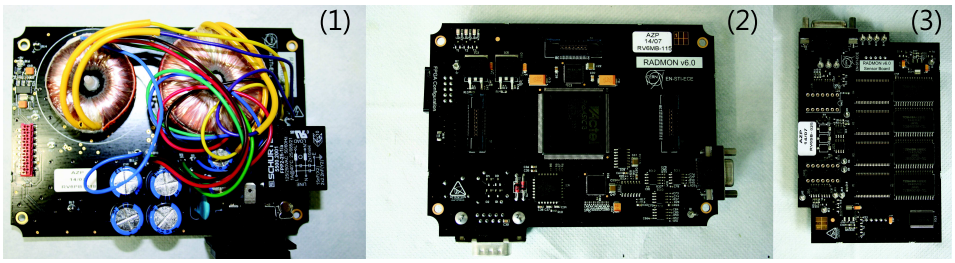

Figure 3-4: RadMon V6: (1) Power Board , (2) Main Board , (3) Sensor Board.

The higher radiation tolerance is a necessary requirement in order to reduce the Mean Time Between Maintenance (MBTM). The higher radiation tolerance for the new version of the RadMon has been achieved thanks to the extensive radiation test campaigns carried out on all the components of the board. Some of these tests will be analyzed later in this chapter. The RadMon V6 is depicted in Figure 3-4. It consists of three modules combined together, (1) the power supply board, (2) the main board, and (3) the sensor board. The power supply board allows connecting the RadMon directly to the 230 V main supply. The board is developed in such a way as to not contain any power switching element that can be susceptible to destructive events such as Single Event Burnout or Single Event Latchup. All the regulation is made by toroid transformers, passive components and linear regulators for the positive and negative supplies necessary to the correct operation of the RadMon. The power supply board is capable of supplying a total power of 7 Watts considering all the outputs.

The main board is the core of the RadMon, a block diagram is depicted in Figure 3-5. The entire main board is built around the Actel FPGA ProAsic3, which is a Flash FPGA particularly used in harsh environments such as the space and avionics for its intrinsic low susceptibility to SEEs. In the paragraph 3.1.5, a detailed description of the mitigation techniques needed to cope with the radiation effects are presented. The FPGA covers several functionalities that in the previous version of the RadMon were done by multiple discrete devices. The MicroFip device that in the previous version of the RadMon was the "brain" of the RadMon, now is embedded in the FPGA thanks to the work of [36]. The advantages of having the MicroFip embedded in the FPGA include the possibility to mitigate the SEE directly in the firmware, the cost reduction (only one component is necessary compared to the tens of devices necessary to let the MicroFip work) and the possibility of not having to be linked with only one supplier for the furniture of MicroFip devices. In any case, to communicate with the WorldFIP bus is still necessary a FIP driver (DriverFIP) which implements the protocol at the physical level (PHY).

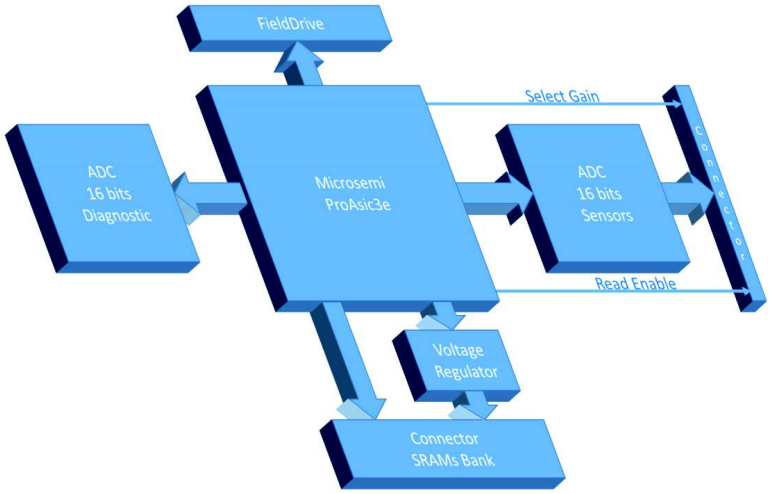

Figure 3-5: Block diagram of the RadMon V6 main board.

The FPGA implements all the logic and states needed to communicate with the external ADCs, to drive and analyze the data coming from the SRAM memories and manages the reset circuit. Moreover, the FPGA is connected directly to several switches present in the RadMon for an automatic reconfiguration of some operational parameters. Most of them will be described later.

As depicted in Figure 3-5, the new RadMon contains two ADCs, one is for monitoring purposes and another for the sensors readout. The ADC is an essential com-

ponents for the RadMon and for this reason, great care was taken in choosing and characterizing one suitable for this application. The ADC used in the RadMon V6 exhibits higher performances with respect to the one used for the RadMon V5. Indeed, this ADC is a 16 bits device with a sampling rate up to 250 kSPS capable of recording signals from 8 independent channels synchronously. The improvements brought by this kind of ADC are reflected on several parameters. Indeed, being the ADC a 16 bits it has a resolution of 152 μV (considering its $\pm$ 5 V of full scale range), 16 times higher than the one of the RadMon V5. Moreover, being capable of recording 8 channels at the same time, it reduces the number of devices present on the board (no swithces acting as multiplexer are needed) and increases the number of signals to be recorded with respect to the RadMon V5. The monitoring ADC keeps trace of all the health signals from the RadMon, such as the supply voltages, the amount of current supplied and the temperature of the main board. All these signals are necessary to understand if the RadMon has some problems or if it should be substituted due to a degradation of the characteristics of some devices. The second ADC is a part of the sensors' acquisition chain. It converts in a digital form the voltages of the RadFets, PIN diodes and temperature sensors; it is still part of the RadMon main board.

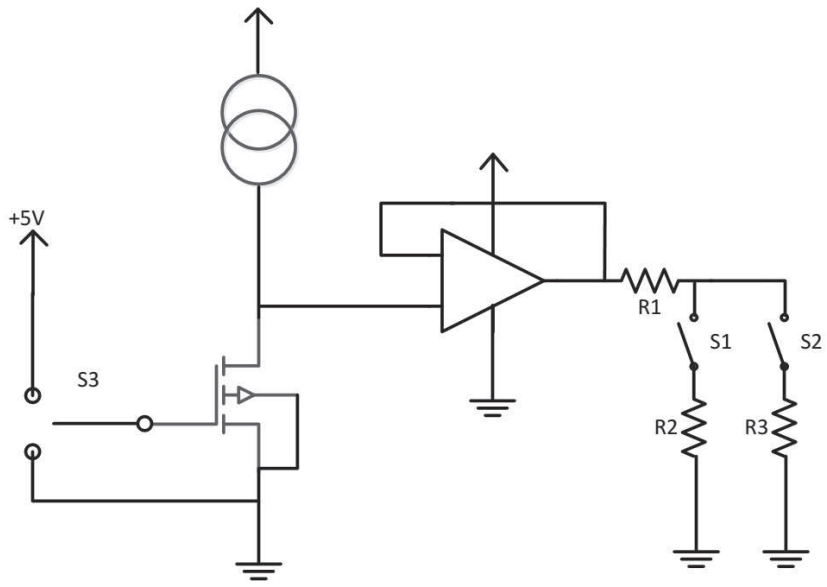

Figure 3-6: Acquisition chain of the RadFet with the possibility to reduce the voltage of the RadFets output to avoid the early saturation of the ADC.

The RadMon Sensor board is constituted by the RadFet, PIN diodes readout

circuit and the SRAM memories block. The acquisition chain of the analog sensors, depicted in Figure 3-6, is similar to the one of the RadMon V5 but some important changes have been made in order to improve the resolution and the dynamic range. The sensors voltage passes through an amplifier in buffer configuration; at its output is possible to select, by means of two switches, the values of the resistor R2 and R3 in order to divide the amplitude of a factor 10 or 2. The voltage dividers are used to increase the dynamic range of the read by reducing the voltage at the input of the ADC. The switch S3 in Figure 3-6 is used for the selection of the bias condition, as it will be explained in Chapter 3. This solution is very useful when the deported module is used and if it is placed where the radiation levels are high and the risk of saturating the ADC is real.

The RTD temperature sensor placed in proximity of the RadFet and PIN diodes records the temperature close to these devices. The temperature compensation in the new version of the RadMon is directly done in software without the needing of changing manually the temperature coefficient when changing the type of RadFet placed on the board.

The SRAM memories used as the HEH sensor are grouped in two banks of four devices in the new design of the RadMon. The Toshiba memories, used in the previous version of the RadMon are used in one bank. The new Cypress memories, used for their high cross section as described in Chapter 5, are used in the other bank. The total amount of SRAM addressable is 16 Mbit for the Toshiba and 32 Mbit for the Cypress for a total of 48 Mbit. The possibility to configure them with different power supplies is achieved by using the voltage regulators whose outputs are selected by several analog switches controlled by the FPGA. The power supplies that can be generated are 1.8 V, 2.5 V, 3.3 V and 5 V.

The use of the new Cypress memories along with the Toshiba ones drastically improve the accuracy of the measurements. Moreover, a huge work of calibration and characterization have been carried out on the "old" and "new" sensors and this will be the topic of the next chapters.

3.1.5 FPGA implementation and radiation mitigation techniques for the RadMon system

The FPGA is the "brain" of the RadMon. It permits to communicate with the WorldFIP bus, manages the peripherals, such as the ADC and the SRAM memories and is in charge of the signal processing. Its functionalities are necessary for the correct work of the RadMon. For this reason, the choice of the FPGA is critical. The previous

chapter gave the guidelines on how to choose and test a COTS component. Following those guidelines, the Microsemi ProAsic3E familily was chosen. The ProAsic3 FPGAs are based on the flash technology to store their configurations, conversely the Xilinx and the Altera FPGA are based on the SRAM technology. The flash technology is intrinsically less prone to SEE with respect to the SRAM based. Unfortunately, the performances of the Flash based FPGAs are below the SRAM ones, but these are more than sufficient for the scope of the RadMon.

The mitigation techniques against radiation effects for the FPGA are several and there are multiple issues to face when changing from one type of device to another. One of the most important differences between the Flash based FPGAs and the SRAM based ones is the susceptibility to SEE also at the configuration level. Thus, having configured an SRAM FPGA with the desired design, it is possible that a SEU changes the configuration of the FPGA and hence also the implemented design. Several mitigation techniques for this issue exist; the one used for the COTS component is the scrubbing. The scrubbing consists in a continuous refresh of the information stored in the configuration registers in order to correct the error induced by the radiation. The scrubbing, usually done on the entire memory, takes time and uses power.

The Flash based FPGAs store their configuration in a floating gate structure which is not affected by single events. The embedded SRAM blocks and memory elements such as Flip–Flops are present in these kind of FPGAs and they can be used in the design of the application. These elements can still suffer of single event effects. Thus, one mitigation technique is devoted to the correction of corrupted data due to single event upset in the memory elements. The most used techniques in this kind of the FPGA is the Triple Modular Redudancy (TMR). The typical TMR scheme adopted is depicted in Figure 3-7, and consists in the triplication of the memory elements and the insertion of a voter circuit. The voter implements the logic function on the three outputs A,B and C:

$$Y = AB + BC + CD \tag{3.1}$$

If one memory element is hit by a SEU, the voter has two right output over three thus leading in a correct output. The TMR is implemented on all the register elements of the RadMon design to assure the correct function of the developed application.

The triplication technique can be used for any kind of memory element in the design, such as the Flip–Flops and the embedded SRAM banks, but for the latter another strategy can be used to mitigate the single event effects. Indeed, the SRAM banks are limited in the FPGA and the triplication is not always possible; thus, an Error Detection and Correction circuit (EDAC) can be used. While recovering the data, a decoder first determines if a message read from the SRAM is valid. This step is

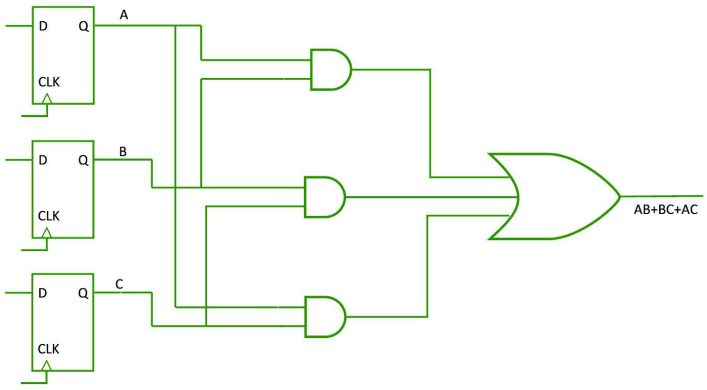

Figure 3-7: Triple Modular Redundancy with the voter scheme.

called error detection. If one error is detected, the decoder finds a valid message that is most similar to the one that is read and corrects the single error. In the RadMon design the embedded SRAM banks are used only in the communication part and they implement the First In First Out (FIFO) memory used to store the values to be sent on the bus. Thus, the low amount of SRAM used permits to triplicate the entire SRAM devoted to the FIFO; the correction of an SEU on the memory bank is done by the insertion of a voter.

3.2 RadMon quality assurance in radiation environments

In this section the tests carried out on the RadMon in order to qualify its radiation hardness are reported and discussed. Each of the RadMon components was qualified and the entire system was tested.

The parts which can be sensitive to three effects of radiation; Single Events effects, TID and DD, were tested in PSI with protons at 230 MeV. The tests of some non–complex devices will be described followed by the most important part tested such as the FPGA, the ADC. The tests have been carried out also on the entire system and the results will be discussed.

3.2.1 Voltage Regulators

The radiation tests on the voltage regulators and on the current sources have been carried with protons at PSI configuring the devices as in the final application of the RadMon. Table 3.1 reports the configurations and the run characteristics. The

Table 3.1: Voltage regulator configurations for each irradiation run

Run	DUT	Input	Output	Voltage	Output		Dose	Fluence	TID
	DUT name	Voltage [V]	Voltage [V]	drop [V]	current [mA]	[MeV]	rate [rad/s]	[p/cm2]	[Gy]
1	LM317D2T	+7.3V	+5V	2.3V	250	230	9.3	6.0×10^{11}	320
2	LM317EMP	+5V	+3.3V	1.7V					
2	LM317EMP	+5V	+1.5V	3.5V	50	230	9.3	$6.0 \times 10^{1}1$	320
3	LM317EMP	+7.3V	+5V	2.3V					
3	LM317EMP	+7.3V	+3.3V	4V					
3	LM317EMP	+7.3V	+2.5V	4.8V	100	230	9.3	6.0×10^{11}	320
3	LM317EMP	+7.3V	+1.8V	5.5V					
4	LM337IMP	-15V	-5V	10V	50	230	9.3	6.0×10^{11}	320

tests are carried out with protons at 230 MeV, with a flux of around 2×10^8 cm^2/s equivalent to a dose rate of 9 rad/s reaching a final TID of 320 Gy.

The DUT LM317D2T and LM317EMP are different for two reasons: they are fabricated by two different manufacturers and they are encapsulated in two different packages. Thus they have to be tested as two different devices. The LM317 devices are devoted to provide as output 5 V, 3.3 V, 2.5 V and 1.5 V, while the LM337 provides the -5 V. The test circuits are depicted in Figure 3-8 and 3-9; the circuit topology is the same used for the RadMon. The resistance R1 and R2 in the test circuits are selected to give the desired output voltage and current considering the equation:

$$V_{out} = 1.25 \times \left(1 + \frac{R2}{R1}\right) + I_{adj} \times R2 \tag{3.2}$$

The term I_{adj} is the current flowing in the ADJ pin of the regulator.

The tests are carried out in order to track and measure the variation of the output voltage as function of the TID for different currents supplied to the load. The output voltage, the voltage and the current on the pin ADJ are recorded during the test.

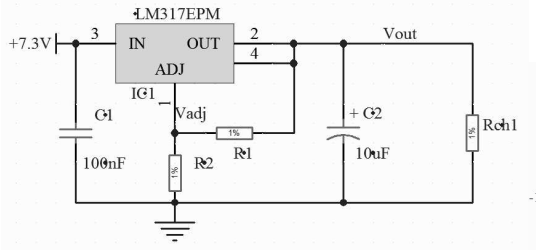

Figure 3-8: Test circuit for the LM317 positive regulator.

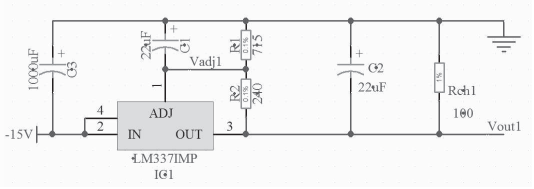

Figure 3-9: Test circuit for the LM337 negative regulator.

The output voltages of four devices regulating a 5 V output are depicted in Figure

3-10. When the beam was off a slight annealing can be noticed, meaning that using the device with a lower dose rate could improve the radiation hardness. However, if the device is prone to the Enhanced Low Dose Rate Sensitivity (ELDRS), the degradation could be worse and a safety margin should be applied (See Chapter 2).

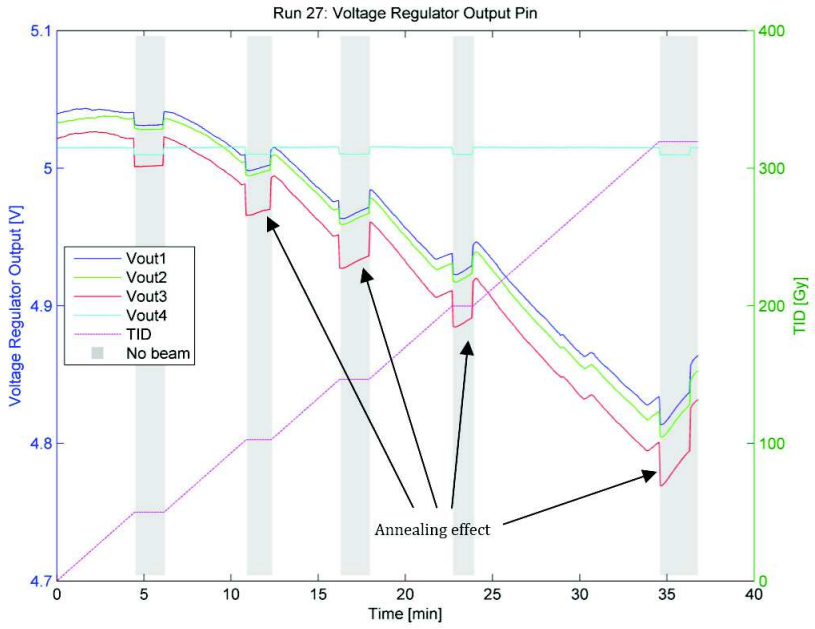

Figure 3-10: Voltage output of three voltage regulators with an output voltage of 5 V. The output voltage of the three regulators in the beam are Vout1 to Vout3, while Vout4 is the reference regulator not irradiated.

No destructive events were registered during all the runs. The maximum drift of 5% was observed for the LM317D2T while for the other is less than 3% (see Table 3.2). The impact of these variations on the RadMon is small because other components shown in the next paragraphs fail before this value. Despite the similar results for all the devices tested with protons an issue arose testing with neutrons. Indeed, the LM317EMP failed during a test with neutrons, having cumulated 1×10^{12} n/cm^2. This result led to the use of only one type of regulator, the LM317D2T, which can work properly beyond to a neutron fluence of about 3×10^{12} n/cm^2 [37]. This result also underlines the importance of a proper radiation testing considering all the effects that the device can encounter in its operation as explained in the paragraph on the test strategy in the Chapter 2.

Table 3.2: Summary of the PSI test results on the positive and negative voltage regulators.

Maximum Drift	LM317D2T	LM317EMP	LM337IMP
% of the output	5%	2.50%	1.30%

3.2.2 FPGA

The tests carried out on the FPGA, have been performed by the BE-CO group [38]. In this paragraph the main results are reported and discussed in order to point out the good and the bad features discovered. As previously mentioned the FPGA chosen is a flash based Microsemi ProAsic3E. The tests have been carried out on an FPGA which contains 400k of logic gates A3P400E. The tests have been performed to measure the TID life–time and the SEU susceptibility. The tests have been also carried out to check the radiation tolerant implementation of the nanoFIP slave interface developed in the FPGA firmware.

In a preliminary test [38] the FPGA reached around 400 Gy before failure, and a fluence of 7×10^{11} pp/cm^2. Despite that, a second test [39] was carried out to probe whether the TID life–time could be extended by reprogramming the FPGA. As explained in [40], the TID life–time is limited by the the charge loss in the FG devices (whether in the erase or the program state). Therefore, a first TID mitigation solution would be to attempt to restore that charge to these FG cells. This refresh could simply be done by erasing and reprogramming the flash FPGA. Unfortunately, the programming circuit is sensitive to TID and after cumulating a certain amount of dose an inability to reprogram the core arises. Actel found that this limit is around 400 Gy with X-rays [41], and the limit of the core extends to 660 Gy (based on 10% degradation of the propagation delay). Assuming a pure analogy the reconfiguration circuitry failure was expected to be manifested at the same value but instead, it was concluded that the limit is approximately 200 Gy: all reconfiguration attempts performed at 180 Gy were successful; one attempt at 230 Gy failed; at 200 Gy one attempt failed and two were successful.

The SEU susceptibility was carried out by counting the numbers of errors on the communication between the FPGA and the PC. In total 1×10^{13} p/cm^2 were accumulated by the 12 DUTs with TMR and no SEU appeared. The FPGA that was synthesized without TMR experienced SEUs in the form of data errors and communication losses, but it was always able to resume alone its functionality. The error cross section found for the DUT non–triplicated was about 6.8×10^{-11} cm^2.

3.2.3 ADC

The ADC is a fundamental part of the RadMon. An 8–channel, 16-bit SAR converter, based on BiCMOS technology has been chosen (ADC MAX11046) . Each channel has independent Sample-Hold circuitry and ADC digitizer, allowing for a real parallel reading of the eight inputs. The SAR architecture is considered an optimum trade-off for applications with dynamic voltage input and medium sampling frequency (up to 2 MSPS).

We considered various aspects of radiation effects on the ADC candidate. We performed a ^{60}Co gamma irradiation to verify the radiation hardness of the ADC. The objectives of the test are to measure the variation of the main parameters of the ADC MAX11046 and to assess its TID life-time. The tests have been carried out at the Fraunhofer institute with a dose rate of 4 Gy/h.

Five boards have been irradiated. Four of them were irradiated in passive mode without the power supply, while the board 5 irradiated up to 500 Gy, was continuously supplied and monitored. Each board contains 3 ADCs which share the same power source. The ADC needs two power supplies: one for the digital part and the second for the analog part; the current consumption on both the power supplies were recorded during the irradition.

The digital power supply of the board 5 (online measurements) was monitored and the current started to increase at 160 Gy at a rate of 1.2mA/Gy. At 240 Gy the current increased with a higher slope (10mA/Gy) (see Figure 3-11). These increments on the analog current happens at around 230 Gy (Figure 3-12). These measurements are in agreement with the results of the proton irradiation at PSI where the current increase was registered at 180 Gy and 160 Gy for the Digital and the Analog supply, respectively [42].

In Figure 3-13 the total power consumption (Analog + Digital) for one ADC is extrapolated from the measurements, dividing the analog current by three and summing the Digital Current. This study helps understanding if the RadMon power board, which is able to provide a maximum of 500 mA, can handle the total current consumption of the ADC. Considering that the RadMon has two ADCs, the current budget for one ADC has been fixed at 500 mA. The Figure 5 shows that the RadMon power board can supply two ADCs up to 260 Gy. At around an accumulated TID of 260 Gy the ADC fails, thus setting the high–end limit for the lifetime of the entire RadMon.

All the boards that were tested in passive mode show no TID effects up to 500 Gy. This highlights the importance of the tests strategy which foresees that online measurements under irradiation must be carried with the real bias conditions. Table

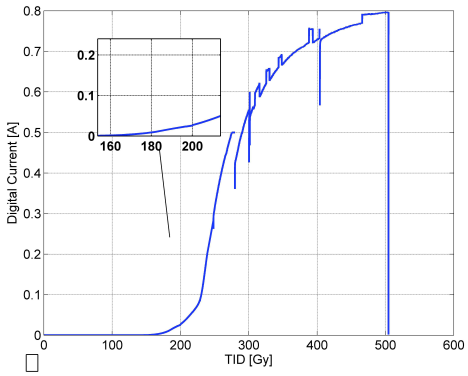

Figure 3-11: Power consumption for the Digital Power supply (for 3 ADCs).

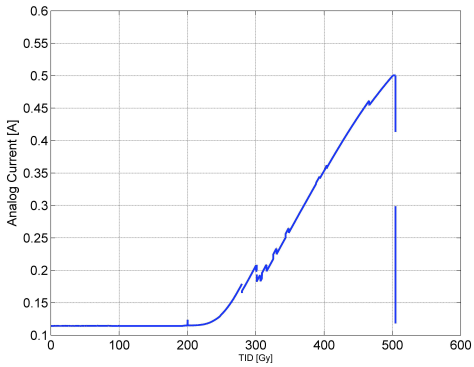

Figure 3-12: Power consumption for the Analog Power supply (for 3 ADCs).

3.3 summarizes the results for all the boards.

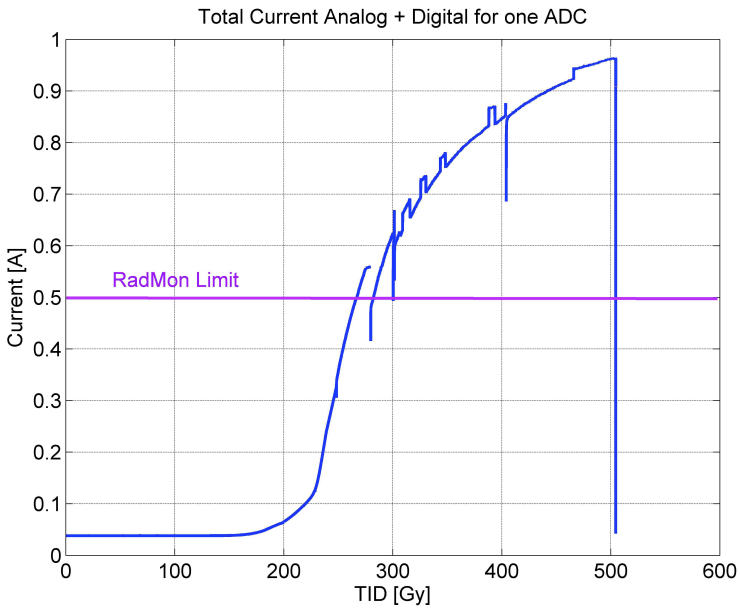

Figure 3-13: Total current consumption combining Analog and Digital power supply for a single ADC. The maximum ammount of current that the RadMon can supply to a single ADC is reported.

Radiations can also cause a SEU in the digital section of the ADC. The criticality of a SEU depends on the application and can be estimated with a fault injection technique [43]. A SEU can also affect the ADC clock circuitry resulting in a Single Event Function Interrupt (SEFI) which blocks the conversion for many successive

Table 3.3: Summary of the ^{60}Co radiation test results.

	Board 5	Board 1	Board 2	Board 3	Board 4
Test Conditions:	Active	Passive (only fed by the supply voltage)			
	ADC1-2-3	ADC1-2-3	ADC1-2-3	ADC1-2-3	ADC1-2-3
TID	No Effect	No Effect	No Effect	No Effect	No Effect
0-159	No Effect	No Effect	No Effect	No Effect	No Effect
160	Digital Current Increase	No Effect	No Effect	No Effect	No Effect
200	Digital Current Increase	No Effect	No Effect	No Effect	No Effect
230	Digital and Analog Current Increase	No Effect	No Effect	No Effect	No Effect
300	Acquisition Fail	No Effect	No Effect	No Effect	No Effect
400	Acquisition Fail	No Effect	No Effect	No Effect	No Effect
500	Acquisition Fail	No Effect	No Effect	No Effect	No Effect

sampling periods. Single Event Transient (SET) on the voltage reference circuit may also result in a series of wrong conversions. Moreover, the voltage reference value can be affected by TID, resulting in a voltage drift, thus a change of the nominal value of the Least Significant Bit (LSB) amplitude. Finally, we considered single-event latch-up and performed experiments to screen for it, since the LHC radiation environment is characterized by the presence of hadrons at high energy (up to 1 GeV). Over the past years, several techniques have been established to determine the cross section of an ADC [44–48]. Usually the detailed architecture of a COTS component is not known, so the dependence of the SEE cross section on the input voltage cannot be estimated a priori. The calculation of the cross section should be addressed with time-variant signals at the analog input if the ADC is used to acquire such a class of signals. However, the continuous acquisition of a time-variant signal can be very demanding when the sampling rate and the ADC resolution are high. Thus, the simplest technique to emulate an AC input voltage is to excite the device with different DC input levels [44]. For a given input level, the ADC output must fall in a specific range of codes; the width of such a range depends on the test vehicle noise. Nevertheless, a SEFI which blocks the conversion on the expected ADC code could not be detected when a DC signal is used as test signal. A more complex method is the beat frequency test, commonly used for very fast flash ADC (up to GS/s) [46,47]. However, this technique lasts too long to stimulate all the ADC codes if the sampling rate is in the order of hundreds of kHz and the ADC has high resolution (more than 16-bit). The test methodology proposed by Berg et al. in [44], called "Four Point window Scheme" (FP), differs from the beat frequency method. It is a dynamic test which enhances the observability of SEUs by acquiring 4 points of a sine wave. This test methodology can be used to discriminate the different origins of the SEUs (Clock circuit, signal filtration, etc.).

Furthermore, the correct test methodology to apply also depends on the constraints imposed by the testing facilities, such as the noise level, the distance between the Device Under Test (DUT) and the test controller, and so on.

Two methodologies have been used to qualify the selected 8-channel ADC with SAR architecture. The first method consists in applying a constant input signal and varying its value as a step function to cover different levels of the input range. This method is referred hereafter as Static Input Signal (SIS). The validity of this method has been verified on a Flash ADC [49]. We developed a second method that applies a time-variant input signal, and is referred to hereafter as Dynamic Input Signal (DIS). The acquisition of the entire waveform can put in evidence the specific error signature, as explained in [44]. The Dynamic figures of merit, such as the Effective Number Of Bit (ENOB), defined in the standards [50], are evaluated continuously during the test and linked to the SEU cross-section.

The SIS test is performed by feeding the ADC with a DC input voltage on each channel. The measurements are divided in two phases: (i) the calibration and (ii) the radiation test. During the calibration, the tester board retrieves and stores the maximum and the minimum ADC code of each channel for a given input voltage. Those values are used in the second phase of the radiation test as thresholds of a dead band, which is not considered for the SEU counting. If an ADC code falls out of the threshold values during the irradiation, a SEU happened. The wrong ADC code and its number of occurrences are saved on the FPGA. The number of occurrences defines the total number of SEUs. Then, by knowing the accumulated fluence of particles, the cross section of the DUT is evaluated per channel. The monitoring of the reference voltage is necessary in the SIS test method in order to verify that the ADC codes which fall out of the dead band are not caused by the drift of the reference voltage, due to the TID. In the latter case, the wrong ADC code is constant and a new calibration is required. By monitoring current consumption, we can check for latch-up events.

The DIS test uses a metrological approach to extrapolate the parameters of the ADC dynamic performance, such as the ENOB, under irradiation [50]. The ENOB is a significant figure of merit for showing how the ADC is impacted by the radiation when a time variant signal, namely a sine wave, is applied. Considering a sine wave of specified frequency and amplitude as input signal, the Effective Number Of Bits of the ADC is defined as [50] :

$$ENOB = log_2\left(\frac{Fs}{rms_{noise} \cdot \sqrt{12}}\right) \tag{3.3}$$

$$rms_{noise} = \sqrt{\frac{1}{M}\sum_{n=1}^{M}|y_n - y'_n|^2} \tag{3.4}$$

where Fs is the full scale of the ADC and the rms noise is expressed by the 3.4 with y_n the ADC samples and y'_n are the values of a sine wave which best fit the points y_n.

For this test, the data are sent in real time to a PC via an Ethernet connection. The PC stores all the ADC sampling codes and computes the sine fit algorithm in real time. The variation of the ENOB during the irradiation will permit to measure the SEU cross section and to study how the SEUs affect the dynamic performance of the ADC. Possible SEFI, resulting in a significant and sudden decrease of the ENOB, would be detected.

At PSI, the SIS and the DIS methods have been used. With the SIS method three ADC chips were tested with a 230 MeV proton beam to a fluence of 4×10^{11} protons/cm^2, corresponding to a TID of 20 krad(Si). Different input levels were applied (-2.5 V, -1 V, 0 V, 0.1 V, 1 V, 2.5 V, 4.8 V). The dead band, evaluated in the calibration phase, was 4.8 mV, which corresponds to 32 LSBs. Therefore, the first 5 bits of the ADC code are not considered in the evaluation of the SEU cross section. Table 3.4 reports the summary of the SEUs per each channel by counting the SEUs collected on the three DUTs. The total number of SEUs has been used to evaluate the cross section per channel, which resulted to be 9.5×10^{-12} cm^2 with a ± 1 uncertainty bar of $\pm 9\%$. The variation of the reference voltages is reported in Table 3.5 for the three devices. As expected, a drift of the reference voltage caused many SEUs since it affected the LSB amplitude. The wrong code is just one LSB out of the dead band. Those cases cannot be counted as SEUs. Thus, the irradiation was stopped several times to run a new calibration procedure and take into account the variation of the VREF. Finally, no SELs were observed up to a total fluence of 4×10^{11} protons/cm^2 at room temperature and at 70 °C.

Table 3.4: SEU counts summary with the SIS method.

Channel	SEU COUNTS	Channel	SEU COUNTS
Channel 0	36	Channel 4	28
Channel 1	31	Channel 5	31
Channel 2	37	Channel 6	27
Channel 3	37	Channel 7	38
Cumulative			265

Table 3.5: Voltage reference drift with a proton irradiation.

DUT	ADC 1	ADC 2	ADC 3
Drift [mV]	-2.5	-4	-3.8
TID [krad(Si)].	20.8	21	21.4

The DIS method was carried out on two DUTs. The input sine wave had an amplitude of 9 V peak-to-peak and frequency of 1 kHz; the ADC sampling rate was 100 kSPS. Given the significant amount of data to acquire, only one channel per ADC was monitored. The ENOB value was calculated on 1000 ADC samples not overlapping, corresponding to 10 periods of the input sine wave. A dry run was conducted before irradiation to evaluate the ENOB of the device, which we measured to be 12.94 bits with a standard deviation of 0.03 bits. The minimum value of the ENOB during the dry run is taken as a reference threshold to distinguish radiation effects: a SEU is counted if the ENOB value is lower than the threshold level. The

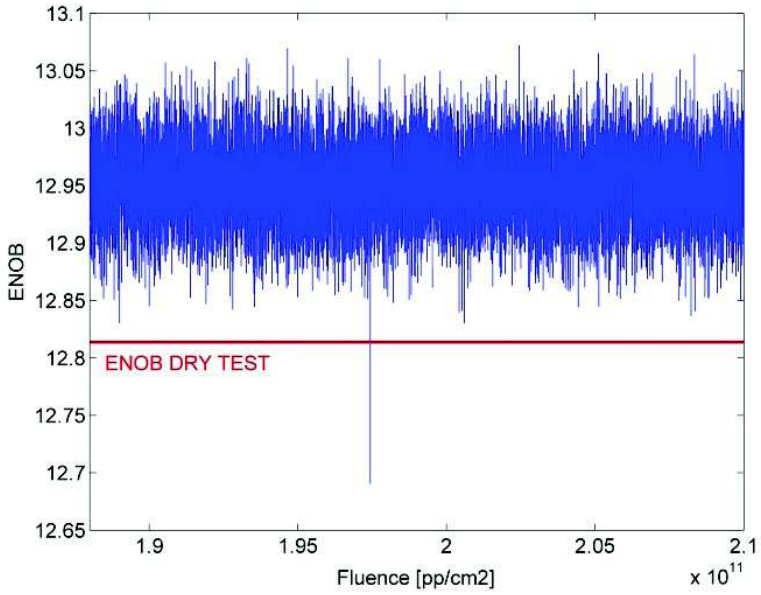

Figure 3-14: The ENOB measurement during the irradiation shows the effect of an SEU. The red line indicates the reference threshold which was evaluated during the dry run test.

typical signature of a SEU is depicted in Figure 3-14. The ENOB collapses under the threshold value, reaching 12.69 dB. The difference between the acquired data and the best fit of the sine wave, computed by the three parameters algorithm, triggers a valid

SEU count (Figure 3-15). The SEU causes an error of about 7.4 mV with respect to the expected value. This result is in agreement with the numerical simulation predictions (Figure 3-16) [51]. In fact, an error of 7.4 mV implies that a SEU affected the ADC code on the 6th bit and decreased the ENOB value to 12.7 bits. By using

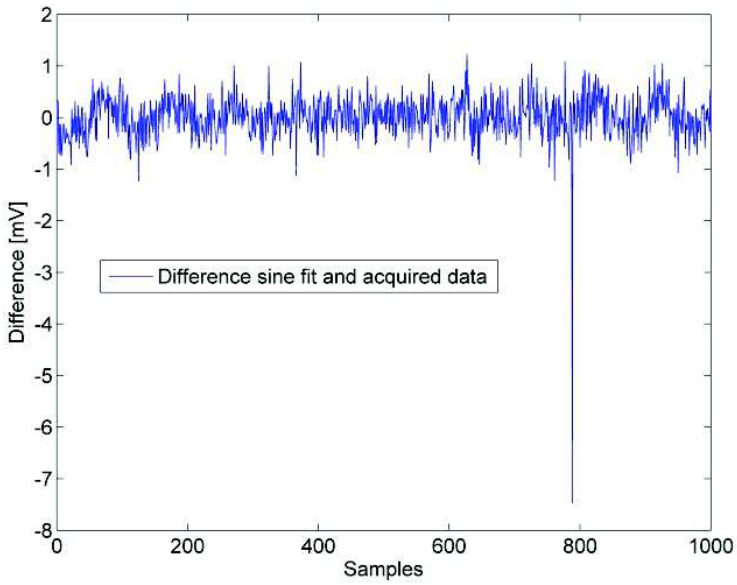

Figure 3-15: The difference between the fitted sine wave and the acquired values shows the evidence of a SEU.

this method on only one channel, a total of nine SEUs (six on one and three on the other) were recorded on the two DUTs. The cross section per channel would be 8.2×10^{-12} cm^2 with a $\pm 1\sigma$ uncertainty bar of $\pm 30\%$. The statistics of the events are too low for a comparison with the SIS method. In the Figure 3-17, the amplitude of the sine waves, estimated with the sine fit algorithm, is represented as a function of the drift of the reference voltage. The drift is 7 mV for both the ADCs at a TID of 28 krad(Si). The DIS method shows how the variation of the voltage reference affects the amplitude measurements and does not require performing the calibration phase during the tests.

The drifts of analog parameters, such as the reference voltage, did not impose the need of a new calibration and its effect on the ADC performance was put in evidence. In fact, the accuracy of the measurement of the sine wave amplitude is affected. All those features were studied by means of numerical simulations and were confirmed by the experimental results. Concerning the evaluation of the cross section, the DIS method permitted to discriminate SEU by masking the first 5 least significant bits, as

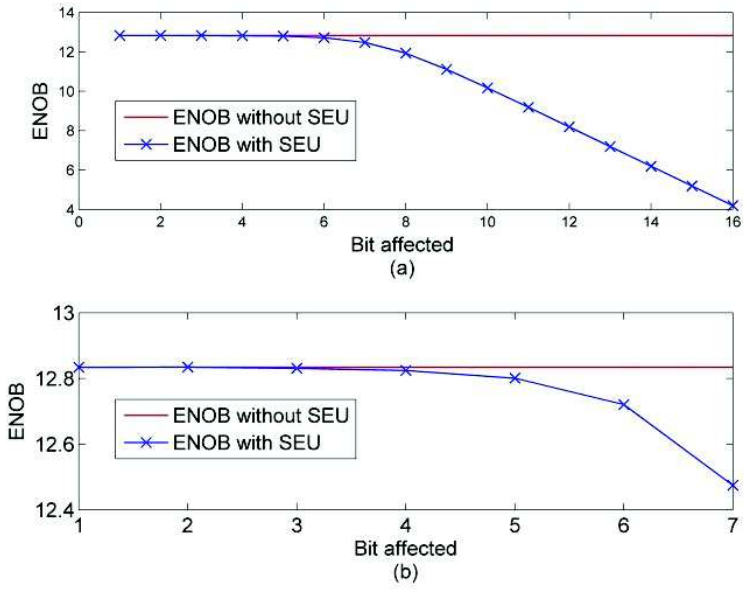

Figure 3-16: Simulation of the ENOB value of a 16 bits ADC compared to the ENOB value affected by an SEU. (b) Zoom in the region in which the ENOB starts to decrease significantly.

the SIS method. The use of the three parameters algorithm allowed the localization of the SEU on the sine wave and the estimation of its amplitude. A SEU cross section per channel of 9.5×10^{-12} cm^2 was measured by using the SIS test. Although the number of SEUs per channel, recorded by using the SIS and the DIS methods, are consistent, the low number of events does not yield a small uncertainty to affirm that the cross section values are in agreement. As a matter of fact, the data rate of the acquisition system for the DIS method is very high and it was not possible to acquire more than one channel per device to collect more events. The SIS method gave meaningful data for a few static inputs because 8 channels were sampled during the beam run. While the DIS method gave very few failures, it was able to sample the full input range. The statistics of the DIS method can be improved if more channels are sampled in a single beam run. This could be achieved by decreasing the sampling rate if the data codes are transferred to the PC where the ENOB calculation is done. In fact, if the sampling rate is halved, two channels can be tested. We expect that the error rate would double since the tested ADC has a full parallel structure. If the ENOB calculation is done on the test board by using a powerful FPGA or multi-FPGA architecture, more channels can be analyzed simultaneously during the run, thus collecting more events. With such an improvement, the DIS method is to

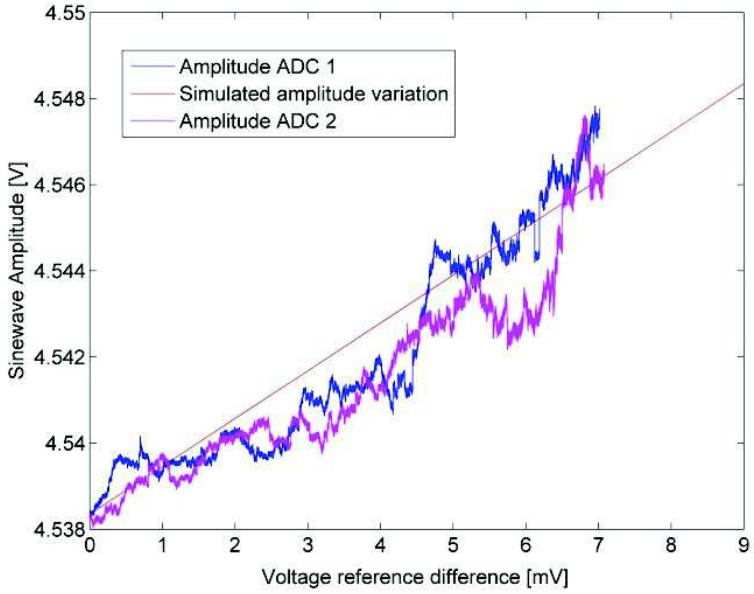

Figure 3-17: Variation of the sine wave amplitude as a function of the drift of the reference voltage for the ADC1 and ADC2. The test data are compared with the numerical simulation results.

be preferred to the SIS one for those applications with time-variant input signals. Moreover, the evaluation of the cross section with the DIS method is not affected by the voltage reference drift, and all the ADC codes are stressed.

3.3 RadMON system radiation test

In the Chapter 2 we discussed about the strategy adopted for the qualification of components; we stated that the qualification of the entire system exposed to the radiation environment is a necessary step which should be carried out before deploying it. We described the qualification tests carried out on the main components with which the RadMon is developed. To finalize the qualification process of the RadMon the entire system was tested in radiation environment. A test with the ^{60}Co source was planned in order to have a system level test and understand how the degradation of the main components affects the performances of the RadMon. The test has been carried out with a dose rate of 4 Gy/h. The target TID was set to 300 Gy. Two boards were entirely irradiated with the identical components mounted.

The results showed clearly that the weak point of the RadMon is the ADC. Indeed, at around 270 Gy the ADC for the monitoring of the sensors started to fail giving

wrong values to the FPGA which, instead, continuously communicates well with the bus. The failure of the sensors ADC is depicted in Figure 3-18 where the voltage thresholds of the two RadFets mounted on the RadMon are depicted. The increase of current and the variation of the internal voltage reference result in the increase of the value measured by the ADC. The two RadMons tested showed an identical behavior, pointing out that the ADC sets the limit for the RadMon TID life–time.

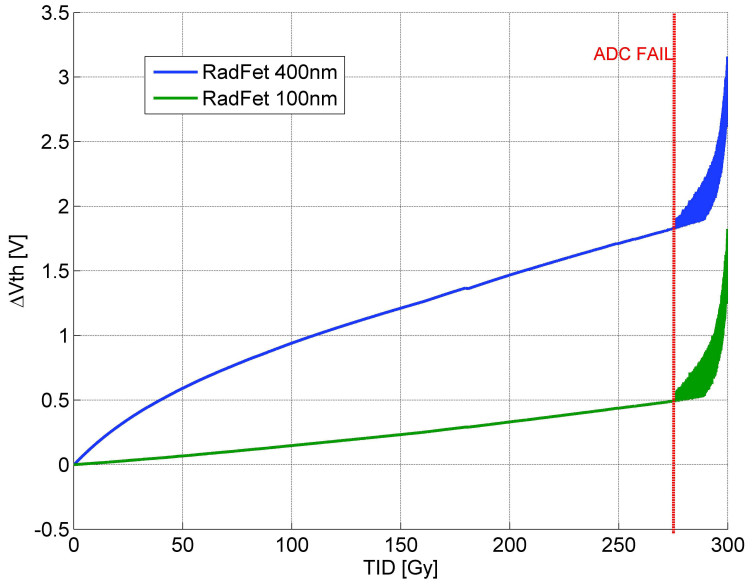

Figure 3-18: System Level Test of the RadMon V6. The red dotted line indicates when the ADC of the RadMon fails.

Another test with protons has been carried out on the entire RadMon system [42]. The results of the proton irradiation showed a higher TID life–time with respect to the ^{60}Co source test. This result is due to the fact that the proton beam size has a diameter of 9 cm and, most likely, when centering the RadMon in the beam the ADCs are on the border. Thus the effective dose received by the ADC is lower than the one measured because of the non–uniformity of the beam. Of particular interest in the protons test was also to verify the SEU susceptibility. The tests passed successfully without showing errors up to a fluence of 1.8×10^{12}.

3.4 Summary

In this Chapter the Radiation Monitor instrument was presented. Two different RadMon architectures which belong to two different versions of the monitor are presented.

The Chapter reports also the test conducted on the sensitive components of the version of the RadMon V6, from the simple voltage regulators to the FPGA and ADC.

The RadMon is an embedded system with multiple features. It is developed completely on COTS components due to the large amount of units that are installed in the LHC tunnel. The architecture of the RadMon V5, which was developed starting from 2005, was discussed in details. The main requirements of this device are a radiation tolerance up to 80 Gy and the possibility to use the WorldFIP bus present at CERN as a communication link. The most important feature is that it should be able to measure along the three "axes" of the radiation effects (SEE, TID and DD).

The RadMon V5 architecture is based on a communication IC (the WorldFip controller or MicroFip) which also acts as main processing unit. The entire system is built on discrete components. The main building blocks are: the main controller unit, the digital peripherals used for the readout of the SRAM memories, used as HEH fluence monitor, and the analog circuitry to read the RadFets and the PIN diodes. The analog signals are digitized with a 12 bit ADC that as we will see later in the Chapter 4, is one of the limiting factors for the sensors' resolution.

The issues encountered with this version of the radiation monitor are mainly due to the low TID life–time (80 Gy) which reduces the MTBM. The presence of manual switches on the RadMon presented a problem when a change of the configuration was necessary. These are some of the motivations that led to a development of a new RadMon version.

The new version of RadMon, referred as "V6", is based on a modular system, made by a power board, a mainboard and a sensor board. The modularity is a necessary requirement to improve the maintenance. The architecture of the RadMon V6 is based on a flash based COTS FPGA which can provide a flexible solution to many of the requirements of the RadMon instrument. Indeed, the FPGA takes now the place of the MicroFip module, mastering the communication on the fieldbus and it does much more. Its flexibility permits not to have anymore manual switches to change the RadMon parameters, avoiding a manual intervention every time something had to be changed. The ADC currently used in the RadMon V6 is a 16 bits ADC which permits to have a higher resolution with respect to the previous one and, thus, improves the resolution of the sensors. The readout circuit for the SRAM memory is not made by external components anymore and the entire algorithm to read the SRAMs is embedded in the FPGA.

The most important part of the design was the selection and the qualification of the components. Indeed for this new version of RadMon the TID life–time was the primary concern. All the components have been qualified following the policy

expressed in the Chapter 2 and the radiation tolerance has been analyzed. In this chapter some of the test carried on the most critical components have been discussed.

Three types of bipolar voltage regulators have been tested. Two of them had the same device reference but made by different companies. All of them showed good results during protons test, but when the 1-MeV neutrons test was carried out one of the two regulator failed before the expected fluence. For this reason the second one has been chosen as a substitute for the RadMon development. This case gives us a good feedback that applying our policy for radiation testing most of the possible failure modes for our environment are scoped.

The ADC was also tested with protons, neutrons and with ^{60}Co gamma. A completely new test methodology has been developed for the ADC testing. Indeed, the so called DIS method was developed in order to stress all the codes from the ADC and be insensitive to the variation of the internal voltage reference. The online test was carried with protons mainly to verify the SEU and SEL sensitivity. The test with ^{60}Co gamma were carried out to measure the TID–lifetime and the TID behaviour of the main parameters. The TID–lifetime found for the ADC is around 260 Gy, this value set the limit for the entire tolerance of the RadMon.

The FPGA has been tested by another group working at CERN and the results have been reported and commented. Furthermore, the FPGA was also tested with the final firmware in the full RadMon system test.

Infact, the RadMon was tested with a proton beam and with the ^{60}Co and no issues were found nor SEUs recorded. The degradation of the performances started to appear around 250 Gy, due to the ADC failure.

The enhancement in the radiation tolerance, and in particular, of the TID life–time, permits to increase the MBTM of a factor 3 with the respect to the previous RadMon version.

Chapter 4

RadFet Dosimeter

The first article regarding the use of a MOS device as a total ionizing dose sensor was written in the 1974 by Holmes-Siedel [52]. After few years, a space qualified radiation dosimeter based on the MOS structure was used for the European communication satellite (OTS) in the geostationary orbit [53]. Nowadays, the MOS dosimetry has a wide application field, ranging from the medical [54], security [55] to environmental radiation monitoring [56]. In the last decade, the community of high energy physics experiments started using the MOS dosimeter as preferred device for the Total Ionizing Dose measurements [57]. The main target of this chapter is to explain the fundamentals of the MOS dosimetry and analyze the characterization process and the significant results for the LHC environment. The basic principle of MOS dosimetry is that ionizing radiation transfers energy to silicon dioxide (SiO_2) and as a result, the measurement of this energy gives the information on the absorbed dose. RadFets are usually simple p-type MOSFETs with a thick gate oxide. The region of interest for dosimetry is below the gate region and is made of silicon dioxide (SiO_2). As already discussed in Chapter 2, the ionizing radiation passing through the oxide deposits energy and creates electron/hole pairs. During the first pico–seconds the radiation–induced electrons and holes can recombine; the fraction of this recombination process depends on some parameters such as the internal electric field and oxide thickness. Afterwards, the radiation–generated electrons are swept quickly towards the gate electrode because of their high mobility. The holes that escape the recombination move slowly with respect to the electrons and undergo a stochastic hopping transport towards the silicon substrate. When the holes reach the Si-SiO_2 interface some of them can be captured by trapping sites present since fabrication. These trapped holes represents the information on the absorbed dose. Indeed, they lead to a shift of the MOSFET threshold voltage V_{th} which can be easily measured.

RadFets work on a cumulative principle, because they integrate the information

on the absorbed dose over time. The ease of reading and the low power consumption make it suitable for the integration in a monitoring device such as the RadMon. In this chapter the physics behind the MOS dosimetry along with the technique used to read the dose information from the RadFets on the RadMon system are described. The results from ^{60}Co calibration are shown for the two types of RadFet analyzed in this work: the 100nm and 400nm thick oxides. The annealing behavior for each type has also been investigated because it produces a loss of the dose information. Later in the chapter we also studied the temperature coefficient variation with respect to the cumulated dose. Finally, we evaluate the issues encountered in the dose measurements with the RadFets in the LHC mixed field enviroment and the effectiveness of a gamma calibration.

4.1 MOS Dosimetry

The RadFet is a basically a p–type MOSFET with a thick oxide. The part of the P–MOS sensitive to ionizing radiation is the SiO_2 layer. Whe radiation passes trough the oxide the energy deposited generates electron/hole pairs. The energy necessary to create an electron/hole pair in the SiO_2 has been investigated in the past; in their investigation Benedetto and Boesh measured that the minimum energy is 17 $\pm$ 1 eV [58]. After creation, the e/h pairs can recombine in a very short time window. This extremely short time in which the recombination can take place is due to the mobility of the electrons and the holes. The mobility of electrons in SiO_2 is around 20 $cm^2V^{-1}sec$ at low field and at room temperature, while at a high field the electrons velocity saturates around 10^7 cm/s [59]. The holes mobility can vary from 1×10^{-6} up to 1×10^{-10} cm^2 V^{-1} sec [60]. Thus, being the holes relatively immobile with respect to the electrons, the initial recombination process can happen only in the first picoseconds.

Initial recombination depends on the incoming particle energy and LET. The two models that describe the process of recombination are called columnar and geminate [5]. The first is used when the incoming radiation deposits energy in dense columns, while the geminate model is used to describe the recombination when the charge pairs are far apart. When discussing initial recombination two parameters have to be known: the thermalization distance r and the average e/h pairs distance λ. The thermalization distance in the SiO_2 is around 5 to 10 nm while the λ is inversely proportional to the LET of the incoming particle. Knowing the stopping power of the incoming particle and the minimum energy to create a pair, it is possible to calculate the line density of electron/hole pairs. Once the pair density is found, the

distance λ is the inverse of it. For a low energy α particle the average pairs distance is much less than the thermalization distance thus, the assumption of a dense column of pairs is satisfied and the columnar model can be applied. Conversely, if the incoming particle has a small LET, the pairs distance will be a factor 5 of 10 greater than the thermalization distance. In this case, the geminate model can be applied. Despite this net categorization, there are intermediate situations in which the two models can overlap. A picture which summarizes the charge yield as function of the electric field for different types of particles is depicted in Figure 4-1 [5].

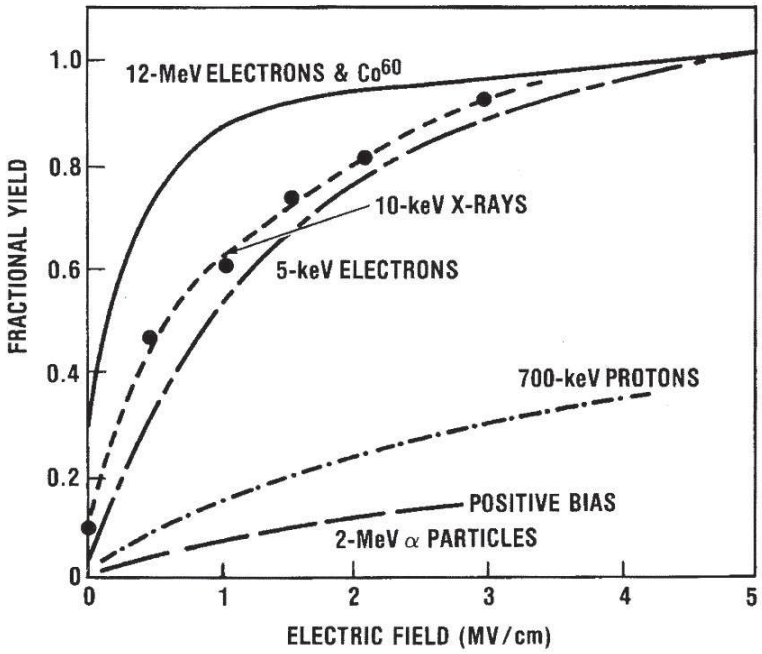

Figure 4-1: Charge yield as a function of applied field for several different types of incoming radiation [5].

It is interesting to look in details at what happens to the charge yield with protons, because as we will see in a successive paragraph, the protons can be used for the characterization of the RadFet as they contribute noticeably at the spectra of the LHC. Several experiments have been carried out by different authors on the charge yield for n and p type MOS devices [61–69], and the results have been summarized by Oldham in [5]. Figure 4-2 depicts the charge yield as a function of the incoming proton energy [5]. The geminate model can apply when the energy is higher than 150 MeV, while the columnar model can be used to model low energy protons (around 1 MeV). The intermediate energies between these extremes show that there is not a

net change in the behavior between the geminate and columnar model. The spread among the measurements is due to the fact that the experiments have been carried out at different electric fields, but this does not avoid to underline the charge yield trend as function of the incoming energy.

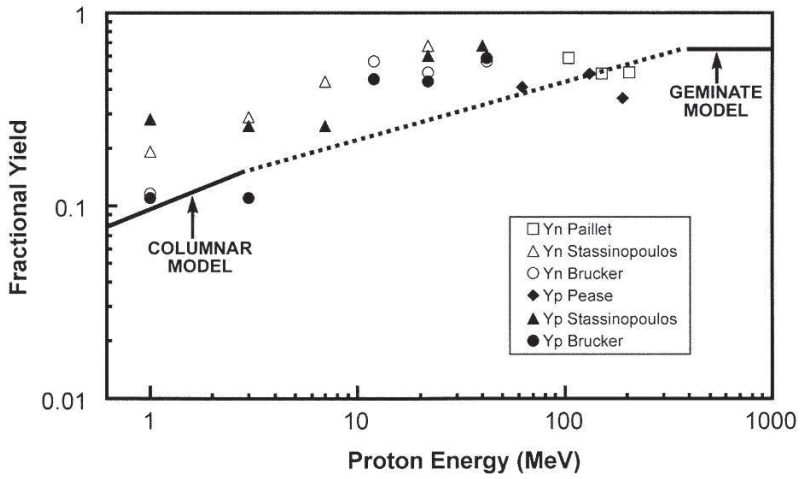

Figure 4-2: Charge yield as a function of the proton energy. n and p refer to n- and p-channel transistors, respectively [5].

Following the irradiation and after the first picoseconds of recombination the holes have the time to be transported through the oxide and be trapped in the SiO_2. The term "trap" is generally used to name a neutral defect in the oxide that can capture holes and retain them for a certain amount of time. The location of the (occupied) hole traps depends on the biasing condition of the MOS structure. Under a positive bias most of the charge is within a few nanometers ($\sim$5 nm) from the Si/SiO_2 interface while under negative bias most of the charges are trapped near the gate electrode [70].

Reactions between holes and hydrogen–containing defects or dopant complexes can also lead to the formation of a second type of ionization defect: the interface trap (N_{it}). Interface traps exist within the silicon band gap at the interface with the SiO_2. Because of their location at the interface, the charge of an interface trap can be changed easily by applying an external bias. Interface traps can be positive, neutral, or negative. Traps in the lower portion of the band gap are predominantly donors, i.e., if the Fermi level at the interface is below the trap energy level, the trap "donates" an electron to the silicon. In this case, the trap is positively charged. P-channel transistors are affected primarily by interface traps in the lower region of the band gap. Therefore, for a p-channel transistor, interface traps are predominantly

positive, causing negative threshold-voltage shifts. Interface–trap buildup occurs on much slower time frames than oxide-trap charge buildup. Unlike oxide-trap charge, interface-trap charge does not anneal at room temperature.

The $\Delta V_{ot,it}$ that results from the trapped holes and from the interface traps is given by

$$\Delta V_{ot,it} = \frac{\Delta Q_{ot,it}}{C_{ox}} = \frac{\Delta Q_{ot,it} \cdot t_{ox}}{\epsilon_{ox}} \tag{4.1}$$

Q_{it} can be written as

$$\Delta Q_{it} = \frac{q}{t_{ox}} \int_0^{t_{ox}} \rho(x) x \cdot dx \tag{4.2}$$

where $\rho(x)$ is the charge distribution of radiation–induced interface trap. Q_{ot} can be expressed as:

$$\Delta Q_{ot} = \frac{q}{t_{ox}} \int_0^{t_{ox}} n_{ht}(x) x \cdot dx \tag{4.3}$$

The term n_{ht} is the density of trapped holes that we can simplify assuming that the charges are located at a distance t_{ox} from the Si/SiO_2 interface and they are uniformly distributed [71]. The equation (4.1) can be rewritten as in equation (4.4).

$$\Delta V_{ot}(Fi, En) = \frac{q}{\epsilon_{ox}} \cdot g_0 \cdot f_y(Fi, En) \cdot f_t(Fi) \cdot t_{ox}^2 \cdot D \tag{4.4}$$

where g_0 is the initial charge generation factor, D is the dose and f_y is the initial recombination charge yield that depends on the electric field Fi and on the the energy En and type of the incoming particles. The term f_t weighs the fraction of holes that are trapped. The variation of voltage due to the hole trapping process and to the interface traps changes the threshold voltage of the MOS structure irradiated. Indeed, the variation of voltage threshold can be rewritten as:

$$\Delta V_{th} = \Delta V_{ot} + \Delta V_{it} \tag{4.5}$$

Looking at equation (4.4) and (4.5) we can identify the key parameters that the user needs to chose in order to increase the sensitivity, expressed as the variation of the voltage shift with respect to the dose received. The thickness of the oxide is the most important parameter, and a thicker oxide exhibits higher sensitivity. On the other hand increasing the thickness of the oxide usually means decreasing the electric field and this, in turn, means a change in the terms f_y and f_t.

4.1.1 Annealing of the Oxide Traps

The annealing of radiation–induced trapped holes in SiO_2 is a long–term process that is strongly dependent on the temperature and applied electric field. Annealing can proceed by either of two processes, tunneling or thermal excitation. The tunneling process has been widely studied in [72–74], while the thermal excitation in [75, 76]. At or near room temperature, tunneling is the dominant mechanis, whilst if the temperature is raised enough, then the thermal process will eventually dominate.

The tunneling process is illustrated in Figure 4-3. The tunneling probability is an exponential function of distance. For this reason, traps near the interface will be neutralized very quickly, but traps farther from the interface will be annealed later. We can imagine as there is an apparent tunneling front, where traps to the left of the vertical front in Figure 4-3 have been compensated or annhealed, while those to the right have not. It is possible to include also the thermal annealing process, with the trap energy level distribution shown in Figure 4-3. The result of the two processes is a logarithmic annealing curve.

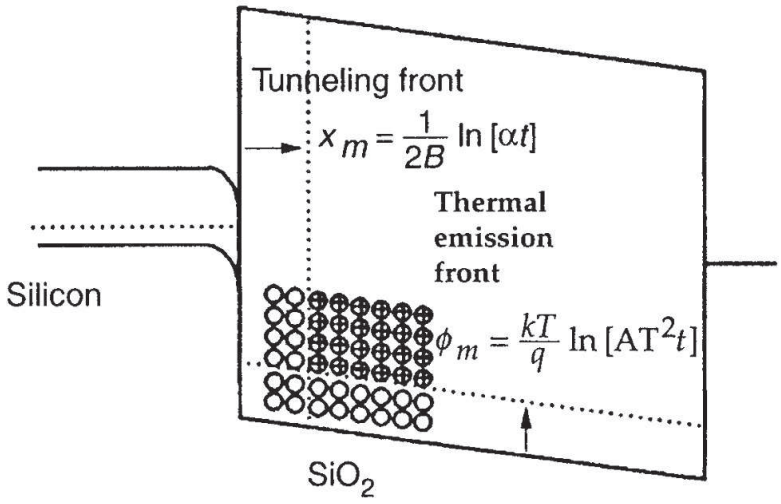

Figure 4-3: Annealing due to combined tunneling and thermal annealing [77].

4.1.2 RadFet readout

The Figure 4-4 shows the irradiation and the measurement circuits. During the irradiation, the gate pin can either be grounded as in Figure 4-4.a or forced to a potential

as in Figure 4-4.b. The Figure 4-4 shows the irradiation and the measurement circuits. During the irradiation, the gate pin can either be grounded as in Figure 4-4.a or forced to a potential as in Figure 4-4.b.

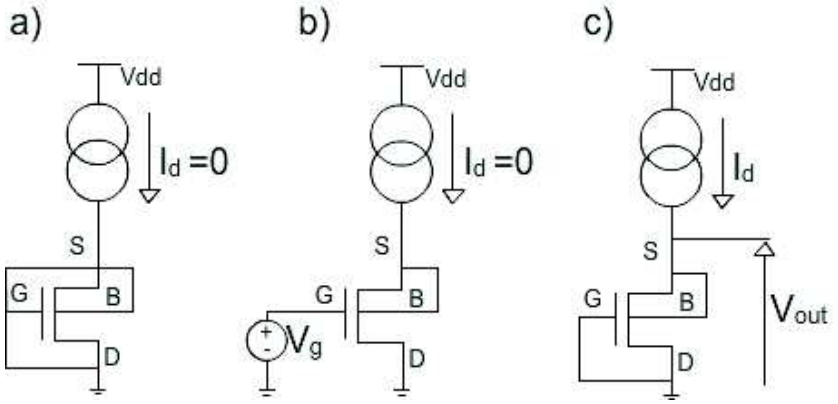

Figure 4-4: RadFet reading circuit a)Zero bias condition during irradiation b)Bias voltage Vg applied to the gate during irradiation c) Current pulse injection during the reading.

When a RadFet has to be read, a current pulse is injected from the source by means of a current generator (Figure 4-4.c). In order to operate in saturation mode, where the relation between the square root of the drain current and the gate voltage is linear and unaffected by gate–drain bias voltage, the gate is connected to its drain. This configuration is called "diode connection" and the equation that links the drain current (I_d) with the gate source potential (V_{sg}) is:

$$I_d = \frac{1}{2}\frac{W}{L}\mu_p C_{ox}\left(V_{sg} - |V_{tp}|\right)^2 \tag{4.6}$$

Where V_{tp} is the threshold voltage, W and L are the width and the length respectively of the MOS, μ_p is the holes mobility and C_{ox} is the oxide capacitance per unit area. The output potential V_{out} can be expressed as:

$$V_{out} = V_{sg} = |V_{tp}| + \sqrt{\frac{I_d}{\frac{1}{2}\frac{W}{L}\mu_p C_{ox}}} \tag{4.7}$$

As shown in the equation 4.7 the potential read on the source is linked to the threshold voltage, but there is also a part that depends on the reading current. Considering that the same current I_d is injected in for the reading and considering an irradiation phase between two successive readings, then the difference of the two measured V_{sg}

will be:

$$\Delta V_{sg} = V_{sg1} - V_{sg2} = |V_{tp1}| - |V_{tp2}| \tag{4.8}$$

Thus, the difference between two readings (V_{sg1} and V_{sg2}) is a direct measure of the shift of the RadFet voltage threshold. The change of the ΔV_{sg} at different dose levels is a direct representation of the shift in threshold voltage, allowing an easy read out of the dose level.

Equation 4.8 does not depend on the injected current; nevertheless great care should be taken in the choice of the readout current. Indeed, the V_{th} changes with the temperature [6]. Any change of the threshold voltage can be due to irradiation and temperature variations. To reduce the effect of the temperature on the RadFET threshold voltage, the readout current is set at the value where the variation of V_{th} is expected to be the minimum, i.e. where the Temperature Coefficient $Tc = \frac{dV}{dT}$ is zero. This point is called the ZTC point.

When the pulse of current is injected a voltage overshoot can happen. Moreover, a dependency of the RadFet voltage rise time with the dose has been observed in the past. Hence, to avoid these effects the measurement of the source potential is carried out after 95 ms from the pulse injection. This will assure that the output signal is correctly recorded by the ADC. The typical protocol followed to read the RadFet is depicted in Figure 4-5.

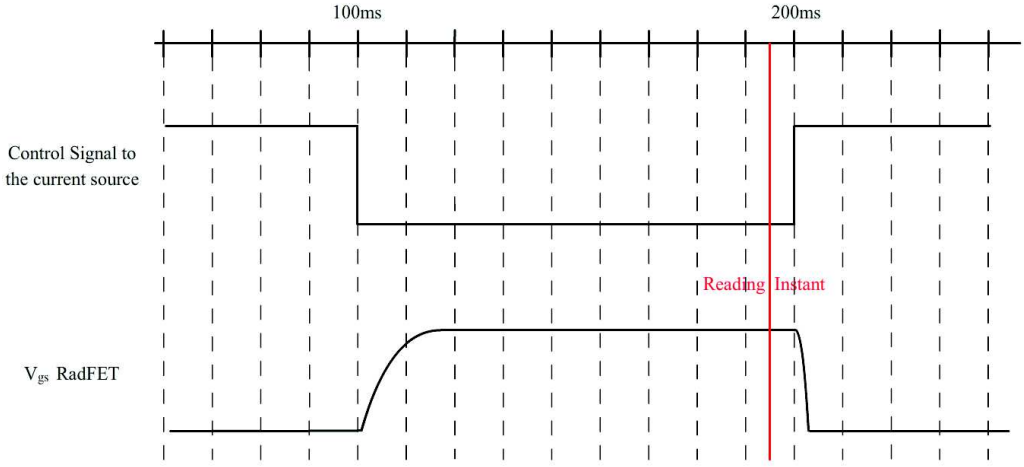

Figure 4-5: Typical protocol for the RadFet measurement.

As already mentioned the RadFet biasing condition is a way the end–user has to increase the sensitivity of the sensor. In unbiased mode the RadFet is left with the source, drain, body and gate connected to the same potential (usually ground). This

condition is used when the sensitivity can be sacrificed for a large dynamic range. The sensor can reach high doses without a huge increase of the V_{sg} which can saturate the readout electronics. As discussed before, being the charge yield (the term f_y in equation (4.4)) strongly dependent on the electric field in the oxide, at zero bias the only electric field present is the one derived from the work function potential [6]. Thus, being the electric field low, the sensitivity of the dosimeter is low too. In order to improve the sensitivity, an electric field can be applied during irradiation. This field improves the charge yield for the same dose levels.

4.2 RadFet Characterization

The calibration of the RadFets is an important step to follow in order to have reliable measurements. Usually when a new batch of sensors is bought a calibration is needed to asses the sensitivity and the sample–to–sample spread. The factors to take in consideration during the calibration planning are multiple, some of them are related to the different environments that the sensor will encounter during its work in the LHC, others, instead, are related to electrical conditions.

The reference calibration is performed with a ^{60}Co gamma irradiation. Depending on the RadFet type, different dose rates and different TID target are selected to characterize the sensors. A test with protons is also recommended since, as it will be shown, the incoming particle energy can have an impact on the sensitivity of the sensors. The electronics conditions concern the applied gate bias, the current injected for the reading and the read timing.

During several years we tried to scope the best solution for the RadMon and the main results are reported in the following paragraph. The tested RadFets come from one manufacturer NMRC. The NMRC RadFet chip contains two MOSFETs with a different aspect ratio for the gate area, one is $300 \times 50\mu m$ and the second is $690 \times 15\mu m$ [78]; in this work we tested only the $300 \times 50\mu m$. The NMRC RadFets are available with different oxide thicknesses, and the ones tested for the RadMon projects are a 100 nm unimplanted RadFet and a 400 nm implanted RadFet. The 400 nm is implanted with boron to reduce the pre–irradiation voltage threshold, which otherwise would have a high value due to the thick oxide growth. It has been shown that due to the creation of additional defects in the oxide caused by the implantation process, the sensitivity of the 400nm implanted RadFets is enhanced with the respect to the un–implanted one [79]. The NMRC RadFets are encapsulated in a Dual In Line (DIL-14) ceramic package with a kovar lid.

4.3 ^{60}Co calibration 100 nm

The ^{60}Co gamma irradiation source was used to calibrate the RadFet. The parameters to select in a gamma calibration are the dose rate and the final dose to reach. In Table 4.1 the irradiation conditions for the calibration runs are reported.

Table 4.1: RadFet irradiation conditions for several ^{60}Co runs

Run	Dose rate [Gy/h]	Dose [Gy]	Irradiation	Temp °C
1	1	0-100	Biased +5V	25
3	1	0-100	Biased-GND	40
4	1	0-100	Biased-GND	25
5	50	0-1000	Biased +5V	25
6	50	0-1000	Biased GND	25
10	50	0-10000	Biased-GND	40
11	50	0-10000	Biased +5V	40

We will compare first the two runs at 1 Gy/h (run 1 and 3). In run 1, the RadFets had a gate bias of +5 V while in run 3 the gates were biased to GND. From the Figure 4-6 the average responses of the three sensors are plotted with linear fits. The response of the RadFet 100 nm is linear up to 100 Gy regardless the biasing condition. The biasing at +5 V permits to increase the sensitivity of a factor 3 with respect to the GND condition.

Run 2 is carried out to verify a possible difference in the 100nm RadFet response if the temperature is set at 40 °C. As it is shown in Figure 4-7, the difference between the calibration curves at 25 °C and 40 °C is around 1%. This test was done to assure that the sensor calibration curve does not change with the absolute value of the temperautre which will be around 25 and 40 °C on the deported module and the main board of the RadMon respectively (See Chapter 3). The dose rate dependency has been also assessed for the 100 nm up to 100 Gy. The dose compared are 1 Gy/h and 50 Gy/h for both the biasing configurations (see Table 4.2). The dose rate effect brings a higher difference in the ground biasing condition; nevertheless the difference is less then 10% for both biases.

Table 4.2: Dose Rate dependency

Dose rate	Bias	Temperature	difference wrt 1 Gy/h%	TID [Gy]
1 - 50 Gy/h	+5V	25 C	-5.3	100
1 - 50 Gy/h	GND	25 C	-8.3	100

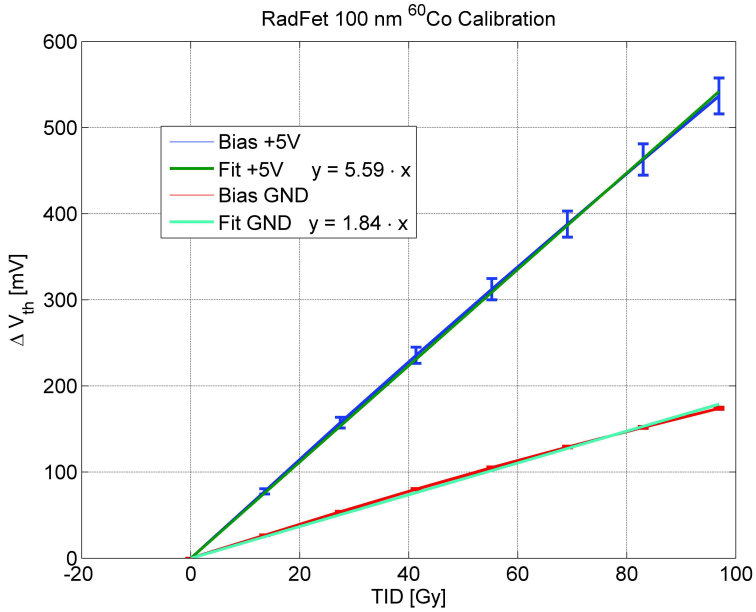

Figure 4-6: Average response of three RadFets for a ^{60}Co irradiation. Two biasing conditions have been tested: +5 V and GND. The response of both the configurations is linear up to 100 Gy. The error bars are the standard deviation calculated on the three samples.

Run 5 and 6 are carried out to obtain the calibration up to 1000 Gy. This is useful in zone where the dose rate is relatively high or if the same RadFet has to be used several times. The Figure 4-8 depicts the average of the response of two sensors for both bias configurations. The linearity is not satisfied anymore and a power law fit has to be used. The parameters a and b of equation 4.9 are reported in Figure 4-8 for the +5 V and GND bias conditions. In order to evaluate the goodness and the usability of the fits we reported the maximum error between the measurements and the fit in Table 4.3. The maximum error committed is around 7%.

$$\Delta V_{th} = a \cdot Dose^{b} \tag{4.9}$$

Table 4.3: Power fit maximum error. The error on the dose is expressed as an absolute value and as a percentage with the respect to the dose measured.

Bias	**Delta Vth [V]**	**Error [Gy]**	**Error [%]**
GND	0.5	-31	-6.6
+5V	2.9	-34	-6

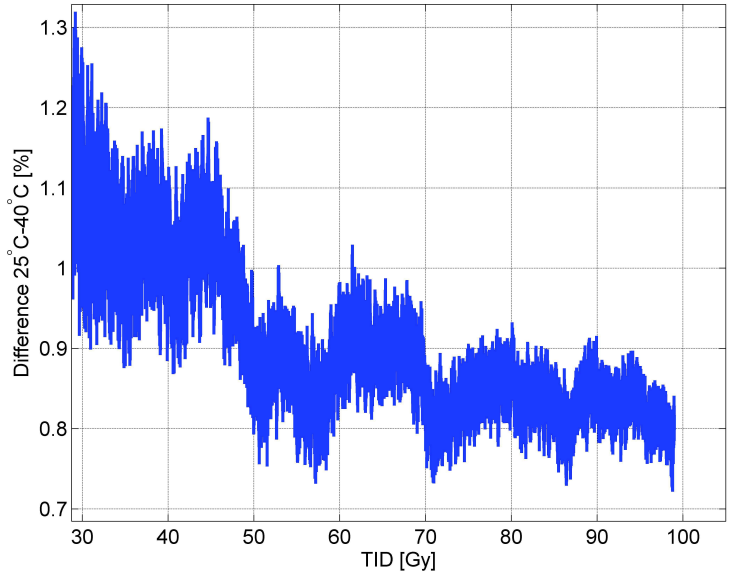

Figure 4-7: Percentage difference between the response of the RaFet irradiated at 25 °C and at 40 °C.

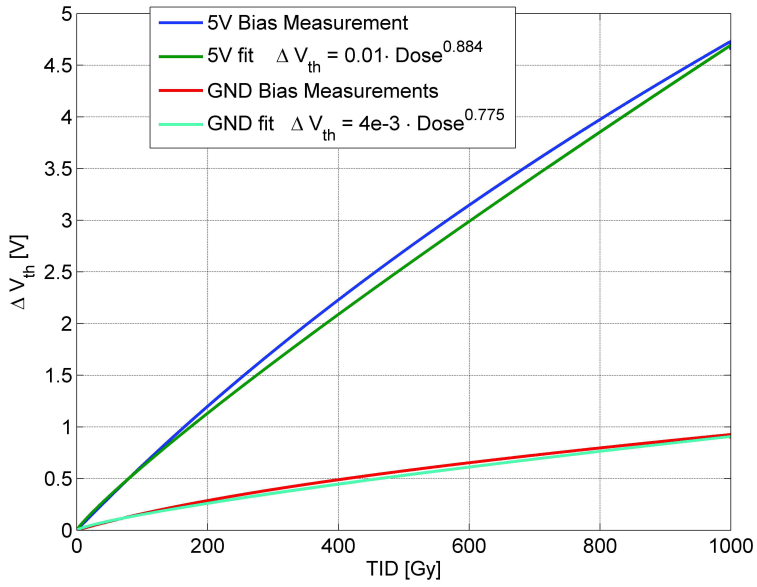

Figure 4-8: RadFet 100 nm average response up to 1 kGy. The two biasing conditions have been fitted with a power law.

In the RadMon operation the calibration curves are used as a look up table without any modification. The fits can be useful to compare the sensitivity of different types of RadFets. In the Table 4.4 the fits for the 100nm and their validity in terms of dose are reported.

Table 4.4: Summary of the fitting equations and their validity for the 100 nm.

	Bias	**Validity**	**Linear fit**	**Power fit**
100nm	GND	0-100 [Gy]	$y[mV] = 1.84D[Gy]$	
	5V	0-100 [Gy]	$y[mV] = 5.59D[Gy]$	
	GND	0-1000 [Gy]		$y[V] = 4e-3D[Gy]^{0.775}$
	5V	0-1000 [Gy]		$y[V] = 1e-2D[Gy]^{0.884}$

The RadFet 100nm biased GND has a sensitivity of 1.84 mV per Gy, while the sensitivity increases of around a factor 3 with a 5 V bias on the gate. As already mentioned in the previous chapter, the resolution of the RadMon in terms of TID is related to the electronics. Indeed, the measurement resolution changes if we use a 12 bit ADC, as in the RadMon V5, or a 16 bit ADC, as in the RadMon V6. The Table 4.5 reports the minimum appreciable dose variation that the two versions of RadMon can measure. The RadMon V5 with the 100nm RadFet in biased configuration is reported only for the sake of comparison since there is no possibility to bias the RadFet on the RadMon V5. The improvement in the resolution for the RadMon V6 is substantial; the resolution can go as low as 20 mGy with the bias configuration.

Table 4.5: Comparison of the minimum dose resolution achievable with a 100nm using the RadMon V5 and V6.

	RadMon V5	RadMon V6
ADC	12 bit	16 bit
ADC Resolution	2.4 mV	150 μV
100nm GND Resolution [Gy]	1.3	8.2×10^{-02}
100nm 5V Resolution [Gy]	0.4	2.7×10^{-02}

4.3.1 Annealing

The measurements of the annealing is another important task to perform because during the LHC operation the amount of time the beam is off is an important fraction of the total time. Indeed, in the 2012 the amount of time the LHC was operative was the 86% of the total time (considering the machine setup) [80].

The annealing has been measured 5 days after the end of the irradiation keeping the temperature constant.

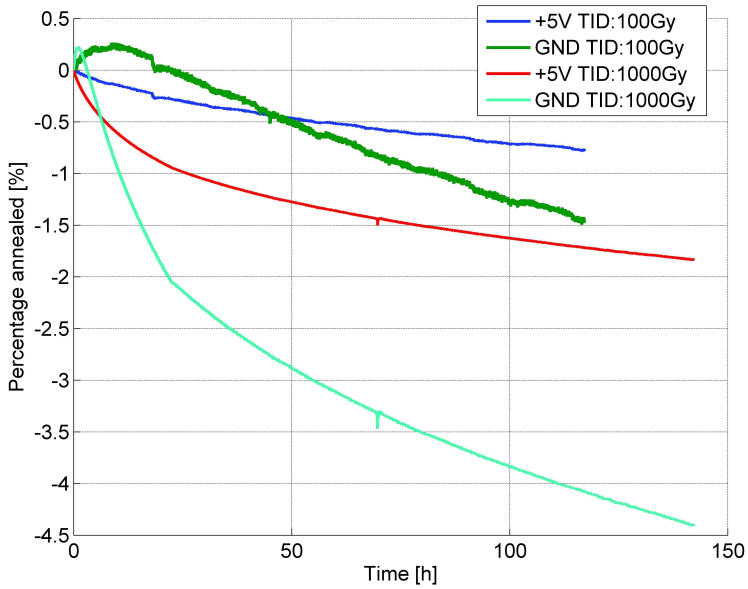

Figure 4-9: Annealing of the RadFet 100 nm. The final TID reached influences the annealing. The two biasing conditions have a different behavior.

In Table 4.6 the variation percentage is reported for each biasing and irradiation condition. The lower the value of the accumulated TID the lower is the amount of annealing. The annealing affects more the RadFets that are unbiased rather than the ones biased at 5V, this behavior was already reported by [81]. The annealing effect is a temperature–dependent process; thus in all the conditions in which the temperature is kept at 40 °C the fading is higher than the one at 25 °C.

Table 4.6: Annealing of the 100 nm 5 days after the test. The sensor are kept in the same electrical conditions of the irradiation.

Index	Bias	Final dose [Gy]	Temp [°C]	Fading [%]
1	+5V	100	25	0.78
2	GND	100	40	2.71
3	GND	100	25	1.48
4	+5V	1000	25	1.56
5	GND	1000	25	3.81
6	GND	10000	40	5.61
7	+5V	10000	40	2.38

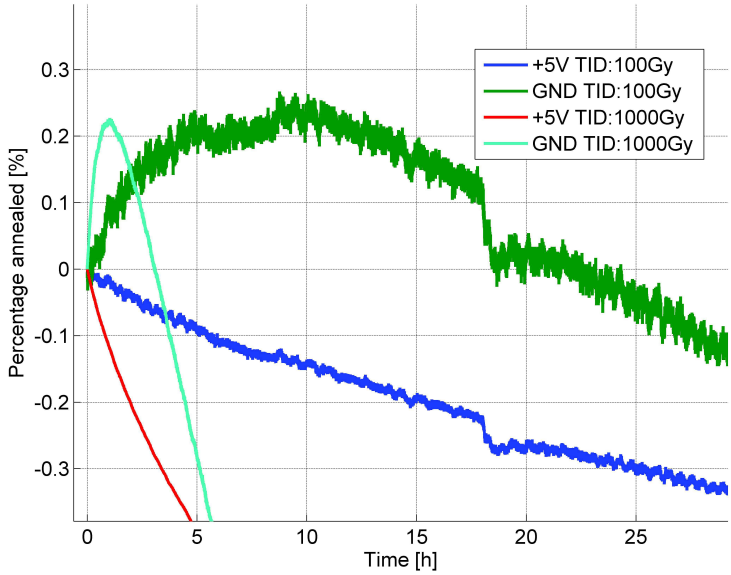

Figure 4-10: First 30 hours of annealing of the RadFet 100 nm. The GND biasing condition showed a build-up process whose duration lasts more if the TID reached is low.

The phenomena of reverse–annealing visibile in 4-10 can be attributed to the interface traps which have a delayed build up from few seconds to thousands of seconds after the irradiation. For a p-type MOS, the interface traps behave in the same way as the oxide traps leading to a negative shift of the voltage threshold. In Figure 4-10 the build up effect is clearly visible for the unbiased condition. The annealing build up last longer for the low TID (100 Gy) because the ratio of oxide traps with respect to the interface traps is comparable for a PMOS. Reaching higher TID, the ratio between oxide traps and interface traps increases so the interface build up is still present but the amount of oxide traps is larger; thus the anneal of those traps start to affect the annealing response earlier. The RadFets biased at +5 V do not show any build up effect because the annealing of the oxide traps, which are in a larger quantity with respect to the zero bias, is the dominant effect. The information on the dose lost during the annealing phase has to be taken into account during the operation. The 100 nm RadFets irradiated at 1000 Gy, can hold the information on the dose loosing only less then 6% over 150 hours at room temperature and being biased at GND, which is the worst condition of annealing.

4.4 ^{60}Co calibration 400 nm

Several radiation calibration campaigns have also been carried out on the 400 nm. Only in one irradiation campaign the 400 nm was used in biased mode as done with the 100 nm. The calibration curve of the 400 nm is depicted in Figure 4-11. The tests have been carried out up to 2300 Gy and 6900 Gy for the RadFet biased at +5 V and for GND respectively. A power law fit (see equation (4.9)) has been used on both configurations. The error is less than 10 % for the unbiased condition while it is the 22% for the biased +5 V condition(see Table 4.7).

In the Figure 4-11, the limits of the acquisition chain of the RadMon are depicted. Two limits are shown because, as explained in the Chapter 3, the RadMon V6 has different gains in order to reach higher dynamic ranges. Because of the large sensitivity of the 400 nm biased at +5 V it is necessary to have a a gain of 0.1 in order to not enlarge the signal dynamic. With the gain of 0.1 the response of the 400 nm biased reaches the maximum allowed voltage on the RadMon at an accumulated TID of around 230 Gy.

In order to compare the response of the RadFet 400nm with the two configurations, it is useful to zoom in the linear region of the 400nm response. The RadFets biased at GND have a response which is almost linear in the range 0–20 Gy; for this reason we will compare the two configurations in this range. In the Figure 4-12 the two fits show that the 400nm biased +5 V is around a factor 4.5 more sensitive. In the Table 4.8 the fitting equations are summarized along with the range of dose where they are valid.

Table 4.7: Power fit maximum error for the 400 nm. The error on the dose is expressed as an absolute value and as a percentage with the respect of the dose measured.

Bias	Delta Vth [V]	Error [Gy]	Error [%]
GND	13	-400	9.8
+5V	2.9	-65	22

Table 4.8: Summary of the fitting equations and their validity for the 400 nm.

	Bias	Validity	Linear fit	Power fit
400nm	GND	0-20	$y[mV] = 38.2D[Gy]$	
	5V	0-20	$y[mV] = 128.2D[Gy]$	
	GND	0-6500 Gy		$y[V] = 0.3D[Gy]^{0.43}$
	5V	0-2000 Gy		$y[V] = 0.83D[Gy]^{0.58}$

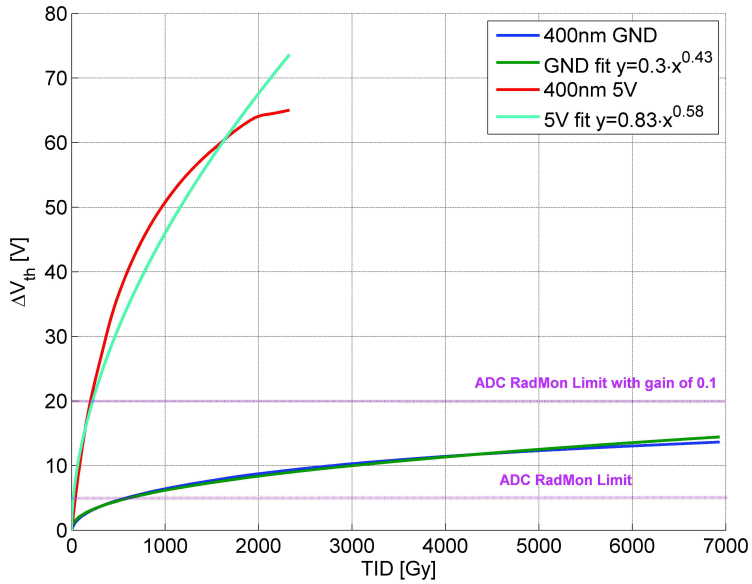

Figure 4-11: Calibration of the 400 nm unbiased and biased +5V. The power law fit is depicted for both the configurations.

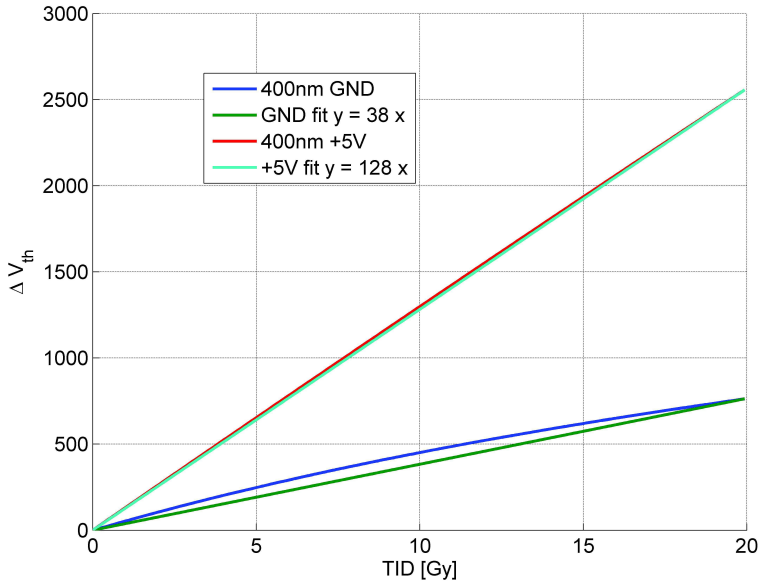

Figure 4-12: Zoom in the linear region of the 400nm response. The linear fits for the two configurations are also depicted.

Being the RadFet 400nm more sensitive with respect to the 100nm, it assures a higher resolution . It is possible to measure with dose steps of about 60 mGy and 10 mGy with the RadMon V5 and RadMon V6 respectively (see Table 4.9).

Table 4.9: Comparison of the minimum dose resolution achievable with a 400nm using the RadMon V5 and V6.

	RadMon V5	RadMon V6
ADC	12 bit	16 bit
ADC Resolution	2.4 mV	150 uV
400nm GND Resolution [Gy]	0.063	3.93×10^{-03}
400nm 5V Resolution [Gy]	0.019	1.17×10^{-03}

4.4.1 Annealing

The annealing of the RadFets 400 nm is expected to be higher than the 100 nm. Indeed the study of the annealing on two RadFets 400 nm biased ground has been carried out. The RadFets were exposed to a ^{60}Co source up to 50 and 600 Gy respectively. The measurements of the annealing were carried out on the next $\sim$ 12 hours after the irradiation. Figure 4-13 depicts the percentage of ΔV_{th} annealed in that time window. The RadFets 400 nm do not show a build–up effect such as the one of the 100 nm, but they show a larger annealing. Indeed, for the 12 hours of annealing period the RadFet irradiated up to 50 Gy lost the 1.5% of the V_{th} while the one irradiated up to 600 Gy lost the 2%. It is very likely that the 400 nm irradiated up to 600 Gy would continue to decrease the V_{th} with the time, while the one irradiated up to 50 Gy would stop decreasing. Indeed, we performed measurements of the V_{th} on RadFet of a previous campaign 6 months after the irradiation. The V_{th} drop was around the 15% for a 400 nm irradiated up to 600 Gy.

4.4.2 Temperature coefficient measurements

As stated previously in this Chapter and in Chapter 3 the RadFets are devices sensitive to the temperature variation. With the reading circuit described in paragraph 4.1.2 it is possible to minimize the impact of the temperature by using the so called ZTC point. Unfortunately, even choosing the right current to feed the RadFet, it has been demonstrated that the temperature coefficient depends on the dose that the sensor accumulated [82]. Moreover, as also mentioned in Chapter 3, the RadFet readout circuit on the RadMon V6 does not include any temperature compensation

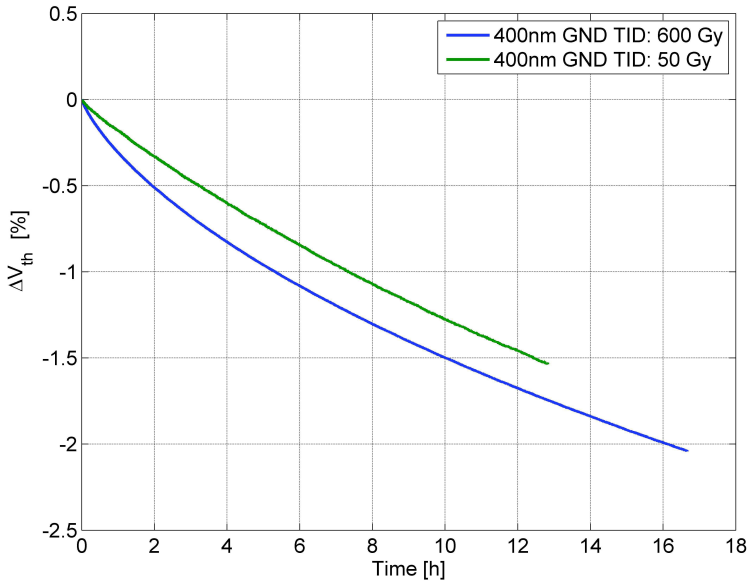

Figure 4-13: Annealing of the 400 nm unbiased for two TID accumulated 50 and 600 Gy.

which instead was carried out by analog components on the RadMon V5. Thus, the duty of the compensation is done at software level. For this reason it is important to know the value of the temperature coefficient and correct the measured value of potential with respect to the temperature variation.

Several measurements have been carried out on RadFets irradiated with ^{60}Co at different doses. Immediately after the irradiation, it was not possible to appreciate any variation of the threshold voltage due to temperature variation because the annealing phenomenon was prevailing. Hence, some measurements have been carried out after 6 months from irradiation to ensure that the annealing process was not the dominant process.

The temperature variation is controlled continuously to obtain the same variation for all sensors. The temperature sensor (PT100) is located inside the deported module. The temperature sweeps from 27 °C to 38 °C. At least 3 measurement cycles for each sensor have been done. In Figure 4-14 an example of the threshold voltage variation as a function of the temperature is shown.

It can be noticed that the voltage variations are the same for the 3 temperature cycles. The hysteresis is due to the dynamic of the temperature changes and to the slow response of the sensor. In the Table 4.10 the information on temperature coefficients are arranged considering the thickness of the oxide. A thicker oxide leads

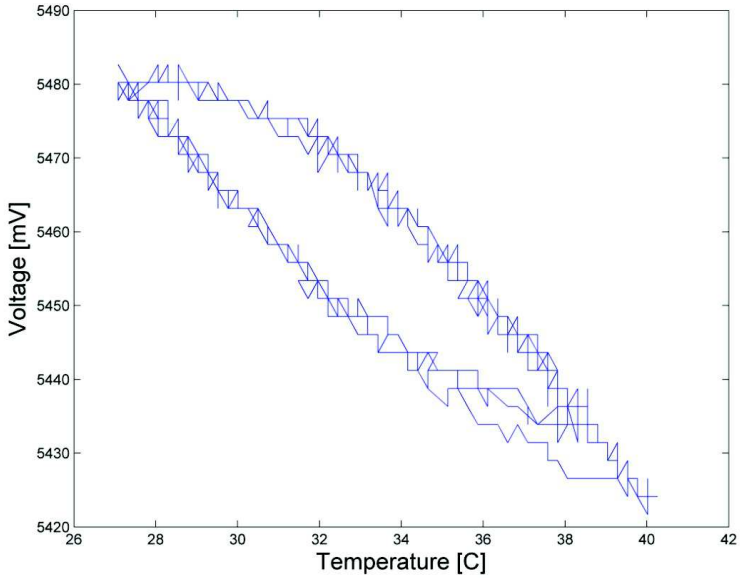

Figure 4-14: Variation of the voltage threshold as a function of the temperature. Three cycles are depicted.

to higher temperature coefficient at 0 Gy [6]. The temperature coefficient increases quite linearly with the dose for both RadFets.

In Figures 4-15 and 4-16 linear fits are proposed to match the data which can be easily implemented at both firmware or software levels to correct the V_{th} if the temperature changes.

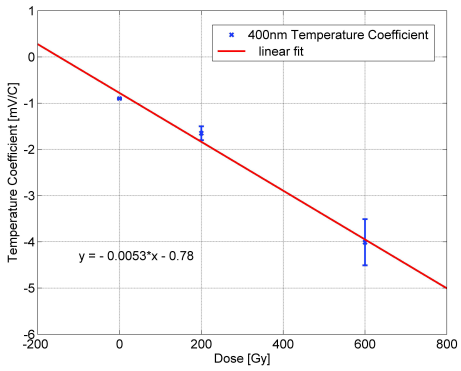

Figure 4-15: 400 nm Radfet Temperature Coefficient (TC) as a function of the cumulated dose.

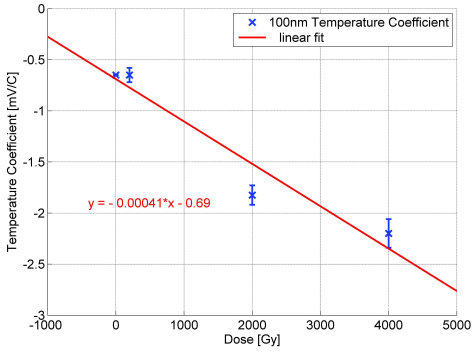

Figure 4-16: 100 nm Radfet Temperature Coefficient (TC) as a function of the cumulated dose.

Table 4.10: Temperature coefficient of 400nm and 100nm Radfets irradiated at different doses. The standard deviationn of the three measurements is also reported.

Mean TC	Std TC	Dose	Oxide Thickness
mV/C	mV/C	[Gy]	
-0.65	0	0	100nm
-0.65	0.07	200	
-1.825	0.095	2000	
-2.2	0.14	4000	
-0.9	0	0	400nm
-1.65	0.15	200	
-4.00833	0.5	600	

4.5 Use of the RadFet in a mixed field environment

An investigation was carried out on the use of RadFETs to monitor TID in a complex mixed particle field such as the one encountered in LHC. The validity of using a ^{60}Co source calibration has been studied. Several measurements have been performed at two CERN experimental test areas capable of providing particle spectra representative of the LHC environment [83]. From those measurements it has been shown that higher dose values are measured with thinner RadFETs. This has been shown using RadFETs with different oxide thicknesses measured with identical beam conditions.

The tests have been carried out one RadFets with three different oxide thickness: 100 nm, 400 nm and 1000 nm.

The tests in the mixed radiation field have been carried out at two facilities one is H4IRRAD and CNRAD. Different locations have been analyzed in the last test facility and they are reported in Table 4.11. “CNRAD45”, “CNRAD455” and “CNRAD463” correspond to three test locations inside the experimental test area. The “PMI” location is the closest to the CNGS target, consequently it is the location with the highest flux and dose rate. In order to understand this effect, simulations have been performed to evaluate the field and the particles contribution to the deposited dose inside RadFETs and it resulted that the charged hadrons like e.g. protons highly contribute to the deposited dose. Thus, irradiation tests have also been performed at the PSI to further investigate their response curve in a proton beam.

Figure 4-17 shows the dose measurements carried out with 100 nm and 400 nm thick oxide RadFETs during irradiation at the CNRAD451 test location. The dose measured by the RadFETs are illustrated versus proton on target (P.O.T). The protons coming from the SPS accelerator impinge on the CNGS target which generates the mixed particle field present in the area. The RadFets is then used to monitor the

Table 4.11: Averaged and pulsed dose rate for the CNRAD AND H4IRRAD experimental test areas.

Position	Averaged Dose Rate [Gy/h]	Pulsed Dose Rate (Gy/h/extraction)
PMI	10	$\sim 3 \times 10^6$
CNRAD451	0.9	$\sim 250 \times 10^3$
CNRAD455	0.054	$\sim 15.4 \times 10^3$
CNRAD463	0.08	$\sim 22 \times 10^3$
H4IRRAD	0.3	1.3

TID due to the cumulative number of proton hitting the target over a certain period of time, using the ^{60}Co calibration curves. As it can be observed in this figure, the dose retrieved by the 400 nm is lower than the one given by the 100 nm. The same effect can be seen in the other test locations (see Table 4.12), apart from the PMI location where the dose rate is a factor around 10 times higher than at the CNRAD451.

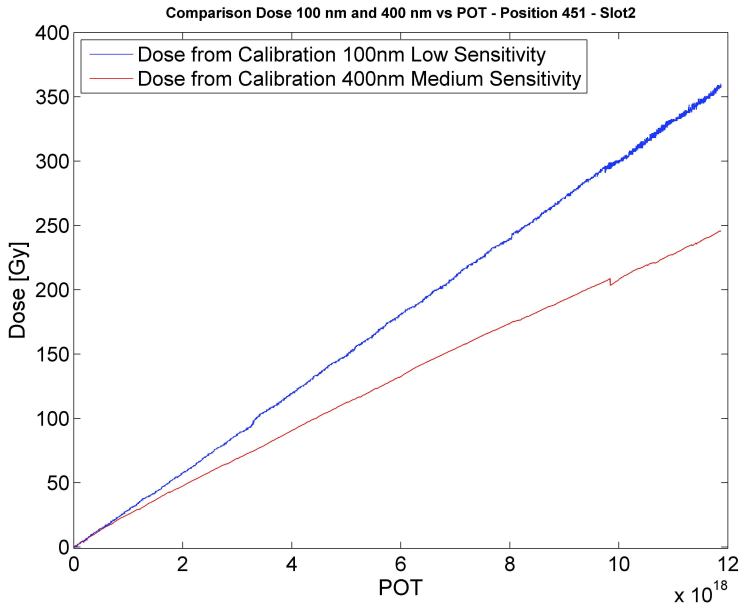

Figure 4-17: Dose measurements using 100 nm and 400 nm thick oxide RadFETs at the CNRAD451 test location. The x–axis represents the number of protons impinging on the CNGS target (POT).

This analysis triggered the study of the radiation spectra in the test locations where the RadFets are mounted. FLUKA Monte Carlo simulations have been per-

Table 4.12: Difference between the dose measured by the 100 nm and 400 nm /1000nm RadFets with respect to the 100nm.

Position	Dose 100 nm (Gy)	Dose 400 nm or "1000nm" (Gy)	Difference (%)
CNRAD 451	350	341	-31
CNRAD 455	10	7	-30
PMI	600	593	-1.1
H4IRRAD	15	11.8	-21

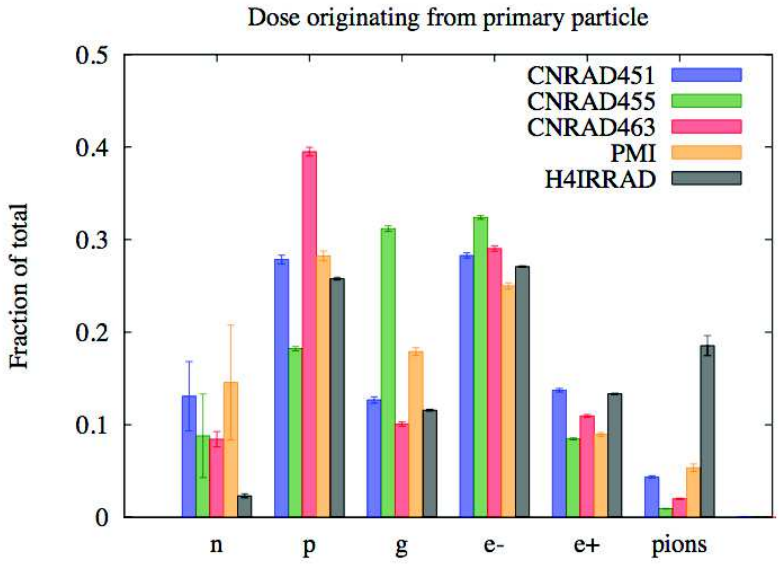

Figure 4-18: Fraction of the energy deposited in the RadFET oxide for each particle type present in the particle spectra for the four CNRAD and the H4IRRAD locations. [83].

formed in order to investigate how each particle type of the mixed radiation field contributes to the deposited dose in the RadFET. Of all particles incident to the lid side of the RadFET, the simulation results in Figure 4-18 shows that protons and electrons each are responsible for 20-40% of the deposited dose. In sum this corresponds to more than a half of the total deposited dose in contrast to incident photons which only contribute to 15-20 % in total. Only at the "CNRAD455" test location photons are contributing up to around 30% of the total deposited dose. The remaining fractions are due to neutrons, positrons and pions interacting with the RadFET material. The higher fraction of photons for "CNRAD455" is due to its more shielded location with respect to the other ones. As a result the relative attenuation of the

hadrons is higher, which induces a higher contribution of the photons to the deposited dose.

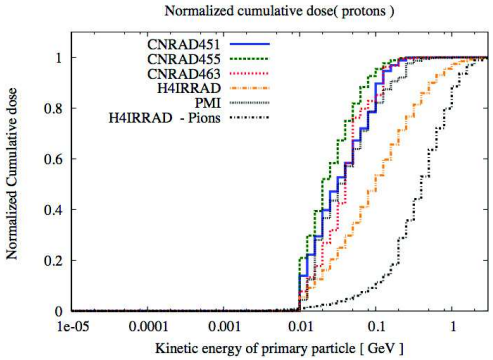

Figure 4-19: Cumulative dose as a fraction of the total deposited dose in each location for incoming protons. In an additional curve is added for the case of deposited dose by incoming pions in the H4IRRAD location. Results are presented versus the kinetic energy bins of the incoming protons/pions [83].

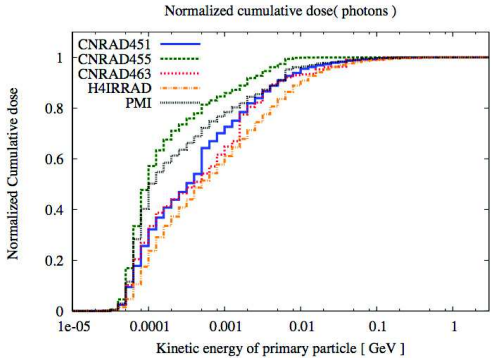

Figure 4-20: Cumulative dose as a fraction of the total deposited dose in each location for incoming photons. Results are presented versus the kinetic energy bins of the incoming photons [83].

Simulations of the cumulated dose for protons and photons have been performed and the normalized curves are presented in Figure 4-19 and 4-20. Those figures show the link between the dose deposition and the energy of protons. As it is illustrated in Figure 4-21, at CNRAD 80 % and 50 % of the deposited dose by protons for each location is due to protons with energy lower than 100 MeV and 35 MeV respectively. Even if the energy range of photons which contribute to the dose deposition is larger than the one of protons, they contribute less. The conclusion is that the dose deposited inside the RadFETs is mainly due to protons with energies lower than 100 MeV.

To understand the energy dependency of the RadFet response, a test campaign with a proton beam has been carried out. The energy range used for this test has been chosen in order to understand the variation of the RadFET responses over a wide range going from 30 MeV up to 230 MeV. Figure 4-21 shows the ratios of RadFET radiation responses over dose given by the PIF facility plotted versus the different proton beam energies for each RadFET considerered in this study. Each point represents the ratio calculated at a final dose of either 50 Gy or 100 Gy, except for the 1000 nm radfet where the maximum dose reached is about 20 Gy. The 400 nm

and 1000 nm curves start to significantly bend towards lower ratios at energies lower than 100 MeV. This was observed in [68] where it has been shown that protons in the energy range below 200 MeV can influence the radiation response of transistor p–type MOSFET. In fact, protons in this energy range can lead to recombination effect inside the oxide that can then reduce the effective charge buildup at the Si-SiO_2 interface. This induces a decrease of the RadFET radiation response. Moreover, Figure 4-21 reveals that the oxide thickness plays a significant role on the oxide trapped charge. Indeed, as the thickness increases, the RadFET response is reduced.

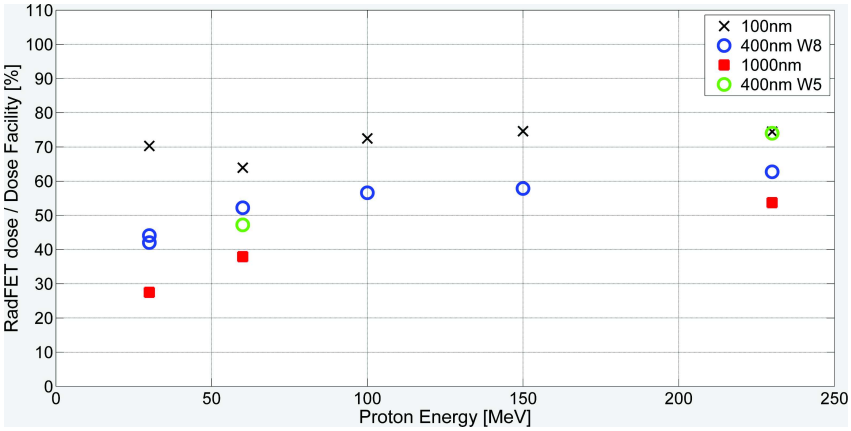

Figure 4-21: RadFET radiation responses over dose provided by the PSI facility versus incident proton energies for the 3 types of RadFETs [83].

4.6 Summary

In this chapter we analyzed and studied in detail a sensor able to measure the Total Ionizing Dose (TID): the RadFet. The RadFet is a p–type MOSFET, adapted for TID measurement. The sensor sensitivities are linked to the gate oxide thickness, indeed, the thicker the oxide the more sensitive is the RadFet. For this reason, we use RadFets with two oxide thickness 100nm and 400nm. The advantage of having two devices with different sensitivity is that we can have a higher TID range with a thinner device, and higher resolution with a thicker one.

In this Chapter we analyzed the physics of the MOS dosimetry to better understand the working principle and the operational features. The ionizing radiation releases energy in the SiO_2 layer of the RadFet, this energy produces a certain amount of electron-hole pairs. After the first picosecond, the electrons are swept away in the direction of the metal gate, while the holes undergo to a hopping transport in the

dielectric. Finally, the holes are trapped close to the Si/SiO_2 interface. This process is enhanced if a bias is applied to the gate of the RadFet: increasing the electric field leads to a bigger number of holes that escape the recombination and that can be trapped. This mechanism, along with the formation of radiation–induced interface traps, leads to a shift of the RadFet threshold voltage. The variation of the voltage threshold with the dose is not linear, thus a calibration is needed.

The readout techniques used in the RadMon exploits the relation between the drain current and the gate source potential in order to measure the variation of the threshold voltage at different doses. In the paragraph 4.1.2 the importance of several electrical parameters, such as the amount of current injected or the reading protocol, has been underlined.

The RadFet calibration has been carried out with a ^{60}Co source on both the RadFet type 100nm and 400nm. Two gate biasing conditions have been tested, one foresees the gate potential to ground (GND) while the second was biased at +5 Volts. Despite the non–linearity of the RadFet, we are still able to approximate the curve with a linear fit for low doses. We can assume the linearity for the 100nm from 0 to 100 Gy while for the 400nm we made a linear fit up to 20 Gy. The linear fit permits to compare the sensitivities for each configuration. In the Table 4.13 the sensitivities are reported for the 100nm and 400nm and the two different biasing conditions. As expected, the 100nm is less sensitive than the 400nm of about a factor 20 considering the same conditions, in good agreement with the expected ratio of 16 (t^2_{ox400}/t^2_{ox100}).

Table 4.13: Summary of the RadFet sensitivity for the 100nm and 400nm.

	Range of Validity	Sensitivity
	[Gy]	[mV/Gy]
100nm GND	0-100	1.84
100nm +5V	0-100	5.59
400nm GND	0-20	38.2
400nm +5V	0-20	128.2

The entire calibration curves for both the RadFet have been fitted to a power fit equation. The fits matches quite well the two curves. Despite that, the calibration curves are always used as look–up table not introducing any error in the conversion between voltage threshold and dose. The effect of the temperature on the calibration has been studied and no significant difference has been noticed.

The tests on the 100nm have been carried out also at different dose rates (1 Gy/h and 50 Gy/h) but the difference is less than 10 %.

The annealing behavior has also been studied in order to understand how much

information is lost if the sensors are not irradiated. As expected, the 400nm annealing is stronger than that of the 100nm; after just 12 hours the annealed charges are around 2% and after 6 months at room temperature they lost around 15 % of the dose information. In the annealing process of the 100nm it is clear that biasing the RadFet at +5 V lead to a lower annealing compared to the GND bias. Moreover, during the annealing period, the effect of the interface traps build up can be noticed for the GND configuration.

The Chapter underlines also the big improvements made on the dose resolution that can be achieved. While the RadMon V5 was able to measure with a resolution of 0.06 Gy with the 400nm, the RadMon V6 improves the resolution decrease of a around a factor 15 by means of a 16 bit ADC and a factor 50 if one considers also the possibility to use the biasing. In Table 4.14 the minimum values of measurable dose for the RadMon V5 and V6 are reported.

Table 4.14: Summary of the resolution in terms of dose achievable with the RadMon V5 and V6.

	RadMon V5	RadMon V6
ADC	12 bit	16 bit
ADC Resolution	2.4 mV	150 uV
100nm GND Resolution [Gy]	1.304348	8.15×10^{-2}
100nm 5V Resolution [Gy]	N.A	2.68×10^{-2}
	RadMon V5	RadMon V6
ADC	12 bit	16 bit
ADC Resolution	2.4 mV	150 uV
400nm GND Resolution [Gy]	0.063	3.93×10^{-3}
400nm 5V Resolution [Gy]	N.A	1.17×10^{-3}

The new hardware developed for the RadMon foresees no temperature compensation external components, as it was for the RadMon V5. This triggered the study of the temperature coefficent for the voltage threshold as a function of the dose. Indeed, we found that increasing the coefficient of temperature increases linearly with the dose. The increase is naturally dependent on the oxide thickness; a stronger temperature compensation is needed for a thicker RadFet.

In the last paragraph of the chapter, we analyzed the difficulties concerned with the dose measurement with RadFet in a mixed field environment such as the LHC. In particular we demonstrated that there is a difference between the dose measured with the 100nm and the 400nm when they were placed in two mixed irradiation facilities at CERN. The difference has been explained by studying the radiation spectra at

the two facilities and noticing that the particles that contribute the most to the final dose are the protons with an energy below 100 MeV. From the theory we know that different protons energies lead to different charge yield in the oxide, thus a difference in the voltage threshold. We studied the response of the RadFet to the incoming proton energy by means of a monoenergetic proton beam. We noticed that the response at 230 MeV is similar to the one obtained with ^{60}Co while lowering the energy the difference starts to be significant. Moreover this difference increases with increasing the thickness of the oxide. This last experiment leads us to think about the effectiveness of a ^{60}Co calibration in our environment and, the suitability of the use of a RadFet sensor in the RadMon. Nevertheless, looking at the results of the proton tests we found that the energy response of the 100nm does not depend on the energy of the incoming particle as much as the 400nm. This leads to the awareness that the 100nm RadFets give more reliable results in terms of dose in an LHC like environment and that if the 400nm has to be used, attention should be paid at the spectra of the incoming particle.

Chapter 5

SRAM memories as HEH Fluence sensor

The key concept in using a SRAM memory as sensor is to consider the fluence of high energy hadrons as the source of its single event upsets. To measure the fluence with an SRAM we count the number of bits in upset and, knowing the cross section, retrieve the number of particles that hit the device. Thus, the cross section of the SRAM, defined as the ratio of the total count of SEUs to the total fluence and the memory size in bit, has to be characterized. The cross section depends on the memory technology, the supply voltage, the type of impinging particles and their energy. Moreover, those factors are not independent among them. The reduction of the supply voltage typically reduces the critical charges that must be overcome to have a SEU [84]. With the technology scaling the critic charge is decreasing, but the number of memory cells per device is increasing. Thus, the Single Event Rate (SER) per device increases, while the cross bit section remains pretty stable (Figure 5-1), as reported by Baumann in [85], [86].

Charged particles such as protons must have few MeV to overcome the Coulomb barrier to be able to penetrate an atomic nucleus. Conversely, neutrons are not slowed down and all their kinetic energy can be transferred to the penetrated atomic nuclei. Therefore, SEE induced by neutrons and protons with the same particle kinetic energy are expected to become similar for energies above 50 MeV [84]. The cell memory upset can be also caused at lower energies and peaks in the range of thermal neutrons (around 25 meV) if the SRAM contains ^{10}B [87]. Boron is commonly used in the microelectronics industries as dopant or in the past in the borophosphosilicate glass (BPSG). When a ^{10}B nucleus captures a neutron, a reaction, $^{10}\mathrm{B}(\mathrm{n},\alpha)^{7}Li$, occurs and the energy, deposited by the reaction products, can induce an SEU. Because of the wide radiation spectrum composition of the LHC environment, all these effects on

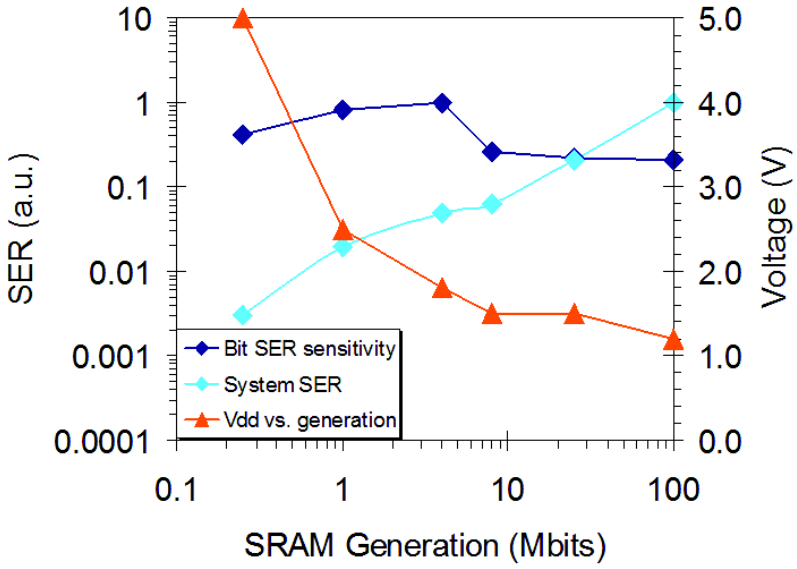

Figure 5-1: Trend of SER as function of the memory size. Each point is a different technology [85].

the SEE rate have to be assessed during the calibration phase.

Due to the high number of RadMon that have to be installed in the LHC complex, the choice of the SRAM is fixed to a commercial component for its availability and affordable price. Several parameters influence the choice of the right SRAM; the most important are:

1. The memory has to be Latch–up free.

2. The effect due to the TID has to be low in the range of the RadMon working life–time.

3. The achievable resolution per each memory should be lower than 1×10^8 pp/cm^2

These are the minimum conditions to consider an SRAM as a good candidate for the use as HEH monitor on the RadMon. The Latch–up free condition can be verified with a heavy ion test or with proton test. If the heavy ions test is available, the memory is considered Latch–up free in our environment if the Latch–up threshold value is above the LET of 20 MeV/cm^2/mg. If the memory has never been tested with heavy ions, a proton test at 230 MeV can be used to verify the Latch–up sensitivity being aware of cumulating a fluence considered representative of the effective working flu-

ence and of the environment. The test with protons to assess the Latch–up sensitivity can be used also to verify the cross section dependency with the accumulated TID.

The Toshiba memories TC554001AF-70L were chosen as HEH sensors for the older version (V5) of the RadMon [2]. The Toshiba SRAM is a 4 Mbit memory (512 Kbit x 8 bit) built with a 400 nm process, which can be powered from 5 V to 3 V. This memory was chosen because of its large fast neutron cross section and for its high thermal neutron cross section [88]. In this work the Toshiba memories has been re–calibrated because another lot of memories was bought. For the new version of the RadMon (V6) the Cypress memory CY62157EV30 was chosen. The Cypress is an 8 Mbit SRAM (512 Kbit x 16 bit) built with a 90 nm process, which can be operate from 3.3 V to 2.5 V of power supply. The main target of this memory is the mobile market because it is a part of the low power memories of Cypress which profits of the MoBl®technology [89]. In this work its suitability as HEH monitor is investigated according to the above defined criteria. The results of the Toshiba memories are recalled. Finally the use of the Toshiba and Cypress in the new version of the RadMon is discussed.

5.1 Memory Test Strategy

The complex LHC radiation environment requires an appropriate test strategy to qualify the cross section of the SRAM memory. The qualification process starts with a proton test at 230 MeV which aim at assessing the memory sensitivity and its robustness against latch–up. The preliminary tests aim at the assessment of the latch-up robustness and the measurements of the lot–to–lot variation and the inside the lot variation. Both the measurements are necessary because, being the memories a COTS, the same component identification can potentially comes from alternative fabrication lines and thus, behave in a different way under irradiation.

The dependency of the cross section on the cumulated TID is another important parameter to take in consideration when the sensors have to be used in a high dose rate location [90]. Once a good candidate is found, the cross section is measured at different energies ranging from 30 MeV to highest energy available in the facility. In this work the Toshiba were tested up to 230 MeV while the Cypress up to 480 MeV. The used test facilities are the Proton Irradiation Facility (PIF) of the Paul Scherrer Institute (PSI) (30-230 MeV) and the TRIUMF Laboratory in Vancouver (230-480 MeV).

The second step is the evaluation of the thermal neutron cross-section. As a third step and in order to study the cross section at energies below 30 MeV, a neutron

beam has to be used. As already said, at energies below 20 MeV the range of protons in silicon becomes less than the plastic package thickness leading to a significant drop in the cross section. Conversely, a neutron does not slow down through direct ionization and its kinetic energy can be expendend in the fragmentation of a nuclei and, therefore, potentially induce an SEU. For this reason, we measured the cross section with a monoenergetic beam of: 5, 8 and 15 MeV at the Physikalisch-Technische Bundesanstalt (PTB) facility in Braunschweig Germany.

As will be explained in the section 5.4.2 knowing the response of the memories as a function of the energy reduces the uncertainty on the HEH fluence estimation for the installation areas where the radiation field spectra are available.

5.2 Test Setup and procedure

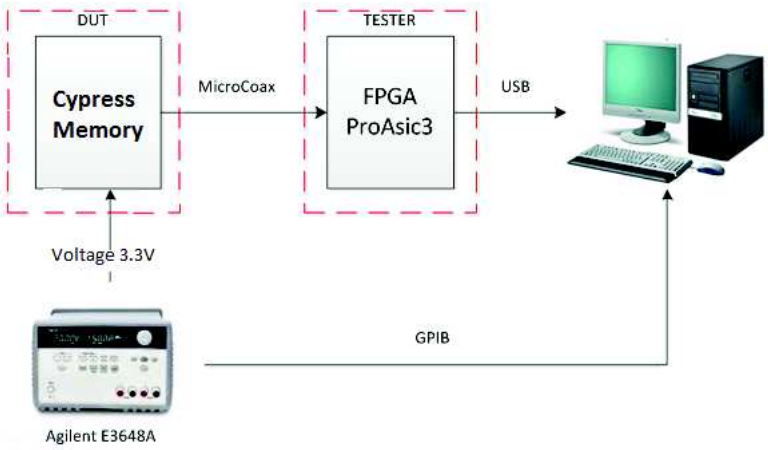

Figure 5-2: Test setup for the memory test.

The measurements were carried out by using the setup in Figure 5-2. Eight memories are mounted on a test board (Figure 5-3) connected to an FPGA board (tester board) by means of a MicroCoax cable.

Even if the tester board was not directly exposed to the beam, we chose a rad–tolerant FPGA. The chosen FPGA is an Microsemi ProAsic3E which has been extensively tested by the manufacturer [41], by the NanoFip [36,38] development team and for the RadMon development (see Chapter 3). The power supply of the test board is fed by an Agilent E3648A dual power supply. The tester board is read by a PC, located in the control room of the facility, via a USB connection. Three test protocols are used to measure the cross section. One method is referred as “static” and presents

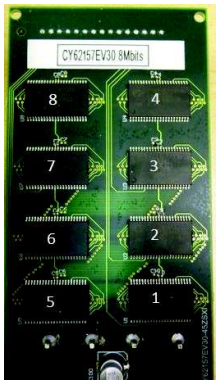

Figure 5-3: Carrier board for eight chips.

the following steps, also depicted in Figure 5-4.a:

1. Init Memory: the memory is initialized to a given bit pattern (all 0, all 1, or other); if more memories (chips) are under test, they are initialized sequentially.
2. Beam on DUT: the DUT is irradiated without being read. Then the beam is stopped.
3. Read + Data transfer: for each error, the address (32 bit) and the data (16 bit) are transmitted.
4. Processing: the data are processed to individuate the SEU and MBU.

The second test method is referred as quasi–static, here also referred as "RadMon Type" because the tester is programmed to use the same reading and writing procedure used by the RadMon. The "RadMon type" method is a quasi–continuous reading method, hence the memory is read when the beam is impinging on the memory (Figure 5-4.b):

1. Init Memory: the memory is initialized to a given bit pattern (all 0, all 1, or other); if more memories (chips) are under test, they are initialized sequentially.
2. Beam on DUT: the DUT is irradiated.
3. Read: the DUT is read to count the total number of errors starting from address 0x0000. In this phase, the error is detected on a single 16 bit line.
4. Processing: the read value is processed by the FPGA to individuate the errors on the single bit and discriminate for MBU (Multiple Bit Upset) on the same 16-bit line. The address of the SEU is not stored.

5. Write: the single line is rewritten with the initialization pattern.

6. Check: one reading of the same address is done to verify if the written pattern is correctly held in the memory.

7. Write-Check: the same operations as before (5–6) are repeated. If the two write-check operations fail the Stuck bit counter (SB) is incremented.

8. Move to the following line and repeat the steps 3–7.

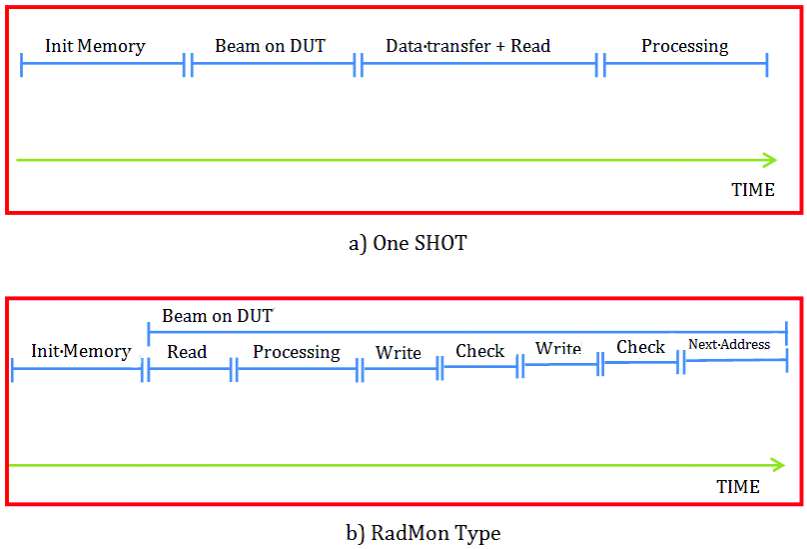

Figure 5-4: SRAM read methods: a) Static – One Shot b) RadMon Type.

A third test method is used and referred as "Continous Mode". This test method is based on the same working principle of the "One Shot" method but the beam is not stopped before reading the memory and the entire cycle showed in Figure 5-4.a is performed continuously during the irradiation. The procedure is:

1. Init Memory: the memory is initialized to a given bit pattern (all 0, all 1, or other); if more memories (chips) are under test, they are initialized sequentially.

2. Beam on DUT: the DUT is irradiated.

3. Read + Data transfer : a read is done and the FPGA is in charge of reading the SEU, MBU, and SB for each memory word. Two variants exist for the Data transfer "No-Dump" and "Dump"'.

4. Init Memory: the memory is initialized to the given bit pattern.

5. The process is restarted from the step (3).

Two variants of this test method exist, one is called "No Dump" and the other one "Dump". The two variants differ each other because the first just reports the number of SEUs, MBUs and Stuck bits, while the "Dump" mode transfers the addresses and words on which a SEU or MBU happens. The variants differs each other only in the "Processing" step depicted in Figure 5-4.a . Since, the transfer of the addresses and words is performed during the irradiation and no operations can be done in the meantime, the time between the read and the next initialization is called dead–time because any SEU happening in this phase is not counted.

Even if this type of reading method was not used for the calibration, because it introduces an uncertainty due to the dead–time, it is here analyzed since some early tests have been carried with this method on the Cypress memory. Here we want to analyze the impact of the dead time on the cross section evaluation. For each 16 bit line in fault state, i.e. the check with the expected pattern fails, the address (32 bit) and the data (16 bit) are transferred to the PC over a serial port at a speed of 57 kbps or 114 kbps (baudrate). The time window needed to transfer the data can be estimated by knowing the expected cross section of the memory and the flux of the beam during the test. In this analysis, we assume that the cross section is dominated by SEU, i.e., one error for each bit line. This is the worst case for the calculation of the time duration to transfer the data. The cross section per bit σ_{bit}, of the Cypress is about $1.8 \times 10^{-13} cm^2$ as will be discussed in the following paragraphs. The cross section of the chip (8 Mbit) σ, is $1.5 \times 10^{-6} cm^2$. Therefore, one can expect an SEU at each 6.6×10^5 protons on the DUT. Knowing the flux ϕ, the memory size, and the number of chip on the board, n, the total number of errors per second per board, N, is:

$$N = n \cdot \sigma_{bit} \cdot size \cdot \phi \tag{5.1}$$

For each error, the address and the data line are to be transferred. Therefore, the total amount of bits to be transferred per second is

$$N_{bits} = (32 + 16) \cdot N \tag{5.2}$$

The total time to transfer the data depends on t_{beam} and is given by:

$$t_{transfer} = \frac{N_{bits}}{baudrate} \times (t_{beam}) \tag{5.3}$$

where t_{beam} is the time the DUT is collecting SEU and $baudrate$ is the number of bit per second transmitted. According to the above sequence, the SEUs, which occur

during the time interval of transferring data and while reading a single memory chip, are not counted. This time period is indicated as t_{blind}. This interval depends on the baudrate of the transferring process and on the beam flux which fixes the SEU rate (given the cross section of the chip). Therefore, for an irradiation on continuous reading mode, t_{blind} has to be low enough to be neglected with respect to the time interval during which the DUT is irradiated and the SEU are counted, which consists of the t_{beam} plus the time to read the other $n-1$ memories; this time is indicated as $t_{beam-eff}$. One can consider the ratio r_{dump} defined as equation (5.4) and study its value as a function of the t_{beam} and ϕ.

$$r_{dump} = \frac{t_{blind}}{t_{beam-eff}} = \frac{t_{transfer} + t_{read}}{t_{beam} + (t_{read} \cdot (n-1))} \tag{5.4}$$

In this evaluation we will consider the worst case with 4 chips, n=4. The reading time (t_{read}) for a single memory is 78 ms. The Figure 5-5 shows the factor to apply for different beam time and different fluxes to correctly evaluate the effective fluence which has to be considered for the cross section calculation.

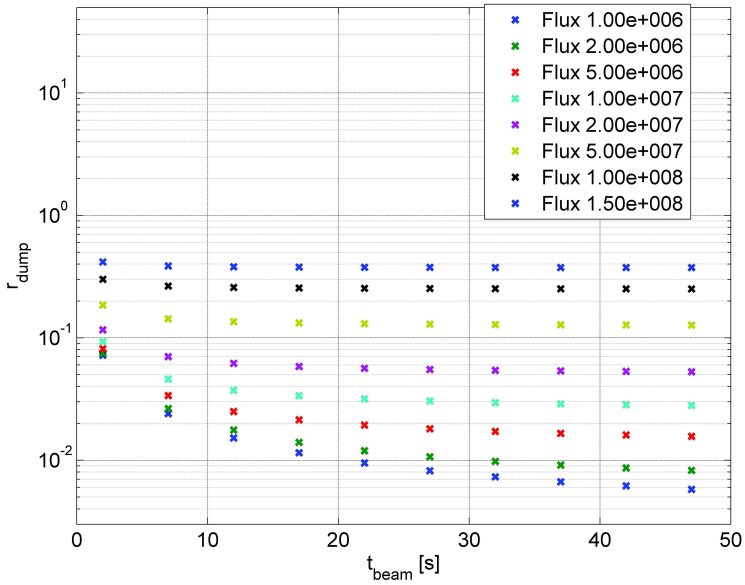

Figure 5-5: Ratio r_{dump} for the "Continous Mode" with the dump of the memory.

The same analysis can be done for the variant "No Dump". The transfer time in this case is very small because it consists of transferring 96 bit of the counters for SEU and MBUs and Stuck bit. Thus the transfer time is:

$$t_{transfer} = \frac{96bit}{baudrate} \tag{5.5}$$

Therefore the equation for the ratio r_{nodump} is:

$$r_{nodump} = \frac{t_{blind}}{t_{beam}} = \frac{t_{ransf} + t_{read}}{t_{beam}} \tag{5.6}$$

The Figure 5-6 shows that the ratio r_{nodump} is below 3% for a t_{beam} higher than 5 s.

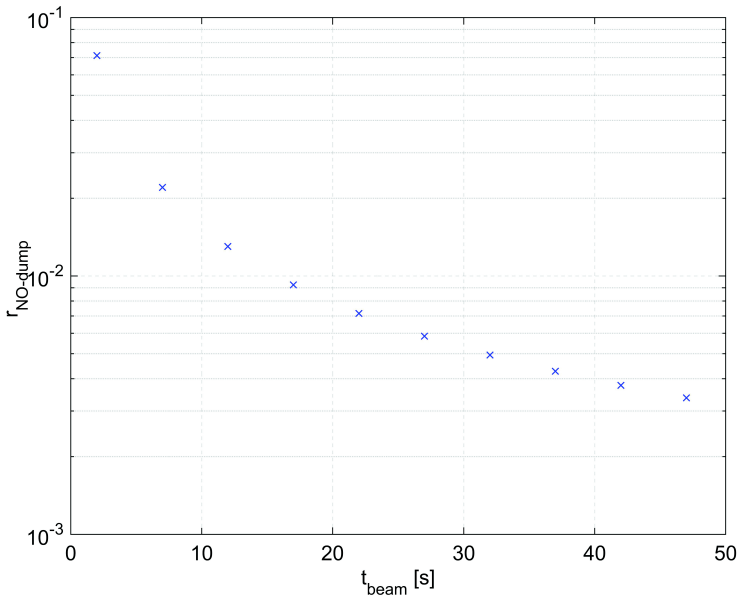

Figure 5-6: Ratio r_{nodump} of the blind time for the "Continous Mode" without the dump of the memory.

5.3 Experimental Results

The test results with the protons, the thermal neutrons and finally the tests with the neutrons at intermediate energies are reported and discussed. Then, the burst events of the Cypress memory are investigated and a mitigation technique is proposed. In this paragraph, the results of the Toshiba memories are reported and discussed too.

5.3.1 Cypress cross section for protons, thermal neutrons and neutrons at intermediate energies

Several test campaigns have been carried out in the past years to calibrate the Cypress memory. One of the first test campaign was in 2011 with a proton beam at PSI; the tests were performed to verify that the SRAM was latch–up free and to evaluate the cross section of that memories. To be noticed that the date lot code (1031) of those memories differs from the one tested afterward (1037 and 1125). Moreover, the tests were carried out on 4 memories at the same time using a 5 cm collimator

In Table 5.1 the Run number and the cross sections found are reported. To be noticed that all the tests have been carried out with the "Continuous Mode" with the "Dump" variant, then the results are adjusted for the effective beam time considering the equation (5.4). The tests were carried out in order to have more than 200 counts for each readings, reaching so a total number of SEUs per run bigger than 7000. This is done with the purpose of reducing the counting statistical error below 2%. The statistic error on N_{counts} is calculated as:

$$\sigma_{stat\_count} = \frac{1}{\sqrt{N_{counts}}} \tag{5.7}$$

Table 5.1: Results of the test carried out on the first lot of Cypress on the 2011.

RUN	Read mode	T beam [s]	Fluence $[p/cm^2]$	Energy [MeV]	Flux $[p/cm^2/s]$	**DUT 1** [cm^2/bit]	**DUT 2** [cm^2/bit]	**DUT 3** [cm^2/bit]	**DUT 4** [cm^2/bit]
12	Dump	40	5×10^9	230	3.4×10^6	1.82×10^{-13}	1.77×10^{-13}	1.62×10^{-13}	2.56×10^{-13}
15	Dump	40	5×10^9	230	3.4×10^6	1.91×10^{-13}	1.74×10^{-13}	1.34×10^{-13}	2.33×10^{-13}
24	Dump	40	1×10^{10}	230	8.6×10^6	1.46×10^{-13}	1.86×10^{-13}	1.33×10^{-13}	2.5×10^{-13}

These were preliminary tests carried out to verify the order of magnitude of the cross section. The mean cross section from the measurements is 1.85×10^{-13} with a standard deviation at 1σ of 4.1×10^{-14}, thus a 23% of spread among the considered samples. The MBUs cross section was evaluated and the contribution to the total cross section was less than 5%. These tests were performed at PSI with a collimator of 5 cm which was able to irradiate up to 4 memory at the same time. This is not the best option for the calibration for two reasons, a) the uniformity of the beam flux degrades moving away from the center, and b) great care should be paid in the centering of the 4 memories. In the successive tests, we tried to avoid this setup and characterize one memory at time with a collimator of 2 cm which gives the best homogeneity on the DUT.

Nonetheless we have reported those data because the good results led us to buy two lots of memories, one with the code 1125 (lot A) and the second with the 1037

(lot B). Twelve devices of each lot have been measured in the same conditions with a 230 MeV beam at a flux of $1.6 \times 10^8 pp/cm^2$.

Each device has been measured three times at 230 MeV to assess the repeatability of the cross-section measurements. In the Figure 5-7 the cross section of the DUTs of the two lots is reported with the repeatability error bar at 1–σ. The repeatability of the cross section measurements, evaluated using three shots on the single chip, is $1.57 \times 10^{-14} cm^2/bit$ and $2.63 \times 10^{-14} cm^2/bit$ for the lot A and B, respectively, which is equivalent to 10% of the average of the cross sections.

The mean of the cross sections of lot A is $1.87 \times 10^{-13} cm^2/bit$ with a 1–σ standard deviation of $4 \times 10^{-14} cm^2/bit$. For the lot B the mean is $3.31 \times 10^{-13} cm^2/bit$ with a 1–σ standard deviation of $7 \times 10^{-14} cm^2/bit$. Those values have been calculated considering all the measurements of each chip. For both the lots, the 1–σ standard deviation is 20%, thus the sample to sample variation dominated the uncertainty source terms. The results showed that there is a significant difference between the cross section of the two lots. Therefore the memories from the two lots have not to be mixed and, on each RadMon the memories have to be tracked from the origin.

One bit flip on a single memory corresponds to $6.37 \times 10^5 \pm 1.47 \times 10^5 pp/cm^2$ for the lot A ($3.6 \times 10^5 \pm 7.56 \times 10^4 pp/cm^2$ for the lot B). The RadMon V6, as already stated in the Chapter 3, can mount up to four Cypress memories. Measuring with four memories is a big advantage because the sensitivity increases by a factor 4 and the relative uncertainty is reduced by a factor 2. This can be easily verified by considering the equation of the uncertainty propagation (equation 5.8) and the expected mean of the population taking into account 4 memories (equation 5.9). The relative standard deviation is reported in the equation (5.10).

$$\sigma_{x4} = \sqrt{(\sigma_{x1})^2 + (\sigma_{x1})^2 + (\sigma_{x1})^2 + (\sigma_{x1})^2} = 2 \cdot \sigma_{x1} \tag{5.8}$$

$$\mu_{x4} = \mu_{x1} + \mu_{x1} + \mu_{x1} + \mu_{x1} = 4 \cdot \mu_{x1} \tag{5.9}$$

$$relstd = \frac{2 \cdot \sigma_{x1}}{4 \cdot \mu_{x1}} \cdot 100 = \frac{\sigma_{x1}}{2 \cdot \mu_{x1}} \cdot 100 \tag{5.10}$$

Using four memories at the same time and summing their SEU counts, the effective cross section per bit of the system is $7.5 \times 10^{-13} \pm 8 \times 10^{-14} cm^2$ for the lot A, and $1.32 \times 10^{-12} \pm 1.4 \times 10^{-13} cm^2$ for the lot B. The relative uncertainty using four memory is 10% considering 1–σ standard deviation. The resolution on the fluence considering four memories becomes $1.59 \times 10^5 \pm 1.7 \times 10^4 pp/cm^2$ using the lot A and $2.25 \times 10^4 pm 2.39 \times 10^3 pp/cm^2$. Finally, the uncertainty on the measurements

considering a confidence level of 95% for four memories is 20% for both the lots.

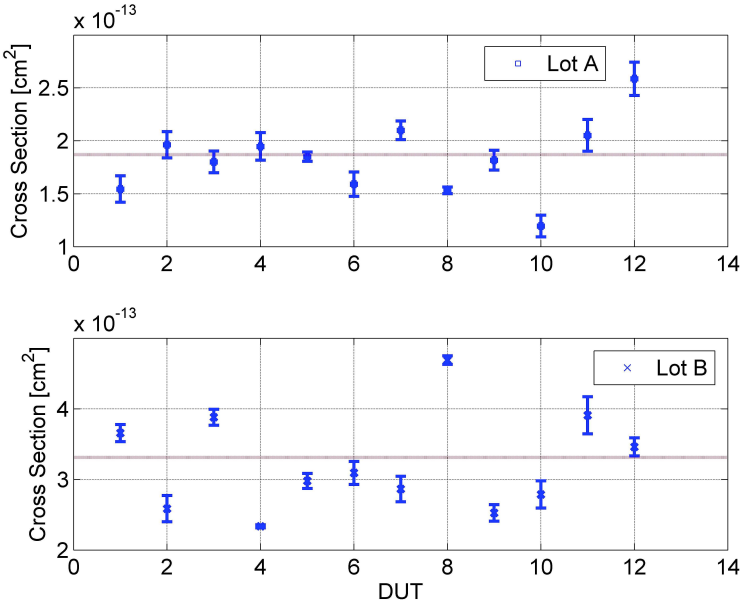

Figure 5-7: Average cross section per bit with protons at 230 MeV for 12 devices for lot A and lot B. The error bars refer to the repeatability calculated over three shots.

The results are summarized in the Table 5.2. Several tests have been performed also at lower supply voltage (2.5 V) but not significant changes have been measured. This is due to the presence of the internal voltage regulators which independently from the external power supply (in the datasheet range) regulates the cell array voltage.

Table 5.2: Summary of the cross section at 230 MeV for each memory lot. The cross section, the minimum resolution that can be achieved and the uncertainty are reported for a single memory and for a set of four devices used together.

	Average Cross section	1-σ	Minimum Resolution	Uncertainty
	[cm^2/bit]	[cm^2/bit]	pp/cm^2	$\pm$ pp/cm^2
Lot A x1	1.87x10^{-13}	4x10^{-14}	6.37x10^5	1.47x10^5
Lot B x1	3.31x10^{-13}	7x10^{-14}	3.6x10^5	7.56x10^4
Lot A x4	7.48x10^{-13}	8x10^{-14}	1.59x10^5	1.7x10^4
Lot B x4	1.32x10^{-12}	1.4x10^{-13}	2.25x10^4	2.39x10^3

The difference between the cross section at 230 MeV and the other energies is a parameter to take into consideration when using the memory as a sensor in a mixed radiation field. Table 5.3 and Figure 5-18 report the mean of the cross sections at

the different energies normalized with respect to the 230 MeV value. The energy dependency has been found to be the same for both the lots. The cross section from 230 MeV to 60 MeV decreases by around 10%. Although this value is comparable with the repeatability of the measurement the cross section tendency to decrease is evident. Below 60 MeV, and especially at 30 MeV the proton beam cannot be considered as monochromatic since the degraders enlarge the energy spectrum of the incoming particles. However, this side effect does not change the main outcome of the test: the decrease of sensitivity becomes more pronounced and the cross section value at 30 MeV is halved with respect to the one at 230 MeV.

The tests at TRIUMF show that the cross section is not saturated at 230 MeV but continue to slightly increase with the energy. The cross section at 355 MeV and 480 MeV is a factor 1.2 and 1.4 larger than at 230 MeV, respectively (Table 5.3). A cross calibration has been done between the TRIUMF and PSI results at 230 MeV by testing the same chip in the two facilities. The cross section measurements are in agreement with less than 1% of difference. The increase of the cross section at high energi interaction es is due to the fact that the entire first metallization layer of the memory is made by Tungsten. As already seen in [91, 92] for SEL effect, the high LET fragments cross section increases with the energy of the incoming particle (protons) in presence of an High Z material. This, in turn can lead, to a higher SEU cross section [93].

Table 5.3: Normalized Cross section for protons.

Test	Energy [MeV]	Normalized cross section
PSI	29	0.57
	47	0.85
	60	0.92
	80	0.89
	100	0.93
	150	0.98
	200	1.02
PSI/TRIUMF	230	1.00/1.01
TRIUMF	355	1.19
	480	1.38

5.3.2 Thermal Neutron Test

The thermal neutron test was carried out at the REZ facility. Three boards each containing 8 DUTs have been tested. Two cards were populated with memories from

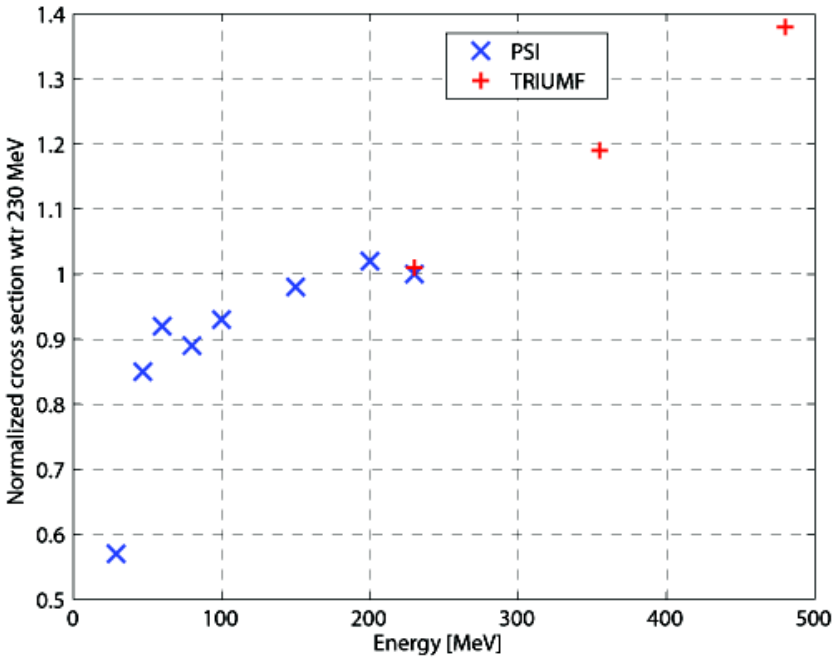

Figure 5-8: Protons cross section as a function of the incoming particle energy.

the lot B and one with the chips from the lot A. The measurements have been carried out in the static mode using 300 seconds for the reading time in order to be able to collect around 300 SEUs per run on each chip leading to a $1 - -\sigma$ statistical error of around 6%. The test has been performed also at different voltages to verify if the sensitivity increases by lowering the voltage supply. The results of the tests are reported in Table 5.4, in which the mean and the standard deviation for 8 DUTs is reported for each board and each supply voltage. Being the average cross section for thermal neutron in the order of $4x10^{-16}$ cm^2/bit, the Cypress has a cross section for thermal neutron more than a factor 400 lower than the one at 230 MeV. The low sensitivity of the Cypress to the thermal neutrons ensures that the measurements of the HEH fluences are not influenced by the thermal part of the LHC spectra. The performances of the memory in a mixed field are discussed in details in paragraph 5.4.2 and 5.4.1.

5.3.3 Neutrons test

As stated before, the neutrons at energies below 20 MeV can still penetrate the device reaching the sensitive volume, hence the cross section is measured with 5, 8 and 15 MeV monoenergetic neutron beam. Given the relatively low flux of the facility, it

Table 5.4: Summary of the thermal neutrons cross section for the two lots, tested with two different power supplies.

Lot	Board	Supply Voltage [V]	Flux [thn/cm^2/s]	Fluence [thn/cm^2]	Average Cross Section [cm^2/bit]	Std [cm^2/bit]
B	1	2.5	1.73×10^8	5.19×10^{10}	4.85×10^{-16}	8.24×10^{-17}
B	1	3.3	1.73×10^8	5.19×10^{10}	4.76×10^{-16}	5.15×10^{-17}
B	2	2.5	1.73×10^8	5.19×10^{10}	4.44×10^{-16}	3.38×10^{-17}
B	2	3.3	1.73×10^8	5.19×10^{10}	4.56×10^{-16}	4.06×10^{-17}
A	1	2.5	1.73×10^8	5.71×10^{10}	4.11×10^{-16}	3.24×10^{-17}
A	1	3.3	1.73×10^8	1.04×10^{10}	3.84×10^{-16}	7.50×10^{-17}

was not possible to make repeated measurements on the same chip. Four SRAMs belonging to the same lot were tested in parallel on the same board. The number of cumulated SEU counts per each chip was at least 300, thus with a statistical count error of ±6%. The mean and the standard deviation of the cross sections of the four chips were calculated for the three energies and the results reported in Table 5.5.

Table 5.5: Mono–energetic neutrons cross section.

Lot	Energy	Average cross section	Standard deviation
	[MeV]	[cm^2/bit]	[cm^2/bit]
LOT B	14.8	1.09×10^{-13}	2.66×10^{-14}
LOT B	8	2.16×10^{-14}	1.41×10^{-15}
LOT B	5	9.30×10^{-15}	4.39×10^{-16}
LOT A	14.8	6.09×10^{-14}	8.30×10^{-15}
LOT A	8	1.80×10^{-14}	5.64×10^{-16}
LOT A	5	9.47×10^{-15}	4.34×10^{-16}

All these results are discussed in the Section 5.4.2, in which the use of the SRAM in a mixed radiation field is described.

5.3.4 Burst events on Cypress memory

A dependency of the cross section on the Chip Select (CS) signal has been discovered by reading two memories with the "RadMon type" method. The Chip Select signal, which activates the control circuitry for the read/write operations, was enabled only during the reading and writing cycles for the first memory while it was always active on the second one. In these test conditions, the second memory presented a higher cross section. To analyze the effect of the CS, a test was carried out by keeping the CS signal always active for the entire run by using the "RadMon type" reading method. The number of SEUs collected in the run with the CS always active (named "Chip Select" in Figure 5-9) is around a factor two higher than the one got with a run

with the CS active only during the reading and writing operations (named "NO chip select"). The results are depicted in Figure 5-9 and the numerical values are reported in Table 5.6.

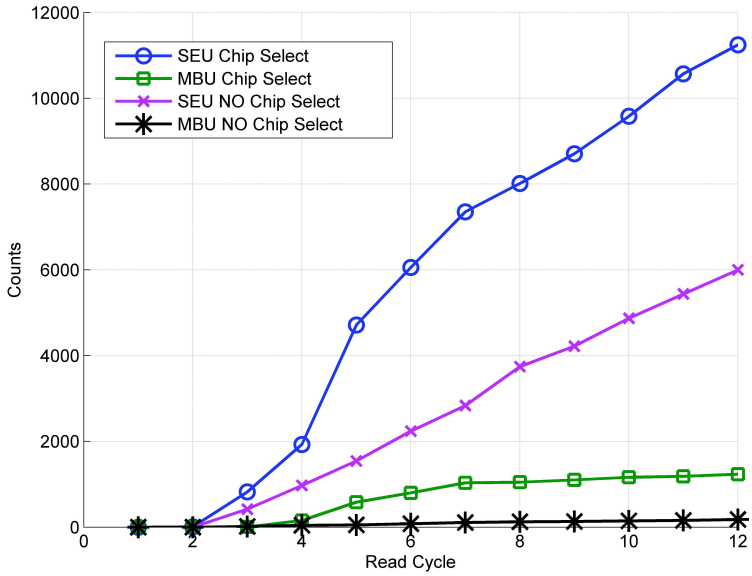

Figure 5-9: Number of SEU counts as a function of the reading cycle (each 2 seconds). The label Chip Select in the legend indicates the cases for which the chip select was always active during the run. The label NO Chip Select refers to the cases for which the chip select was not activated during the run.

Table 5.6: Cross section comparison with the Chip Select signal active.

Chip Select Active	Cross Section [cm2/bit]	SEU Counts
No	1.47x10-13	7423
Yes	4.95x10-13	12575

Furthermore, we analyzed the number of bits in error in the same bit line when the CS is kept enabled during the beam run. An increase of the MBU counts is observed and shown in Figure 5-9. The number of bits which are upset in a logic word of the memory is rarely larger than 3 for the condition "No Chip Select". Conversely, the number of upset bits in a single word overcomes the three bits when the Chip Select is enabled during the entire run (Figure 5-10). During other tests carried out at a lower flux with the "RadMon Type" mode, the burst events become more evident on the

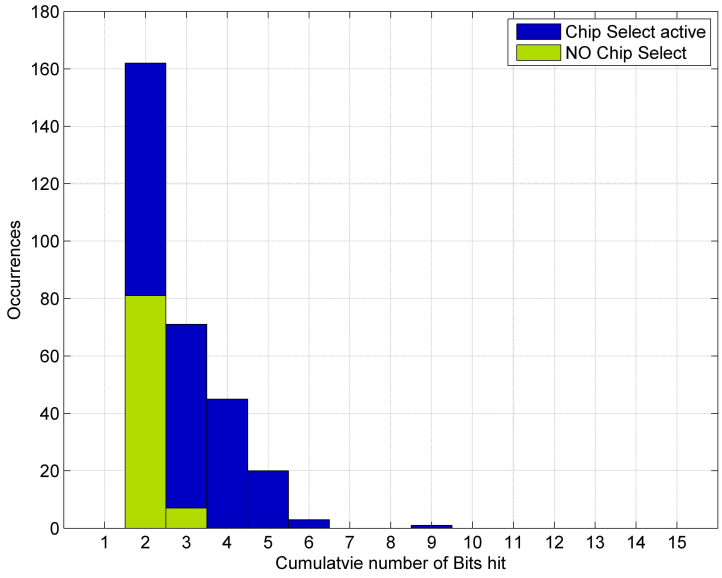

Figure 5-10: Histogram of the number of upset bits in case of MBUs with CS inactive (yellow) and active (blue) during the run.

counts reading. In Figure 5-11 two burst events are underlined for an irradiation at a flux of $6.8 \times 10^6 pp/cm^2$. Therefore, in view of the usage of this memory as radiation sensor, a detailed analysis has been carried out to understand if the burst events can be recognized and therefore corrected for.

The recognition of the burst pattern was performed dumping the entire memory or part of it during the irradiation and analysing the data referring to the physical internal structure of the SRAM. The bit-map permitted to put in evidence that a burst event can be recognized because the hit cells belong to the same block (Figure 5-12).

Thus, an algorithm was developed to recognize if multiple SEUs in a single reading cycle have a burst signature and account them as one event. The procedure has been applied on the data of the past campaigns and successfully reduces the number of counts by a factor 5 (Figure 5-13). This method, can be applied on-line.

5.3.5 TID Robustness

The cross section dependency on the TID has also been assessed at PSI. The dose values for each irradiation are given directly by the facility. The equation used to calculate the TID is 5.11:

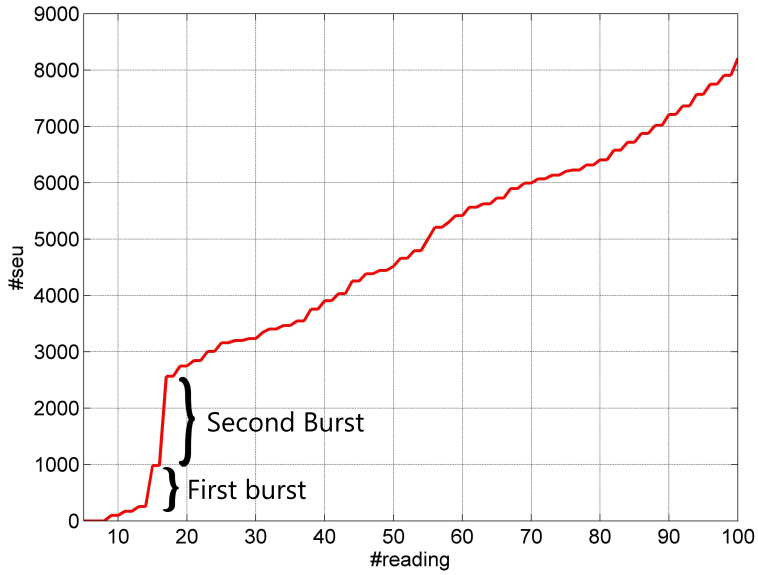

Figure 5-11: Example of burst events at low flux $6.82 \times 10^6 pp/cm^2$.

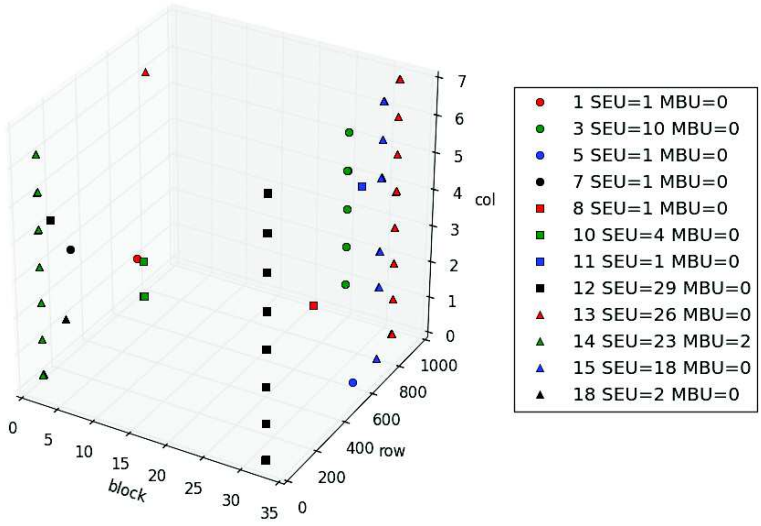

Figure 5-12: Bursts events analysis recovering the information on the block, row and column. The burst events are characterized by multiple bit in upset in the same block.

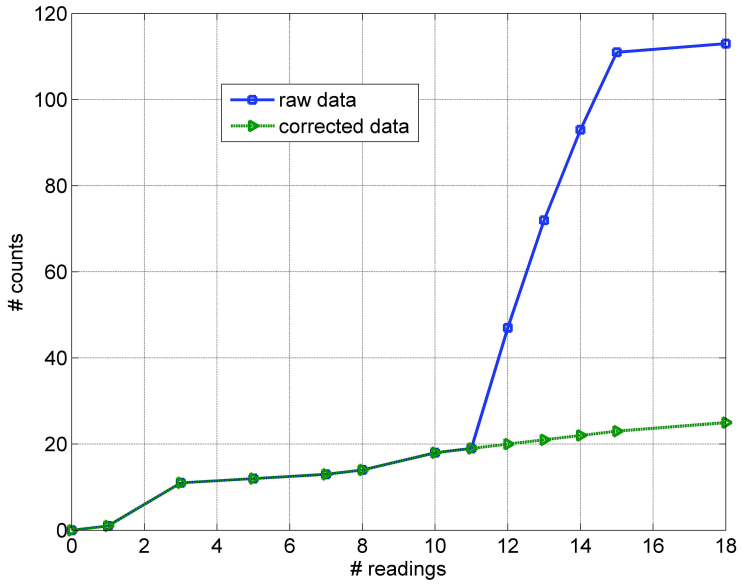

Figure 5-13: Raw readings and efficency of the bursts mitigation algorithm are depicted together.

$$Dose(rad(Si)) = LET(Si) \cdot \Phi \cdot 1.5 \times 10^{-5} \tag{5.11}$$

Where the Linear Energy Transfer (LET) is a function of the incoming proton energy and has units of MeV-cm^2/mg. The fluence Φ, expressed in cm^2, is obtained from the computer controlling the exposure. The test was carried at 230 MeV on a chip which had already cumulated 6 krad(Si). The cross section starts to decrease above ∼30 krad(Si) and becomes 60% of the initial values at 62 krad(Si), as depicted in Figure 5-14. During the test we inverted the pattern (all zeros to all ones) at intermediated TID levels in order to verify if the cross section variation could be due to an imprinting effect; the results were consistent with those obtained using the initial pattern of all zeros and showed that the bit pattern does not play a role on the TID effects.

The memory shows a big dependency with the cumulated TID. Luckly, this effect can be neglected in the actual version of the RadMon because the memories are installed on the motherboard which is radiation tolerant up to 25 krad. Before having cumulated this amount of dose, the RadMon undergoes to a preventive substitution.

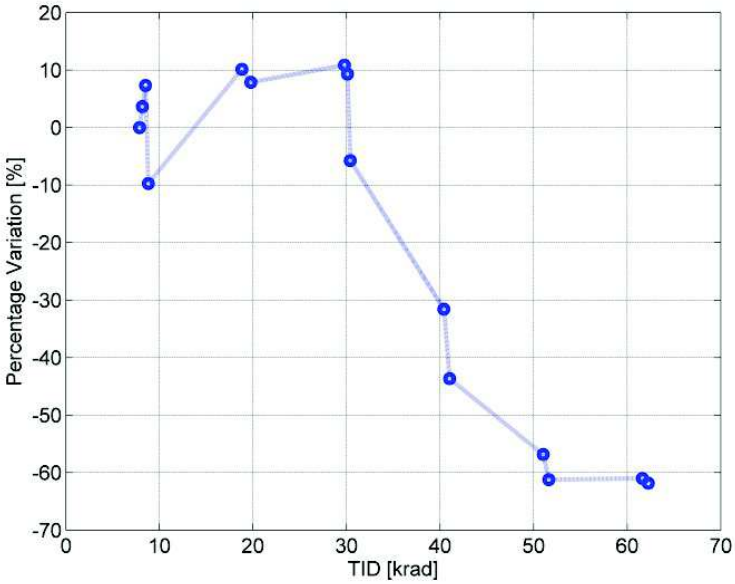

Figure 5-14: Cypress cross section dependency as a function of the TID.

5.3.6 Toshiba SRAM

The Toshiba memories have been calibrated following the same procedure used for the Cypress. The process of re–qualification of this component was necessary because several new batches of this type of memories were bought. In this work the protons and thermal neutrons tests have been carried out. The intermediate energy neutrons response is based on the test carried out in [94].

5.3.7 Toshiba cross section for protons, thermal neutrons and neutrons at intermediate energies

The proton test have been carried at PSI with the energy of the proton in the range 30 – 230 MeV. The flux used was around $2.20 \times 10^8 cm^2$. As already mentioned (see chapter X) the cross section depends on the supply voltage. Indeed it was found [95] that this applies to the Toshiba memories and we take advantage of this effect for the measurements of the HEH and of the thermal neutrons (see Paragraph 5.4.1).

Several lots (memories with the same date code) have been tested during the years. A summary of the measurements carried out on three lots is reported in Table 5.7. The test performed in the 2014 5.8, are carried out on the two lots of which we have the largest furniture and will be used for the RadMon installation. The average

cross section of different lots of Toshiba memories it changes only of around 15% and it is close to the sample–to–sample variation of a given lot.

Table 5.7: Summary of the Toshiba memories protons cross section for the lot 443-438-442. The average cross section and the standard deviation are calculated for each lot.

	Lot 443	Lot 443	Lot 438	Lot 438	Lot 442	Lot 442
	PSI 2011	PSI 2011	PSI 2012	PSI 2012	PSI 2012	PSI 2012
	5 V	3 V	5 V	3 V	5 V	3 V
Cross section [cm2]	2.95×10^{-14}	6.50×10^{-14}	2.28×10^{-14}	5.56×10^{-14}	3.50×10^{-14}	6.00×10^{-14}
Std [cm2]	6.61×10^{-15}	1.64×10^{-14}	2.89×10^{-15}	4.86×10^{-15}	1.02×10^{-14}	7.52×10^{-15}
std/mean [%]	22.4	25.2	12.7	8.7	29.1	12.5
Diff wrt lot 443 [%]			-22.712	16.9	-15.7	8.3

Table 5.8: Latest tests carried out on the new lots 440 and 441.

	Lot 440	Lot 440	Lot 441	Lot 441
	PSI 2014	PSI 2014	PSI 2014	PSI 2014
	5 V	3 V	5 V	3 V
Mean Cross section [cm2]	2.63×10^{-14}	5.44×10^{-14}	2.57×10^{-14}	5.46×10^{-14}
Std deviation [cm2]	2.73×10^{-15}	7.23×10^{-15}	1.71×10^{-15}	3.95×10^{-15}
std/mean [%]	10.4	13.3	6.6	7.2
Diff wrt lot 443 [%]	-10.9	-16.3	-12.7	-15.9

The energy dependency of the cross section has been measured in several test campaigns. As already done with the Cypress memories, an energy scan from 30 to 230 MeV was carried out. The cross section as a function of the energy is depicted in Figure 5-15 for both the supply voltage, 5 V and 3 V. Looking at the results we can confirm that there is no dependency of the Toshiba cross section as a function of the energy.

A proton test at 60 MeV was carried out in [96] to understand the cross section dependency with the accumulated TID. The results reported also in Figure 5-16 show an increase of the cross section for TID higher than 111 Gy for 5 V and 160 Gy for 4 V.

No tests have been carried out on the TID–life time of the Toshiba memories, but we can extrapolate this information from the [97], which states that the memories exhibit a parametric failure at 20 krad(Si) due to an increase of the supply current.

One of the feature of this SRAM is to have a cross section for the thermal neutrons comparable with the one of the protons lowering the supply voltage. This feature can be exploited, as it will be discussed later in the chapter, to measure the thermal neutron fluence.

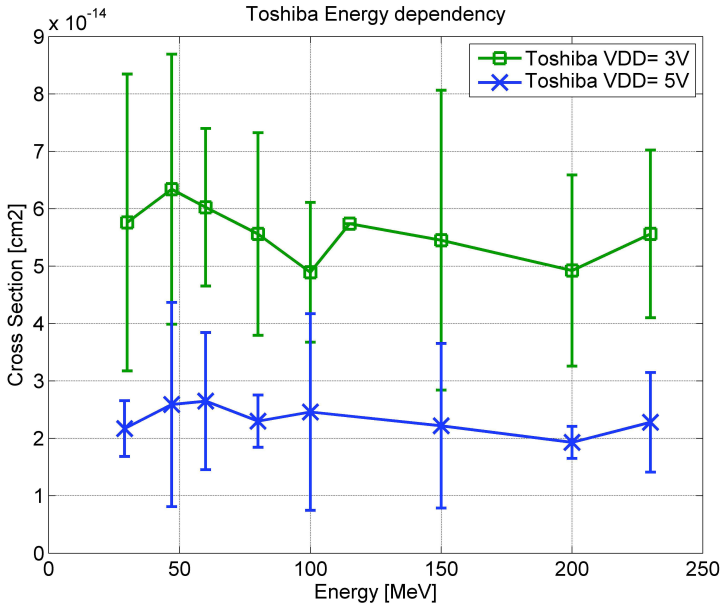

Figure 5-15: Energy dependency of the Toshiba cross section for two different supply voltages, 5 V and 3 V.

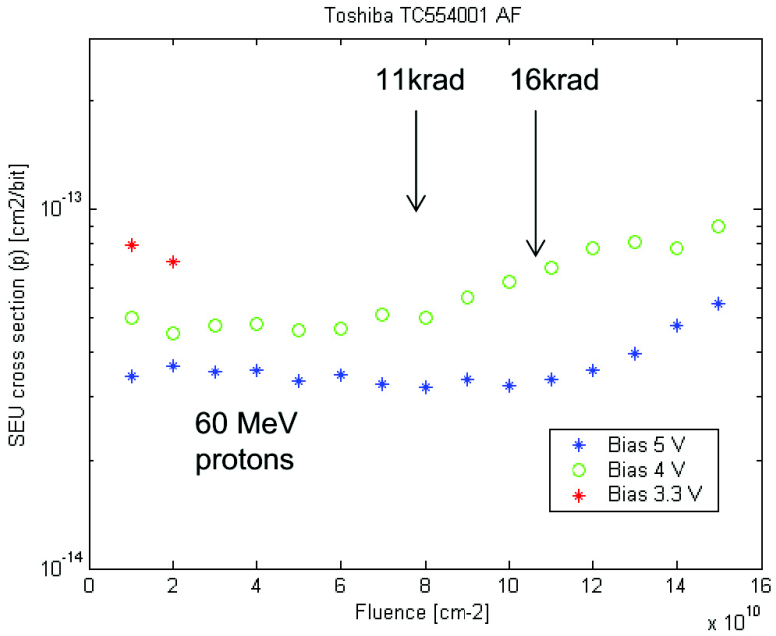

Figure 5-16: TID dependency on the Toshiba cross section for two supply voltages, 5 V and 4 V [96].

The thermal neutrons tests have been carried out on several lots, the measurements which resulted to be in a very good agreement for all the lots have been joined to give only one value of cross section. The average and the standard deviation of the cross sections for the thermal neutrons at two voltage supplies (5 V and 3 V) are reported in the Table 5.9. The large cross section for thermals is due to the technological process, indeed one of the factor is the passivisation layer made with a borophososilicate glass (BPSG).

Table 5.9: Toshiba Thermal Neutrons cross section for two voltage supplies, 5 V and 3 V.

Toshiba				
	Voltage	Mean cm^2	Standard deviation cm^2	ration proton 230MeV/thn
Toshiba 438/440/441/442/443	3V	1.55×10^{-13}	7.47×10^{-14}	0.35
Toshiba 440/441/442	5V	2.61×10^{-15}	1.8×10^{-15}	14

In the Table 5.9 the ratio with the proton cross section at 230 MeV is reported. The cross section for protons at 5 V of power supply is around 14times higher the one for thermals, while at 3 V the cross section for thermal is around 2 times higher the one of protons.

5.4 Use of the SRAM as Hadron fluence counter on the new RadMon

5.4.1 Strategy for discriminating HEH and Thermal neutrons

The strategy used for the measurement of the thermal neutrons in the LHC is based on the the observation, already discussed in the previous paragraph, that lowering the biasing voltage of an SRAM cell, the thermal neutron cross section becomes as large as the proton cross section at the same supply voltage. The SEU cross-section is expected to decrease linearly with the supply voltage but for the thermal neutrons, the ratio of the sensitivity at different voltages was largely exceeding the simple reduction of the critical charge [98]. Based on this, it is proposed to combine the RadMon SRAM SEU measurements at two different voltages to estimate the ratio between the thermal neutron and high energy hadron fluence. The contribution of SEUs at a given voltage "V" can be written as :

$$N_{SEU}(V) = \sigma_{HEH}(V) \cdot \Phi_{HEH} + \sigma_{th}(V) \cdot \Phi_{th} \tag{5.12}$$

where $\sigma_{HEH}(V)$ and $\sigma_{th}(V)$ are the HEH cross section and the thermal neutron cross section as a function of the supply voltage. If two measurements at two different supply voltages are carried out, the relation 5.12 results in a system of two linear equations with two variables. If the cross section for the two types of particles differs changing the supply voltage, as the case of the Toshiba memories, carrying out two measurements at two voltages $V1$ and $V2$, the resulting equation are:

$$\Phi_{HEH} = \frac{N_{SEU}(V1) - \sigma_{th}(V1) \cdot \Phi_{th}}{\sigma_{HEH}(V1)} \tag{5.13}$$

$$\Phi_{th} = \frac{N_{SEU}(V2) - \sigma_{HEH}(V2) \cdot \Phi_{HEH}}{\sigma_{th}(V2)} \tag{5.14}$$

In the (5.13) it is supposed that V1 is the supply voltage at which the cross section for HEH is higher than the one for thermals, viceversa for the equation (5.14). To be able to evaluate with a certain accuracy the HEH and the thermal neutrons fluences, the cross sections of the SRAM should be very different for the same supply voltage for the HEH and the thermals.

We can "design" our measurement system in order to achieve a certain accuracy. Considering that we want an accuracy of at least k % on the measurements of the Φ_{HEH}, this results in the statement:

$$\frac{\sigma_{th}(V1) \cdot \Phi_{th}}{\sigma_{HEH}(V1)\Phi_{HEH}} < k \tag{5.15}$$

We have already discussed about the 'risk factor' or 'R–Factor' which is defined as follows:

$$R = \frac{\Phi_{th}}{\Phi_{HEH}} \tag{5.16}$$

Using the (5.16) the equation (5.17) can be rewritten as:

$$\frac{\sigma_{HEH}(V1)}{\sigma_{th}(V1)} > \frac{R}{k} \tag{5.17}$$

This means that the ratio R, which depends on the environment, affects the accuracy k. Taking the cross section for thermals and for protons at 230 MeV of the Cypress memory, we can calculate at which value of R the system has an accuracy lower than 30% (k) for the HEH fluence by doing only one measurement at a given supply voltage. This exercise for the lot A, led to the conclusion that the HEH fluence measurements with the Cypress has an accuracy lower than 30% wherever the R factor is below 100, hence when the thermal neutrons fluence is 100 times less

than the HEH fluence. The Toshiba cross section for thermals at 5 V is 10 times smaller than the one with protons, this led to an accuracy of the 30% only in the location in which the thermal neutrons fluence is only three times smaller than the HEH fluence (R<3).

Having the two types of memories (Toshiba and Cypress) working at the same time on the RadMon, the thermal neutrons fluence can be calculated in two different ways. The first method is described in [98], and exploits the increased Toshiba cross section for thermals with respect to the one for HEH at the supply voltage of 3 V. Indeed, the term $V1$ in the equation 5.13 is 5 V and $V2$ in the 5.14 is 3 V. Using the 5.13, 5.14, the ratio R can be rewritten as:

$$R = \frac{\sigma_{HEH}(3V) \cdot N_{SEU}(5V) - \sigma_{HEH}(5V) \cdot N_{SEU}(3V)}{\sigma_{th}(5V) \cdot N_{SEU}(3V) - \sigma_{th}(3V) \cdot N_{SEU}(5V)} \tag{5.18}$$

Two measurements are needed, at 5 V and at 3 V on the same RadMon ($N_{SEU}(5V)$ and $N_{SEU}(3V)$). This was the method used on the RadMon V5.

With the new version of the RadMon the Cypress memories can be used in place of the Toshiba to evaluate the HEH fluence assuming not to be affected by the thermal neutrons (at the conditions for for R and k already discussed), then the thermal neutron fluence is calculated by means of the Toshiba at 3V (5.14). The resulting equation for R would be:

$$R = \frac{\sigma_{HEH}(3V) \cdot N_{SEU_{Cypress}} - \sigma_{HEH_{Cypress}} \cdot N_{SEU}(3V)}{\sigma_{th_{Cypress}} \cdot N_{SEU}(3V) - \sigma_{th}(3V) \cdot N_{SEU_{Cypress}}} \tag{5.19}$$

where $N_{SEU(3V)}$ and $N_{SEU_{Cypress}}$ refer to the Toshiba and Cypress counts respectevely. The advantage of this method with respect to the one of carrying two measurements with the Toshiba is the higher accuracy due to the low sensitivity of the Cypress memory to thermals.

5.4.2 Measurements in the LHC mixed radiation field

In this section we discuss how to apply the obtained data of the radiation tests to use the SRAM Cypress as a hadron flux counter in the LHC mixed radiation field. The knowledge of the energy response of the memories reduces the uncertainty on the HEH fluence estimation for the installation areas where the radiation field spectra are available. In fact, the HEH fluence is given by:

$$\Phi_{HEH} = \int_{E_{threshold}}^{20MeV} \mathrm{w_n}(E)\phi_n(E), \mathrm{d}E + \int_{20MeV}^{\infty} \mathrm{w_p}(E)\phi_p(E), \mathrm{d}E \tag{5.20}$$

Where $E_{threshold}$ is the SEU threshold energy for neutrons below 20 MeV, typically the value of 0.2 MeV is used since it is the threshold energy for the alpha production in nitrogen. $w_n(E)$ is the weighting function for neutrons above $E_{threshold}$, $w_p(E)$ the weighting function for HEH above 20 MeV, and $\phi_n(E)$ and $\phi_p(E)$ are the neutron and HEH differential fluences, respectively. The equation is slightly different from the one in [94] because the HEH contribution is not anymore considered as a step function above 20 MeV but is weighted by the function $w_p(E)$, which takes into account the fact that the protons cross-section is not saturated above 20 MeV for the Cypress SRAM (Section 5.3.1). The different responses of the SRAM to protons and neutrons allow to weight neutrons and charged particles separately. The effect and consequence of this dependency are discussed later in this paragraph.

A Weibull fit function, given in the equation 5.21, where W and S are the shape parameters, w_{sat} is the saturation value of the cross section, and $E_{threshold}$ is the threshold energy for inducing SEUs, is used to evaluate $w_n(E)$ exploiting the data at 5, 8, 14 MeV.

$$w(E) = w_{sat} \cdot \left(1 - e^{\left(-\left[\frac{(E-Eth)}{W}\right]^S\right)}\right) \tag{5.21}$$

For the neutron cross-section the saturation value is fixed to the same value of the protons cross-section at 230 MeV based on the assumption that at energies above 50 MeV the nuclear cross-section for these particles is very similar [84]. The Weibull fit and the parameters are reported in Figure 5-17.

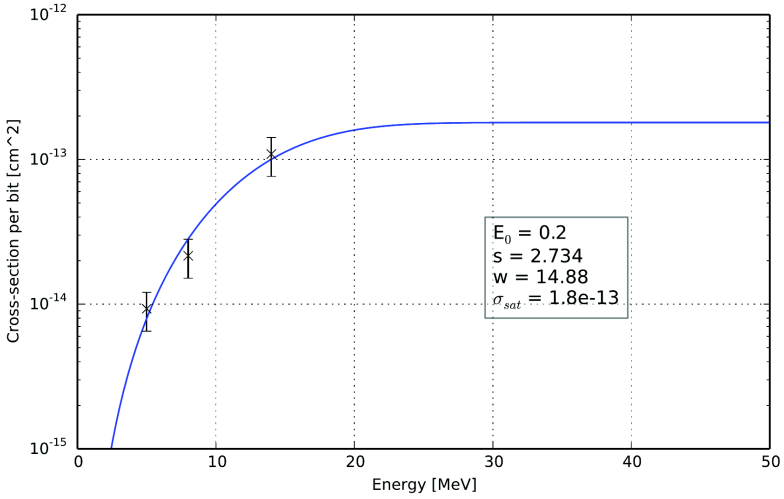

Figure 5-17: Fitting curves and parameters for the neutrons data set.

The function $w_p(E)$ for the protons is retrieved as the union of two fit functions to take into account that the cross section does not saturate above 230 MeV. The Weibull fit has been used in the 30-230 MeV range and a two parameter (m, k) power law function 5.22 for energies above 230 MeV.

$$w(E) = k \cdot E^m \tag{5.22}$$

The two functions are depicted in Figure 5-18 with the parameters of the equation (5.21) and (5.22).

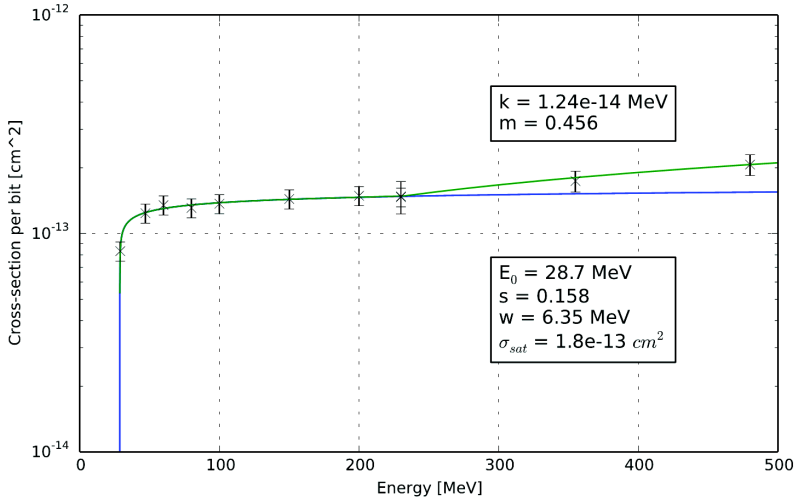

Figure 5-18: Fitting curves and parameters for the protons data set. A power law function is used for energies above 230 MeV.

A study was performed to understand the impact on the measurement accuracy of the drop of the protons cross section at energies below 60 MeV and the increase above 230 MeV. For this purpose, three LHC environments have been simulated (LHC tunnel, the RR alcove and UJ alcove) [99]; the results of the convolution of the spectra of each environment with the weighting functions permit to evaluate the "effective cross sections" of the Cypress memory, which is a fixed number for a given area used to convert the SEU counts in the HEH fluence. Table 5.10 reports the results of the simulation considering the data of the SRAM belonging to the lot A. The "step function approach" considers that the SRAM cross section is constant above 20 MeV. In the equation (5.20) the function $w_p(E)$ is set equal to 1 and $w_n(E)$ to 0. In the second approach ("Weibull fit"), only the Weibull fit of the equation (5.21) is considered as weighting function considering that the cross section saturates at 230 MeV. In the third approach (referred to as "power law"), the weighting function

takes into account the increments of the cross section above 230 MeV combining the equation (5.21) and (5.22). For all three cases, the weighting function w_n for the 5-20 MeV range is always the Weibull fit.

Table 5.10: Effective cross section in different LHC environment.

	cm^2/bit/HEH
LHC tunnel	
Step Function approach	1.99×10^{-13}
Weibull fit	1.83×10^{-13}
Power law	2.41×10^{-13}
RR alcove	
Step Function approach	2.09×10^{-13}
Weibull fit	2.01×10^{-13}
Power law	2.07×10^{-13}
UJ alcove	
Step Function approach	2.23×10^{-13}
Weibull fit	2.23×10^{-13}
Power law	2.20×10^{-13}

The type of the weighting functions does not affect the value of the effective cross section in the areas, like the RR and UJ alcoves because the contribution of both the HEH below 60 MeV and above 230 MeV is not dominant. The correction of the HEH below 60 MeV does not affect the results so drastically even in the LHC tunnel environments; indeed the difference considering a step function or the Weibull fit is around 8%. Conversely, in the LHC tunnel environment, being the spectra of HEH more "hard", the contribution of the HEH at high energy (>230 MeV) has more impact and the effective cross section is 30% higher considering the power law fit. This exercise shows how the accuracy of the hadron flux can be improved where the radiation spectra is known.

5.5 Summary

The measurements of the HEH and thermal neutrons fluence are carried out by using commercial SRAM on the RadMon. It is necessary to count the number of bits flipped and, knowing the cross section, retrieve the number of particles that hit the device. The cross section of the SRAM should be known before the measurements and thus, the SRAM should be characterized in an environment as close as possible to the one of the LHC. The SRAM used in the previous version of the RadMon are the Toshiba,

built with a 400 nm process. The new version of RadMon is capable of reading two banks of four memories and thus another memory type has been characterized: the Cypress CY62157EV30, based on a 90 nm process.

An appropriate test strategy to qualify the cross section of the SRAM has been developed. The process includes a proton test at various energies (30-480 MeV) to evaluate the SEL immunity, lot–to–lot variation and the inside the lot variation, the energy response and the response dependency with respect to the TID cumulated. Some technologies are sensitive to thermal neutrons, as the case of the Toshiba SRAM, for this reason, the second step is to foresee a thermal neutrons test. The last step is to evaluate the cross section at energies below 30 MeV with a neutron beam.

Several test campaigns have been carried out to characterize two lots of Cypress memories. The reference cross section is the one found with a proton beam at 230 MeV. The cross sections for the two lots are reported in Table 5.2. As pointed out in this chapter, having four memories installed on the RadMon reduce the minimum resolution and the uncertainty by a factor 2. The tests at higher energy show that the cross section is not saturated at 230 MeV but continue to increase slightly with the energy. The energy dependency is also visible at lower energy where the cross section is halved with respect to the one at 230 MeV. The thermal neutron cross section is around 400 times lower than the one at 230 MeV. The low sensitivity of the Cypress to the thermal neutrons ensures that the measurements of the HEH fluences are not influenced by the thermal part of the LHC spectra.

During some tests at low flux, some burst events on the Cypress have been found. We pointed out that one of the possible cause was the chip select signal that, when turned on for the entire irradiation, led to a cross section which was the double of the one without the chip select active. We recognize, thanks to the physical mapping of the memory, that the burst event belong to the same block. We managed to count and correct the burst events off-line but the same algorithm will be implemented in the FPGA for an online correction. The TID robustness of the Cypress memories has been verified during a proton beam test where the SEU and the TID effects act in synergy. The SEU cross section starts to decrease above 30krad and decreases at the 60% of the initial value at $\sim$62 krad(Si). Although the dependency with the TID is quite strong, this is not a limiting factor because the RadMon motherboard, which the memories are close to, can stand up to 25krad. In any case, before this amount of dose, the RadMon undergoes to a preventive substitution making the effect negligible.

The procurement of new lots of Toshiba memories implies a process of re–qualification. The proton tests have been carried with protons of energies in the range of 30 – 230 MeV. No dependency of the cross section on the incoming particle energy has been

measured. The cross section at 230 MeV has been measured at two supply voltage 3V and 5V, the average cross sections for two lots are reported in Table 5.8. The Toshiba cross section is around a factor 10 lower than the Cypress one. The Toshiba SRAM being developed in with an old technology process (BPSG layer for passivation) have a cross section for the thermal neutrons comparable with the one of the protons lowering the supply voltage. This feature can be exploited to measure the thermal neutron fluence. Indeed, in the paragraph 5.4.1 it has been described how to use the Toshiba memories to measure the R factor making two measurements at two voltages. In the same paragraph, we have highlighted that using the Cypress memory for the HEH fluence estimation and the Toshiba at low voltage increases the accuracy of the thermal neutrons measurements with respect to the technique of carrying two measurements at two voltages with the Toshiba memory.

In the last paragraph of this chapter, we have discussed about how to apply the measured cross sections for the Cypress memories in the context of the mixed radiation field measurements. The concept of the "effective cross section", which is the result of the convolution of the spectra of a selected LHC environment with a weighting function, has been explained. The effective cross section permits to achieve an higher accuracy weighting the memory response at different energy with the radiation spectrum of a defined zone. We showed that the effective cross section is affected by the environment when the radiation spectrum becomes more "hard" and the worst case is when we consider the increment of the cross section at high energy as the case of the Cypress memory.

Chapter 6

Floating Gate Dosimeter

In this chapter the floating gate dosimeter will be presented. In order to understand the working principle as a radiation dosimeter, the floating gate structure with its electrical characteristic is described. The radiation effects on the floating gate structure permits to understand how to use this kind of structure as a radiation dosimeter. The floating gate and its embedded circuit is a complex device which integrates several functionalities, detailed and explained in the following chapter. Because of its complexity a modular measurement setup has been built for the characterization and the calibration. The results of several tests carried out in a mixed radiation facility at CERN, in ^{60}Co gamma and in a proton beam are analyzed and discussed. An analytical model of the sensor is presented and the theoretical sensitivity for the prototype of FGDOS is evaluated. Finally, the model allows measuring the charge yield for different particle types and different energies accurately.

6.1 Working principle

6.1.1 Introduction to the Floating Gate MOS devices

The first floating structure has been reported in 1967 by [100]. This kind of structure was used for non–volatile data storage in EEPROM, EPROM and Flash Memories. Only in the 1989 the floating gate structure was studied to be used for non–storage applications; the neural processing was one of the possible use of the floating gate structure [101]. In the same years a patent [102] pointed out the possibility to exploit a kind of floating structure as a radiation dosimeter.

For the understanding of this device, the key structure to analyze is a basic Floating-gate Avalanche Injection MOS (FAMOS). The functionalities of a FAMOS can be traced out by studying the floating gate potential. The schematic cross section

of a generic FAMOS device is shown in 6-1. The upper gate is the control gate and

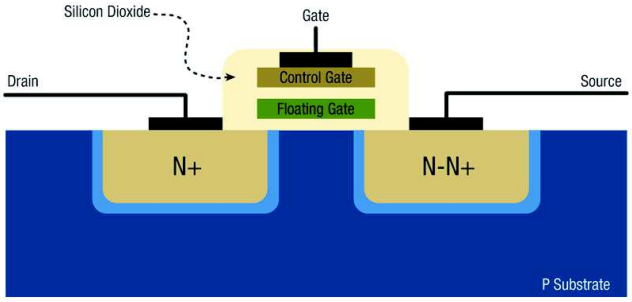

Figure 6-1: FAMOS structure. The polysilicon gate is left floating, surrounded of SiO_2.

the lower gate is the Floating Gate structure (FG) which is built with a conductive layer isolated within the dielectric (SiO_2). The charges on the floating gate determine if the transistor conducts when a (read) bias condition is applied on the gate. Being the floating gate completely surrounded by insulators, its charges are retained for a long period of time.

Before analyzing the FAMOS structure, let's consider an ideal transistor with no charge layer in the gate insulator as depicted in Figure 6-2.a,. In Figure 6-2.b a sheet of electrons at distance d from the silicon channel surface is added. The results of the charge distribution in the dielectric is a shift of the MOSFET threshold voltage 6-2.c . The ammount of V_{th} shift depends on the distance d and the amount of the charges; the equation of the V_{th} could be rewritten as :

$$V_{th} = V_{th0} - \frac{Q \cdot d}{\epsilon_{ox}} \tag{6.1}$$

where V_{th0} is the initial V_{th} and ϵ_{ox} is the dielectric constant of the oxide.

The threshold voltage impacts the dependency of the source–drain current of the transistor as a function of the gate–source potential. Figure 6-2.c shows the characteristic curves shift as a function of the stored charge. If electrons are added to the gate insulator region, the curve will move in a positive direction.

If now we go back to the FAMOS device, the floating gate provides a favorable accumulating site for the charge to modify the V_{th}. The energy band structure for a simple floating gate device is shown in Figure 6-3; the silicon substrate is shown on the left side of the picture above while the n–type control gate is on the right. The polysilicon gate doped n–type is in the middle, within two silicon dioxide layers. The FG is electrically isolated by the high energy barriers between the conduction band of the polysilicon and that of the top and bottom SiO2 layers. These barriers assure the

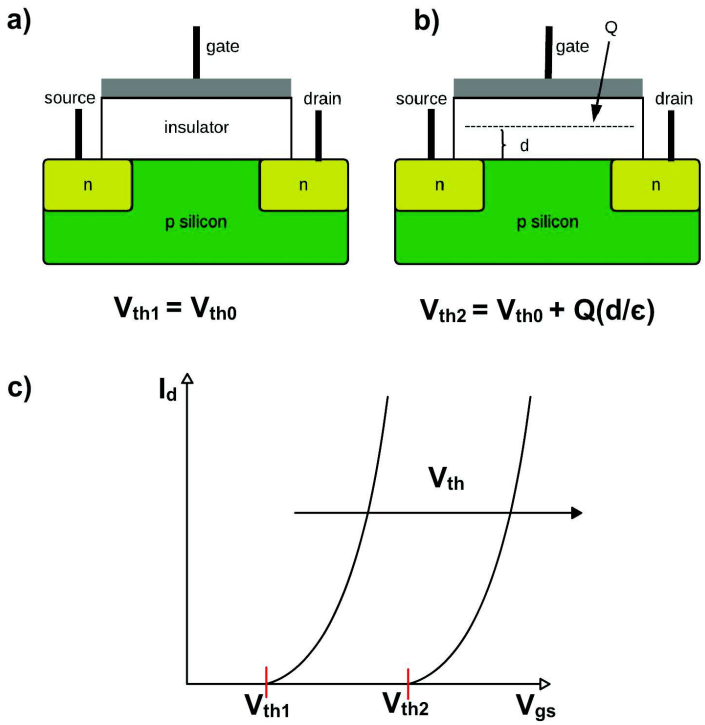

Figure 6-2: V_{th} shift as a function of the charges in the oxide. a) Empty dielectric, no charges stored in the oxide. b) Sheet of electrons at distance d from the interface Si-SiO_2. c) V_{th} shift due to the electrons in the oxide. To be noticed the positive shift of the V_{th} due to negative charges in the oxide.

non–volatile retention of the FG charge since the energy necessary to overcome them is higher than the thermal energy. To change the amount of charges stored on the floating gate is necessary to change the potential of the floating gate with the respect to the SiO_2 layers until a conduction mechanism is invoked to overcome the barrier or tunnel through it. The effect of the conduction mechanism is to inject charges in the floating gate; the Figure 6-4 shows the modification of the energy bands because of the electrons stored in the floating gate.

Channel Hot Electron (CHE) and Fowler-Nordheim tunneling are two common mechanisms used for the charges injection in the FG gate. To invoke CHE injection a lateral channel electric field on the order of 10^5 V/cm is required to accelerate electrons to energy levels above the barrier height. Some of those electrons will be scattered by the lattice and be directed toward the floating gate. To actually reach the floating gate, the scattered electrons must retain sufficient energy to surmount the silicon to insulator barrier and cross the insulator to the floating gate. CHE is an inefficient

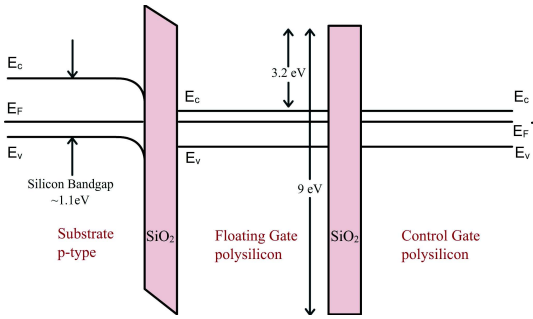

Figure 6-3: Band structure for a FAMOS device in a non–programmed state.The floating gate made of polysilicon is confinated by the two high potential barriers of the SiO_2 layers.

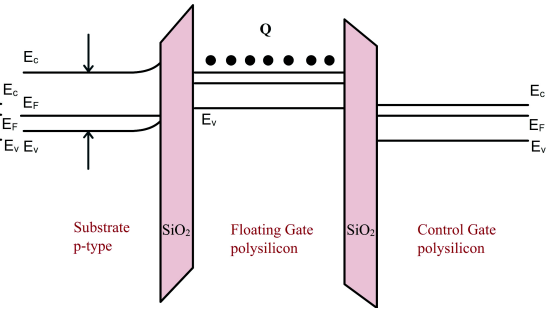

Figure 6-4: Band structure for a FAMOS device after electrons injection in the Floating Gate. The injected charge is confinated by the two high potential barriers of the SiO_2 layers.

method because less than about 0.001% of the channel current will be directed to the floating gate; this is one of the reason to name a model used to characterize this phenomena "the lucky electron" [103]. If we consider a MOS in conduction mode, an electron traveling from the source to the drain gains energy from the lateral electric field and looses energy to the lattice vibrations (acoustic and optical phonons). This is an equilibrium condition at low fields and it is kept until the field reaches around 100 kV/cm . For fields exceeding this value, electrons are no longer in equilibrium with the lattice, and their energy begins to increase. Electrons are "heated" by the high lateral electric field and a small fraction of them gains enough energy to surmount the SiO_2 barrier. To overcome this potential barrier the electron must have a kinetic energy higher than the potential barrier Si-SiO_2 and velocity directed towards the FG.

Fowler–Nordheim (FN) tunneling is a quantum mechanical tunneling process where the electrons or holes can penetrate through the oxide barrier into the conduction band of the oxide. The cold electrons tunneling will occur when a field on the order of 8 to 10 MV/cm is established across the insulator next to the floating gate. The process is slower than CHE injection, but is better controlled and more efficient. The Fowler–Nordheim current density J is expressed by the equation (6.2):

$$J = kE_{tun}^2 e^{\frac{E_c}{E_{tun}}} \tag{6.2}$$

where E_{tun} is the tunneling electric field while k and E_c are physical parameters depending on the material characteristics in which the tunneling is taking place [104].

This basic equation underlines that the tunneling current increases with the electric field. A band structure which compares the two process is depicted in Figure 6-5. In the CHE process the electrons must have enough energy to overcome the potential barrier due to the lateral electric field, while in the FN process the probability of tunneling increases with the gate electric field.

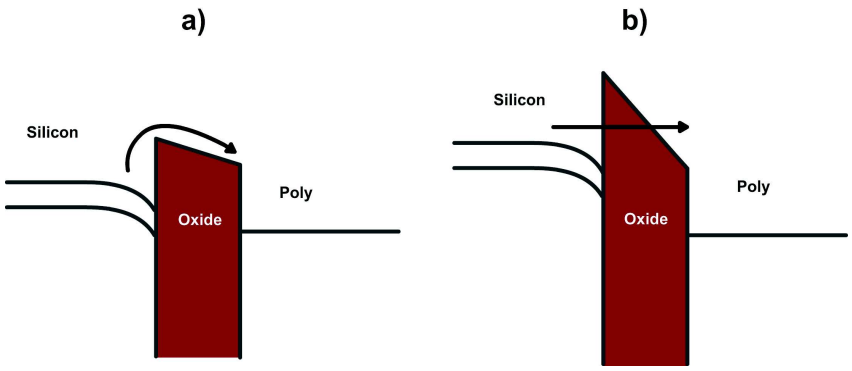

Figure 6-5: Band diagram of the two processes, CHE and FN, that are able to inject charges in the floating gate. a) Channel–hot–electron b) Fowler–Nordheim tunneling.

6.1.2 The Floating Gate Dosimeter working principle

The Floating Gate Dosimeter (FGDOS) is a radiation sensor based on a FAMOS structure. When a ionizing radiation impinges on a floating gate device three main mechanisms take place.

1. The injection of charge onto the floating gate due to the charge generation in the surround oxide.

2. Charge trapping in the floating gate oxide.

3. Photo–emission of carriers from the floating gate

The three mechanisms are depicted in the Figure 6-6 where the band structure of a "programmed" floating gate FAMOS is depicted, i.e. the floating gate is charged and no signal is applied on the control gate. The ionizing radiation generates charges in the oxide that are separated by the internal electric field between the control gate and the floating gate and the one between the floating gate and the substrate. The charges that escape the recombination are directed towards the floating gate or the substrate depending on their sign. Some of the holes that escape the initial recombination can be trapped in the oxide. The photo–emission [105] phenomenon is related to the

charges stored in the floating gate which acquire enough energy to overcome the oxide potential barrier and be ejected from the floating gate.

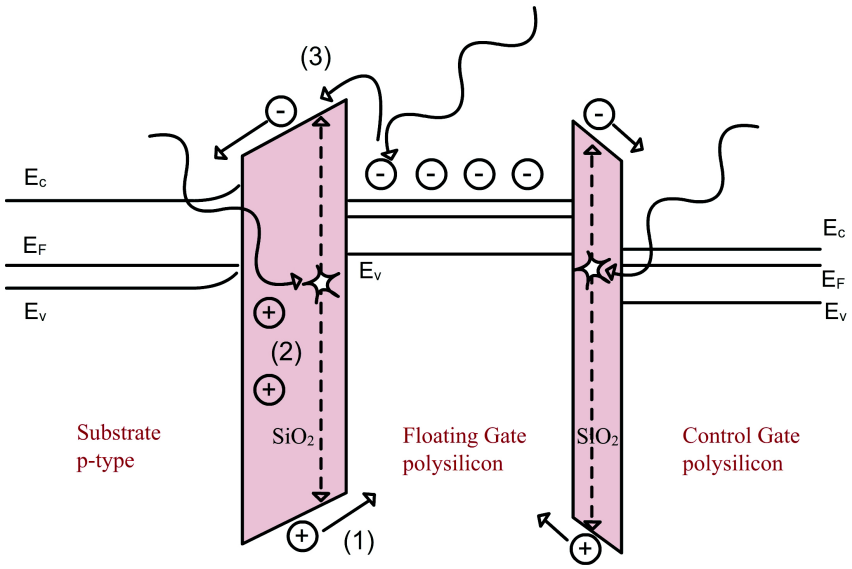

Figure 6-6: Three effects apply on a floating gate under exposure 1) Injection of charge 2) Charge trapping 3) photoemission.

The consequence of the radiation exposure on the FAMOS devices is a change in the threshold voltage V_{th}. In a flash based memory device, the shift of the V_{th} depends on the state (programmed or erased) of the cells [106]. In the Figure 6-7 the memory cell, which in the programmed state stores electrons, being exposed to X–rays radiation shows a decrement of the V_{th} . Instead, an increment in the threshold voltage in the erased state is noticed. The two different behaviors indicate that the second mechanism (the charge trapping in the oxide) cannot be a major factor in the device response to ionizing radiation. This is because trapped charges are usually positive and, they would cause a decrement of the threshold voltage in both cases. Moreover, the density of trapped charges in the tunnel oxide must be low due to the small oxide thickness of commercial memory devices. Hence, the major contributions are the injection of charge onto the floating gate and the photo–emission effect.

Based on this assumption a floating gate device can be used as a radiation dosimeter if the variation of the threshold voltage can be measured. The structures for exploiting this effect have been studied in the past and several different technology solutions have been tested [107–109].

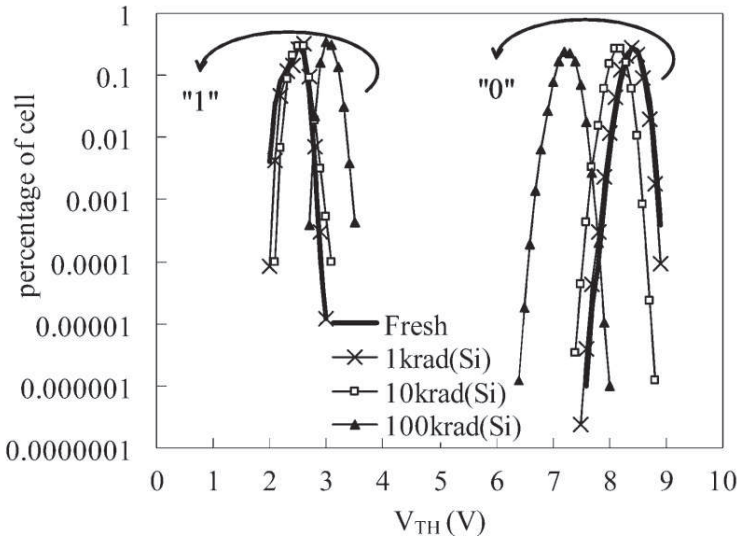

Figure 6-7: Effect of the radiation on the threshold voltage of a flash memory device [106].

6.1.3 Implementation and pratical issues

The sensor tested in this work has been developed by IC-Malaga and it is formed by two parts: the transducer and the reading circuit. The transducer is an N-channel transistor with the floating poly silicon gate that has a large extension over the field oxide Figure 6-8. Positive charges can be placed on the FG prior to the irradiation through the injection electrode. To protect the FG from external electrostatic fields, the entire sensor is overlapped by an upper layer of metal connected to ground, which serves as a shield, Figure 6-9.

Being the floating gate voltage read with an N-MOS, the poly–silicon floating gate is charged with holes and connected to the gate of the reading MOS in order to create a conductive channel. The three mechanisms, previously discussed, play a role in the dosimeter response. The migration of the radiation–induced charges within the oxide which surrounds the floating gate into the floating gate itself, by directly discharging it, is the principal effect on which the sensor is based. The holes stored in the floating gate which are emitted from the floating gate if they acquire enough energy from the incoming radiation (photo–emission) and the holes trapped in the oxide are unwanted, side effects. It will be discussed later in the chapter that the photo–emitted holes effect is negligible.

One has to noticed that, the trapped charges density in the oxide is low, when the

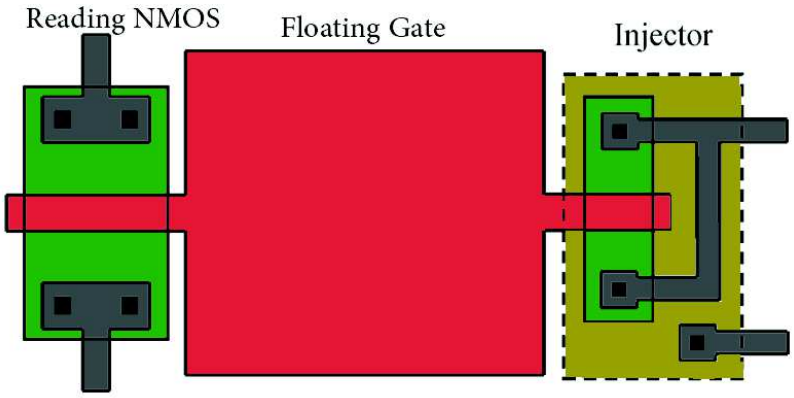

Figure 6-8: Layout of the floating gate dosimeter. On the left side the reading NMOS is depicted while on the right side the injector.

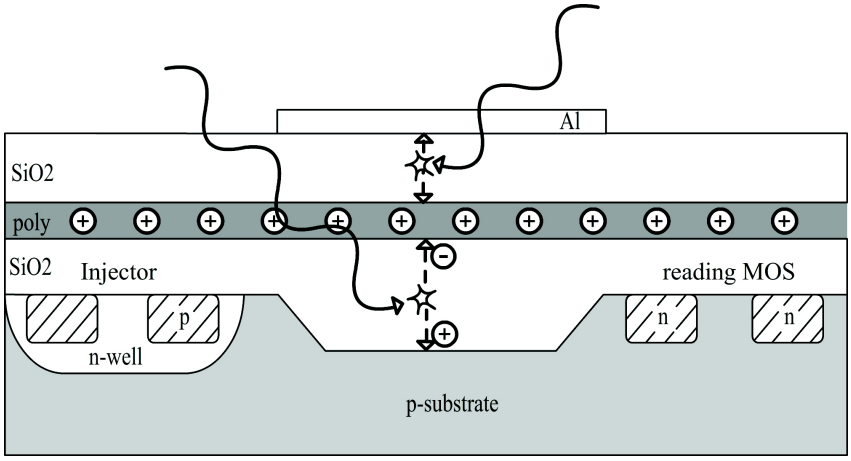

Figure 6-9: Schematic structure of the FGDOS and its working principle.

oxide is thin, but when the oxide becomes thicker than 50 nm (as is the case of the FGDOS sensor) the effect of the trapped charges becomes to be important, which is undesired in this kind of dosimeter, and it will be discussed in a successive paragraph. The resulting effect of the three phenomena is a shift of the gate–source potential of the reading MOS which modulates the current flowing in the MOS itself.

The reading N-MOS, being polarized in linear mode, transduces the gate potential, (i.e. the FG potential) in a current output, which varies with the received dose. The MOS current variation is then converted by an oscillator, embedded in the sensor's chip, in a square wave. The variation of the current results in a frequency variation of the output square wave. To retrieve the information on the dose, it is necessary to count the number of pulses in a given time window. This solution allows to easily

interface the sensor with an external micro–controller or an FPGA. Moreover, the reading algorithm consists of a counter and can also be embedded in a small FPGA.

When the frequency gets too low the sensor is recharged. The recharge process, which can also be done during the irradiation, is controlled by the FPGA firmware which decides to inject charges when the output frequency goes below a pre–defined threshold. The recharging process is stopped when the output frequency reaches the desired initial value. The recharge process needs a supply voltage higher than the sensor core voltage (5 V) to initiate the tunneling. Usually, in all the tests carried out a voltage between 18 V and 19 V is used.

The prototype tested can be defined a Sensor System On Chip (SSOC), whose block diagram is depicted in Figure 6-10. The chip contains the sensor described above, a temperature sensor and a digital SPI interface. The SPI interface is a slave interface used to configure, by means of a microcontroller or FPGA, some internal registers of the dosimeter. The internal registers are used, for example, to select the two configuration HIGHSENS or LOWSENS and to read the temperature output.

In fact, in the tested prototype the dimension of the floating gate overlapping the field oxide is selectable with a digital interface to get two capacitors of different sizes and also two different sizes of the reading MOS transistor. The system with the bigger capacitor (and bigger reading MOS) provides a higher sensitivity to measure low dose variation (this configuration is referred as HIGHSENS), while the smaller capacitor (referred as LOWSENS) is more suitable to measure in a field with a high dose rate. The frequency ranges are around $49 - 32$ KHz for the HIGHSENS and $123 - 100$ KHz for the LOWSENS.

The FGDOS presents an advantage with the respect to the RadFet in terms of fabrication; in fact there is no necessity of a custom process to grow a thick oxide; the sensor can be built directly using a standard CMOS technology. Another advantage of the FGDOS is its intrinsic re–usability. Indeed, once the floating gate is de–charged, it can be charged back to its initial potential value. Being the new version of RadMon based on a rad-tol FPGA, the integration of such a sensor is easy because there is no need of a conditioning circuit between the sensor and the FPGA.

6.1.4 FGDOS test setup

Having seen the complexity of the FGDOS, it was necessary to verify the TID robustness as well as the soft and destructive errors cross sections. Moreover, the sensor has to be characterized until the end of its life–time under different irradiation conditions. The Table 6.1 reports the tests carried out to verify the radiation reliability of the sensors and the reading circuits, as well the radiation response of the dosimeter. For

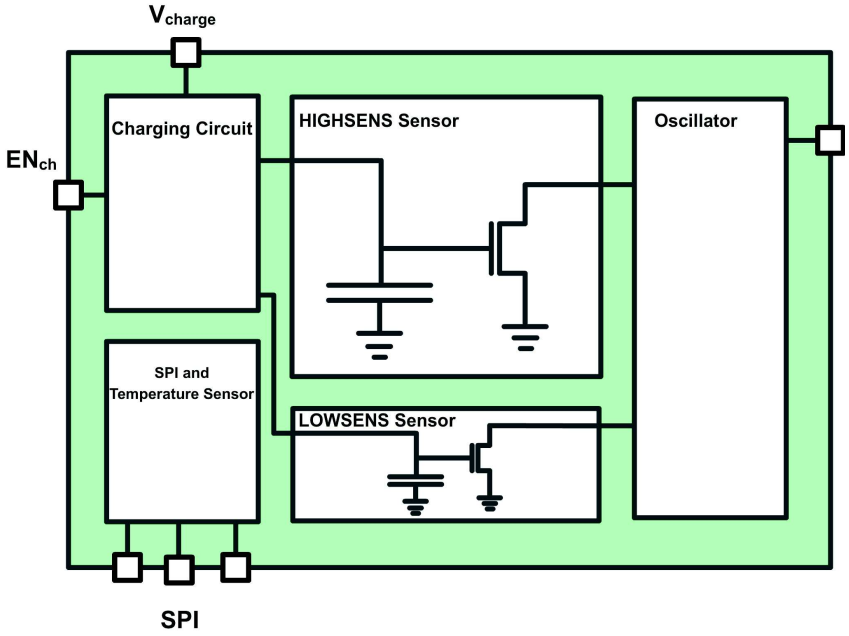

Figure 6-10: Block diagram of the FGDOS Sensor System On Chip.

Table 6.1: Irradiation test conditions for three type of irradiation, ^{60}Co, protons and mixed irradiation field.

	TID Lifetime	Soft SEE	Hard SEE	Sensor Characterization			
				Energy	dose rate	dose	sample to sample
Co60	X				X	X	X
Protons	X	X	X	X	X	X	
H4IRRAD Mixed Field			X			X	

this scope, a modular test setup has been built. The typical complete test setup for the sensor is depicted in Figure 6-11. The supply voltage is fed by three external power supplies (3x Agilent E3648A) controlled via GPIB protocol. They feed the voltage regulators on the auxiliary board and on the tester board. The current consumption of each sensor is measured by means of resistors in series to the regulators that feed the power pins of the sensor. The value of the resistor used was 120 Ω. The voltage drop across the resistor is recorded by a MultiDAQ and it is logged with a PXI acquisition system, controlled via Ethernet. This part of the setup is used only when the current consumption of the sensor has to be monitored. The tester board to read out the FG is an Altera FPGA mounted on a custom board. The tester board is connected to the PC via a USB to Ethernet adapter. The DUT is connected to the tester via a flat cable. We wanted the testbed to be modular to adapt to the needs of the different irradiation campaigns. Indeed, after performing the test on the TID

life–time where the current consumption for each device was a concern, the regulators board and the MultiDaQ were removed. The possibility to have one regulators on the custom made FPGA board made it possible to use just a single dual channel power supply.

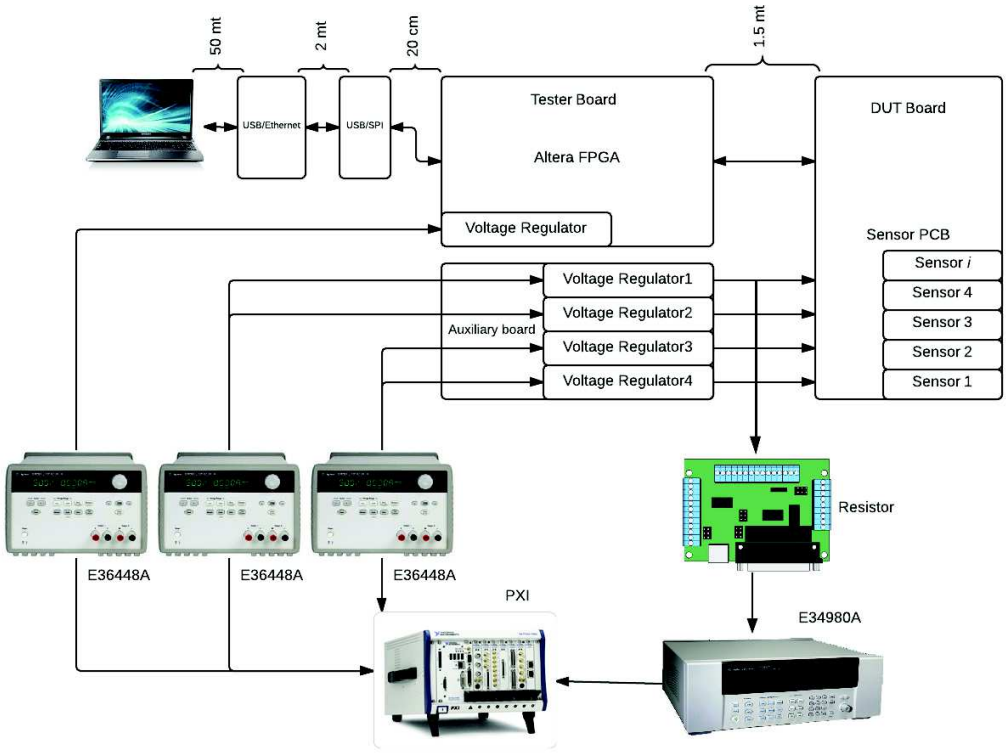

Figure 6-11: Block diagram of the FGDOS modular test setup.

6.1.5 Readout Algorithm

As said before, the output of the sensor is a square wave with its frequency modulated by the received dose. In order to let the sensor work in a well defined region of the reading MOS characteristics (linear region), two values called "threshold" and "target" are set on the readout FPGA. The threshold value is the frequency value at which the floating gate should be recharged back in order not to go out of the linear region of the I_d–V_{gs} curve of the reading MOS. The target value is the frequency value to reach in order to stop the recharge process. An example of raw data from an irradiation of the sensor is depicted in Figure 6-12 for both the configurations HIGHSENS and LOWSENS. The frequency ranges are around $49 - 32$ KHz for the HIGHSENS and $123 - 100$ KHz for the LOWSENS.

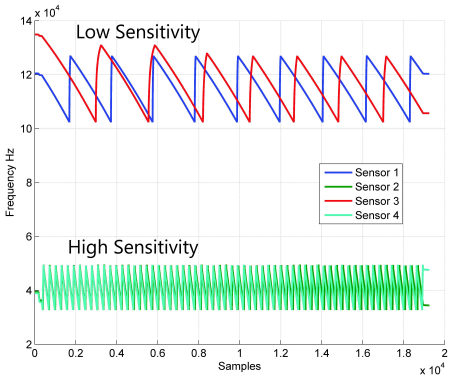

Figure 6-12: Raw data acquired from the sensors.

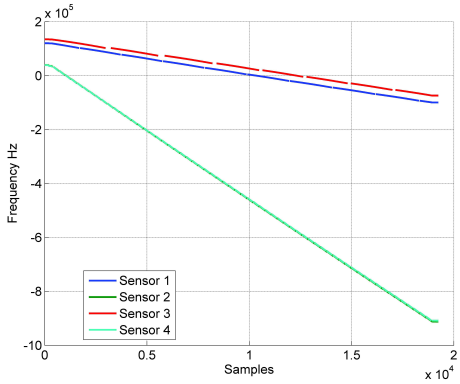

Figure 6-13: Recharge compensation output.

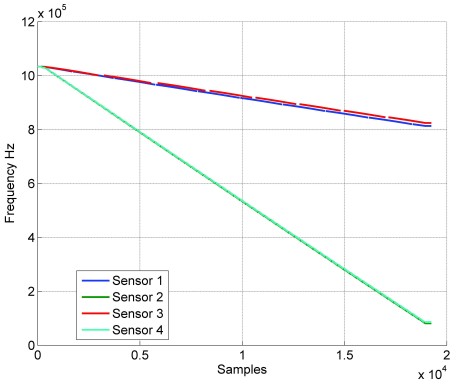

Figure 6-14: Normalization of the data to compare the slope.

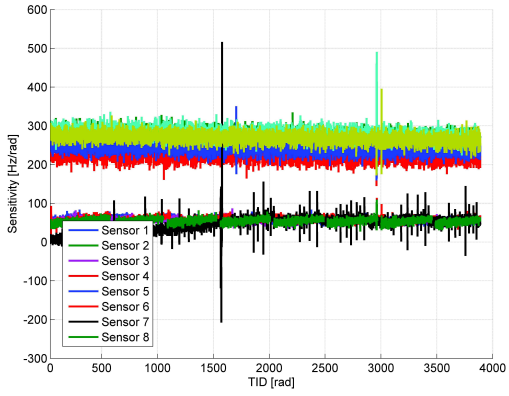

Figure 6-15: Sensitivity for the irradiated sensors. The spikes remaining are the ones that the algorithm was not able to remove.

A post–processing analysis is necessary to retrieve the correct information on the cumulated TID. A block diagram of the algorithm is depicted in Figure 6-16. The first block treats the part of raw data related to the recharge process. The "recharge compensation" removes the samples acquired during the recharge process from the data in order to analyze the shift of the frequency (Figure 6-13). The data of the recharge process are ignored in the analysis phase. The frequency shift reaches negative value, as can be seen in Figure 6-13. This is an artifact of the recharge compensation processing. Thus, the successive step is to make positive the frequency shift. Moreover, all the output frequencies are shifted in such a way that

they have the same initial frequency to better compare the slope of the sensors. The maximum frequency variation is taken as a reference to make this normalization. The result of these two processes is reported in Figure 6-14. Some spikes appear on the output frequency. To remove those spikes from the data of the irradiation phase, a detection algorithm has been implemented. For the characterization of the sensors, the sensitivity, expressed as the ratio between the variation of the output frequency and the dose (Figure 6-15), is studied.

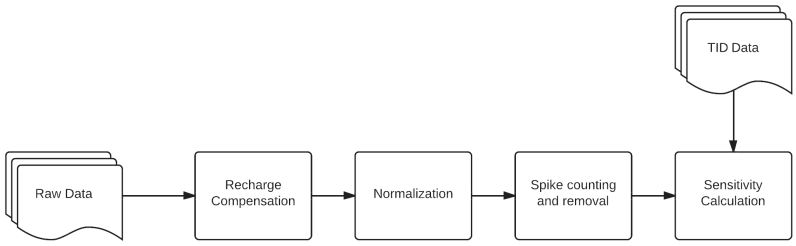

Figure 6-16: Block diagram of the step necessary for the continuous reading of the FGDOS sensor.

6.2 Radiation test results

In this section the main results from the irradiation in different reference fields of main importance for the CERN environment are presented. The floating gate was tested for the first time at CERN in the H4IRRAD facility, a CERN mixed irradiation facility. The other tests have been performed with a ^{60}Co source and with a protons beam at the PSI facility.

6.2.1 Radiation test at H4IRRAD

The test at H4IRRAD (see Chapter 2) was carried out on a first version of the prototype, which was from a different batch with the respect to the one tested afterwards. The setup was also slightly different from the one presented in the previous section (Figure 6-11). One of the main concerns was the use of long cable to connect the sensors from the irradiation zone up to the control zone (30 meter long), which induced noise on the output signal.

The main objective of the campaign was to verify the working principle of the FGDOS in a mixed field. Indeed the sensor was not yet calibrated at that time and thus, a cross calibration was done in post-analysis by exploiting the results of the

RadFets placed very close to the installation location of the FGDOS (Figure 6-17). Another important point was to asses the robustness of the prototype to destructive events such as Single Events Latchup.

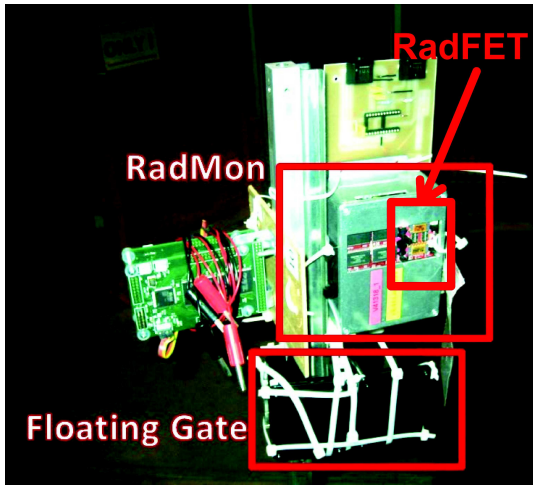

Figure 6-17: H4IRRAD installation. RadMon on top and Floating gate below.

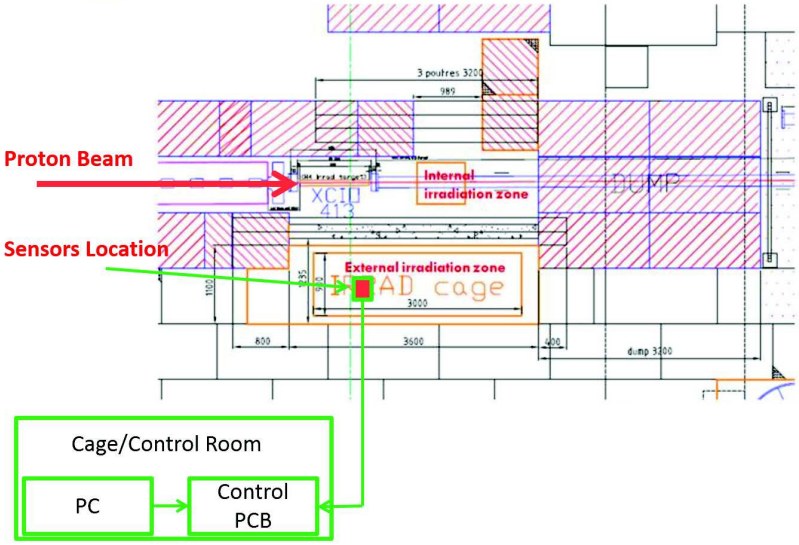

Figure 6-18: H4IRRAD installation. FGDOS sensors were put in the external zone.

Two sensors configured in HIGHSENS mode were placed in an area of H4IRRAD where the dose rate was around 10 times less with respect to internal zone (see Chapter 2) as depicted in Figure 6-18. The irradiation lasted 20 days. The slot was divided in two parts with two different intensity periods as depicted in the Figures 6-19, 6-20; in

the first period the average protons on target (POT) was 2×10^8, while in the second one the average POT was around 4×10^9.

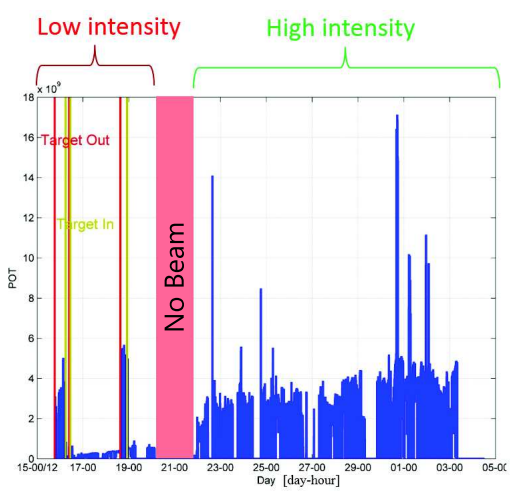

Figure 6-19: Proton on target per second for the H4IRRAD test (blue line). The two intensity periods are evidenced.

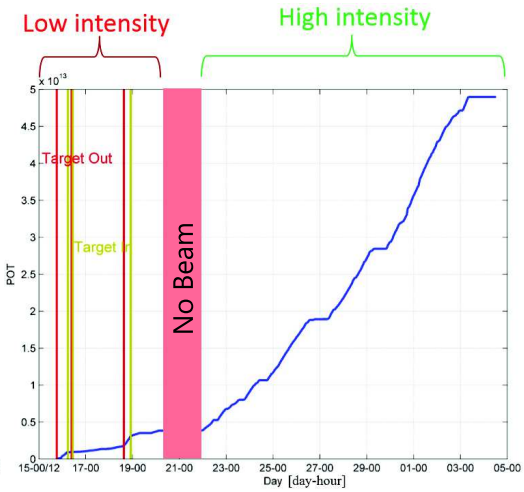

Figure 6-20: Cumulative number of protons on target for the H4IRRAD test (blue line).

The measurements performed in H4IRRAD in the low intensity period are depicted in Figure 6-21. The measurements are compared with the data of the RadFets mounted on the RadMon V5 (400 nm and 100 nm). The TID was too low to be measured with the RadFet 100 nm which has a resolution of only 250 rad (considering that the RadMon V5 has a 12 bit ADC with a resolution of 2.5 mV). Thus the comparision is performed only with the RadFet 400 nm with bias voltage at 0 V. As depicted in Figure 6-21, both the sensors in HIGSENS configuration follow nicely the RadFet 400 nm (low intensity period). In the high intensity slot the sensors still worked, however the difference between the response of the two sensors increases with the accumulated dose, reaching a percentage difference of 10% at the end of the irradiation period, as depicted in Figure 6-22. In the same picture, it is also highlighted the annealing of the RadFet when there was no beam; conversely the FGDOS sensors did not show any decrease of the output frequency.

The sensitivity in Hz/rad has been calculated as a function of the dose retrieved by the RadFet 400 nm (considered as a reference) for both the sensors. As depicted in Figure 6-23, the average sensitivity in the low sensitivity period is only 6% less than the one in the high intensity period. This mismatch could be due to the different dose rate at which the sensors are exposed in the two periods. The average sensitivity,

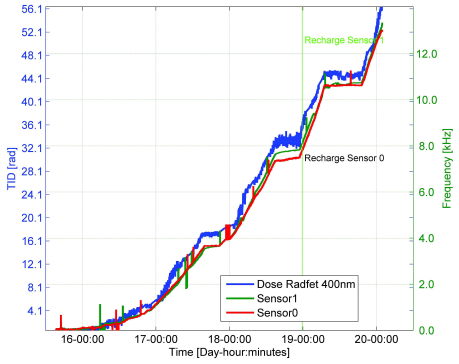

Figure 6-21: Response of the two FGDOS sensors compared with the one of the 400 nm RadFet in the low intensity period. The green lines indicates when the first recharge process happens.

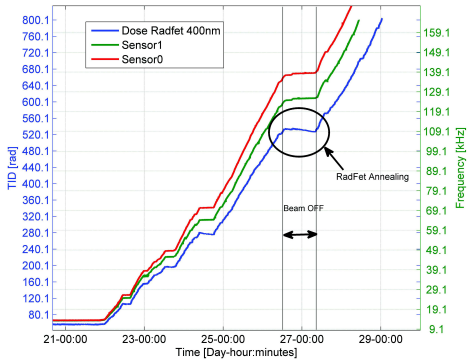

Figure 6-22: Response of the two FGDOS sensors compared with the one of the 400 nm RadFet in the High intensity period. The annealing of the RadFet is highlighted.

calculated on the last day of the low intensity and on the full period of the high intensity periods, considering the data of both the sensors, is around 243 Hz/rad with a standard deviation (1σ) of 9.9 Hz, representing a variation of 4%. The noise level measured on the output frequency was around 60 Hz, due to the long cable between the sensor and the readout circuitry. Thus, the minimum resolution we could achieve with this setup was around 247 mrad.

The values here reported cannot be used to calibrate the sensors because of the complex radiation environment of H4IRRAD. Moreover, the 400 nm RadFet was used as a reference but we know that it underestimates the TID by 40% [83]. Despite of that, we proved the working principle of the sensor which was the main goal of this experiment. Furthermore, the sensors and its embedded reading circuitry did not suffer any destructive events up to a fluence of $4 \times 10^9 HEH/cm^2$. On this basis, the sensor has been characterized to get a proper calibration curve with ^{60}Co source and with protons at different energies.

6.2.2 Radiation test at the USC Facility with ^{60}Co

The sensors were tested at the Universidade de Santiago de Compostela, by using a 5.8 kCi ^{60}Co source. The tests have been made at various distances from the source to achieve different dose rates ranging from 12 rad/h to 270 rad/h.

As stated in the Chapter 2, the reference dose was given by the facility by means of a therapy level ionization chamber which measures the dose rate. By means of a

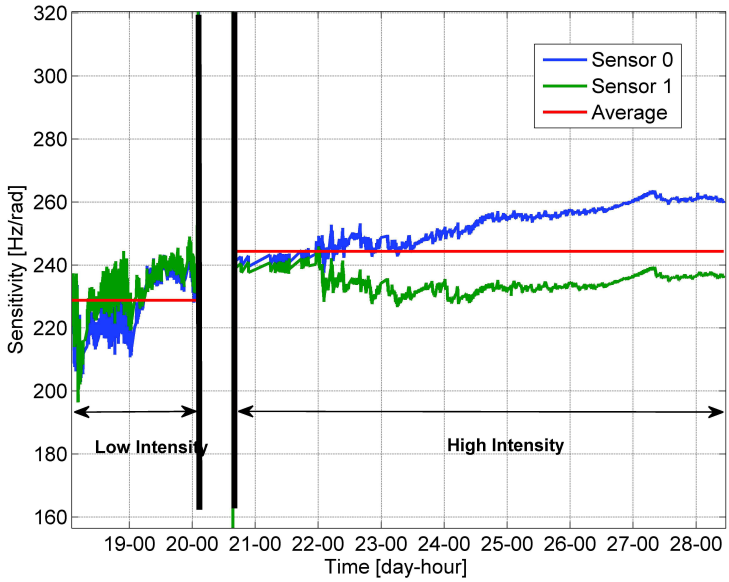

Figure 6-23: Sensitivity as function of the time for the two sensors tested in H4IRRAD. Both the low intensity period and high intensity periods are shown.

Labview software, the ionizing radiation is integrated over time and the dose in silicon is provided with an accuracy of 3%. The accuracy of the calibration was cross checked with the RadFets placed few centimeters away from the FGDOS. The temperature of the room was stable and maintained for the entire test at 20 ± 0.1 °C.

The main purpose of the gamma irradiation was to calibrate the sensor retrieving the output frequency as a function of the TID. Moreover, the dose rate effects, the TID tolerance (life–time) of the sensors and the sample to sample variation are assessed. In the Table 6.2 the test plan for the USC irradiation is reported. The first ten runs were carried out at different dose rates and for each dose rate four new sensors are added. Two of them in the HIGHSENS and two in the LOWSENS configuration. The runs from 11 to 21 were carried out to cumulate TID on the samples in order to verify the long-term TID effect and the sensor TID lifetime. In the Table 6.3 the summary of the sensitivities measured in the first 10 runs are reported. The first three runs were made at very low dose rate 12 rad/h. The dose rate of the successive four runs was 87 rad/h and then 270 rad/h. The percentage differences of the sensitivity with respect to the first run are reported in the columns $Diff$. The effect of the dose rate seems to be inverted for the HIGHSENS and the LOWSENS configuration; for the former, the sensitivity increases with the dose rate, while for the latter the sensitivity decreases of around $20 - 28$ % from 13 rad/h to 270 rad/h.

Table 6.2: Test plan for the ^{60}Co irradiation.

Run	Samples	Dose Rate	TID per Run
		[rad/h]	rad
1	1-2	13	13
2	1-2	13	13
3	1-2	13	19
4	1-2-3-4-5-6	86.7	1065
5	1-2-3-4-5-6	86.7	89
6	1-2-3-4-5-6	86.7	91
7	1-2-3-4-5-6	86.7	215
8	1-2-3-4-5-6-7-8-9-10	259	3888
9	1-2-3-4-5-6-7-8-9-10	269	278
10	1-2-3-4-5-6-7-8-9-10	269	273
11	1-2-3-4-5-6-7-8-9-10	269.2	677
12	1-2-3-4-5-6-7-8-9-10	269.2	4316
13	1-2-3-4-5-6-7-8-9-10	269.2	291
14	1-2-3-4-5-6-7-8-9-10	269.2	273
15	1-2-3-4-5-6-7-8-9-10	269.2	408
16	1-2-3-4-5-6-7-8-9-10	269.2	4200
18	1-2-3-4-5-6-7-8-9-10	269.2	2885
19	1-2-3-4-5-6-7-8-9-10	269.2	2778
20	1-2-3-4-5-6-7-8-9-10	269.2	4664
21	1-2-3-4-5-6-7-8-9-10	269.2	2034
22	11-12-13-14-15	2091	1010
23	16-17-18-19-20	2094	1012

Table 6.3: Dose rate dependency of the FGDOS sensitivity for HIGHSENS and LOWSENS configuration.

		LOWSENS		HIGHSENS	
Run	Dose Rate $[\frac{rad}{h}]$	Sensitivity $[\frac{Hz}{rad}]$	Diff. %	Sensitivity $[\frac{Hz}{rad}]$	Diff. %
1	13.0	46.3	0.0	335.5	0.0
2	13.0	44.8	-3.2	321.9	-4.1
3	13.0	50.3	8.7	323.1	-3.7
4	86.7	45.4	-1.9	308.2	-5.7
5	86.7	45.1	-2.6	298.1	-8.8
6	86.7	48.7	5.2	290.9	-11.0
7	86.7	52.4	13.3	297.8	-8.9
8	259.2	49.5	21.1	229.1	-29.9
9	269.2	57.0	20.8	262.8	-19.6
10	269.2	59.1	28.7	260.7	-20.2

In Figure 6-24 the dependency of the sensitivity on the TID is showed for the HIGHSENS and LOWSENS configuration for a test done at 270 rad/h. A linear fit was used to extrapolate the rate at which the sensitivity decrease. The sensitivity decreases at a rate of 9% each 10 krad(Si) for both the configurations. All the sensors stop working properly around 28 krad(Si).

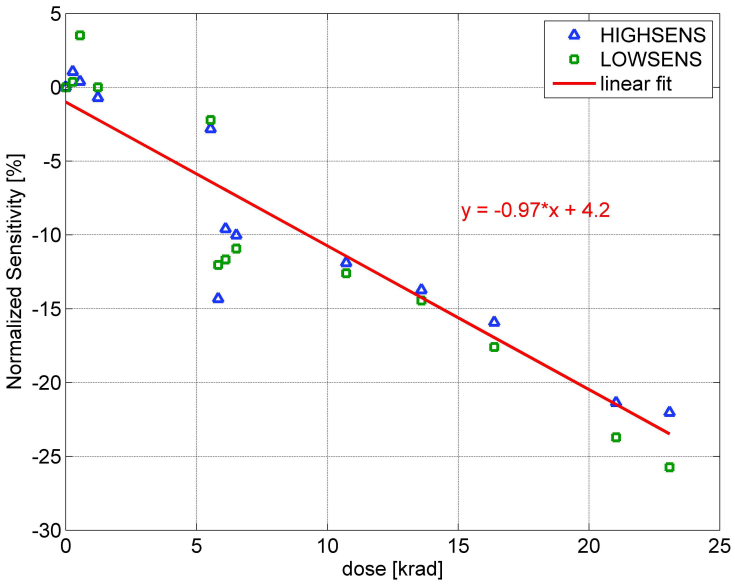

Figure 6-24: Dependency of the sensitivity on the TID for the LOWSENS and HIGHSENS sensors, expressed as percentage difference with respect to the initial sensitivity. Those tests are carried out at a constant dose rate of 270 rad/h in ^{60}Co. The drop of sensitivity around 7 krad(Si) could be due to a variation of the polarization of the readout circuitry due to the TID.

Two runs (run 22–23) have been planned in order to verify the spread among the sensors from the same lot (Table 6.2). A dose rate of 2000 rad/h has been chosen and the cumulated TID is around 1 krad in order not to be sensitive to the long–term TID effect. Five new sensors for each configuration HIGHSENS and LOWSENS have been tested in a single irradiation run. The mean and the standard deviation of the sensitivity of the sensor is evaluated during all the run. Then, the average sensitivity of the sensors is given in Table 6.4. The spread, calculated as ratio of the standard deviation over the the mean, is 2% and 7% for the HIGHSENS and for the LOWSENS respectively.

Table 6.4: Spread among components five sensors for each configuration irradiated in a single irradiation run.

Run	Dose rate $[\frac{rad}{h}]$	TID [rad]	mean $[\frac{Hz}{rad}]$	std $[\frac{Hz}{rad}]$	Spread $[\frac{\sigma}{\mu}]$ %
22	2091	1010.2	320.9	5.7	1.8
23	2094	1012	61.6	4.2	6.8

Table 6.5: Proton test plan.

Run	**Sensors**	**Energy [MeV]**	**Fluence**	**TID [rad]**	**Dose rate [rad/h]**
1	1-2	230	1.87×10^{10}	1.00×10^{3}	530
2	2-3	101.4	1.07×10^{10}	1.00×10^{3}	592
3	3-4	60.88	4.04×10^{9}	5.48×10^{2}	706
4	1-2	230	8.00×10^{10}	4.27×10^{3}	31966
5	1-2	230	7.24×10^{10}	3.86×10^{3}	31896
6	1-2	230	6.71×10^{10}	3.58×10^{3}	29568
7	1-2	230	6.43×10^{10}	3.43×10^{3}	31926
8	1-2	230	9.37×10^{10}	5.00×10^{3}	31928
9	1-2	230	5.21×10^{10}	2.78×10^{2}	14937
10	1-2	230	9.37×10^{10}	5.00×10^{3}	31972
11	1-2	230	8.32×10^{10}	4.44×10^{3}	31953
12	3-4	230	1.88×10^{10}	1.00×10^{3}	6670
13	3-4	230	1.88×10^{10}	1.00×10^{3}	13423

6.2.3 Proton Irradiation at PSI

The aim of the first three runs was to understand the dependency of the FGDOS response on the proton energy. Three energies have been selected 60 MeV, 100 MeV and 230 MeV. The sensitivities for different proton energies are reported in Table 6.6. For each energy two new sensors were tested to start with a fresh device. For each run only 1 krad of TID was cumulated because we do not want to mix the TID effects with the energy dependency. Moreover, we tested the device using the same dose rate for each energy. The sensitivity for both the configurations decreases as the incoming beam energy goes lower. This effect is due to the charge yield that depends on the type of the incoming particles and its energy. A deeper analysis of this phenomenon is done in the Section 6.3.

A second test was carried out in order to assess the causes of the long–term TID effect on the sensitivity with protons at 230 MeV. The results in Table 6.7 show a decrease of the sensitivity with respect to the accumulated TID as observed with the

Table 6.6: Sensitivity dependency on the proton energy for LOWSENS and HIGHSENS configurations.

		LOWSENS		HIGHSENS	
Energy MeV	Dose Rate rad/h	Sensitivity Hz/rad	Diff. %	Sensitivity Hz/rad	Diff. %
230	530	76	0	358.7	0
101	530	65.2	-14	288.7	-19
60	530	50.9	-33	238.9	-33

^{60}Co gamma measurements. A typical curve of the sensitivity as function of the TID is depicted in Figure 6-25.

Table 6.7: Sensitivity variation with respect to the TID for the LOWSENS configuration [Energy: 230 MeV]

TID	Difference
[krad(Si)]	%
1	0
4.3	-13
7	-23
11	-21.6
19	-30

The decrease of sensitivity is due to the trapping of charges in the field oxide of the floating gate capacitor. To verify this statement a long run was performed up to 10 krad measuring the sensitivity at the beginning and at the end of the irradiation. Afterwards, an isochronal annealing up to 300 °C was performed on the irradiated samples [110]. The isochronal annealing effect can be studied only when the sensor is re–irradiated because there are no electrical parameters that give indication on the state of the field oxide. Thus, the samples were again irradiated from 10 krad to 16 krad to re-measure the sensitivity, which resulted to be increased by the isochronal annealing, as reported in Table 6.8.

The sensors stopped working properly around 20 krad(Si). Before the end–life an increase of current consumption was noticed. The nominal power consumption is around 2.5 mA and 1 mA for the HIGHSENS and LOWSENS configurations respectively. The tests to verify the TID at which the sensors stop working were done only on the LOWSENS configuration since the dose–rate was high in the run 4 to 10 (around 30 krad).

In the Figure 6-26 the current for two LOWSENS sensors is shown with the TID

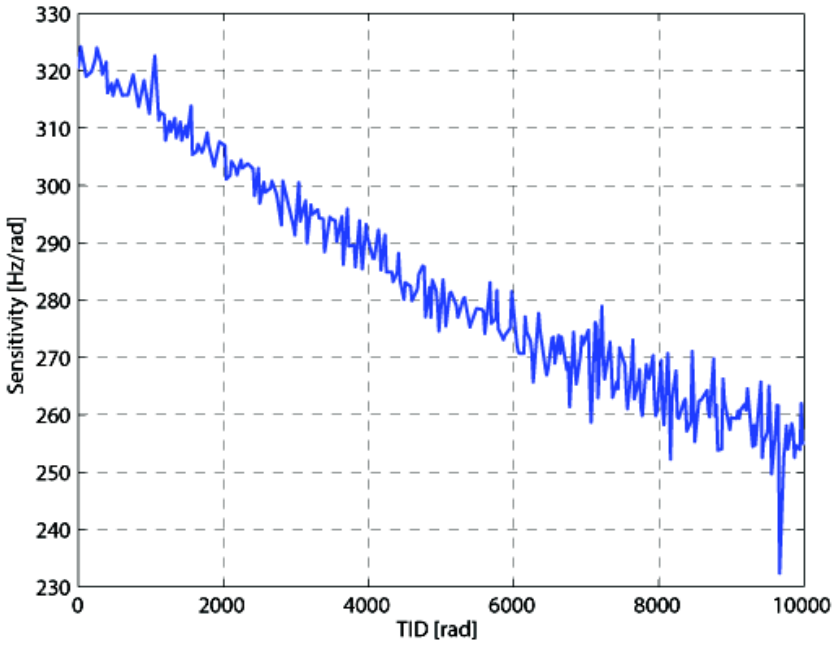

Figure 6-25: Sensitivity as function of the TID cumulated for a HIGHSENS configuration.

expressed in krad. Starting from 10 krad the current consumption starts to increase reaching around 9 mA at 20 krad. A small difference of around 1 mA between the two sensors can be noticed. The increase of power consumption was not an issue for the proton tests since the voltage regulators are able to supply this amount of current up to 25 krad.

The proton test also allowed assessing the Single Events susceptibility of the FGDOS. The test focused on both destructive (Single Event LatchUp) and non–destructive events. The Latch–up test was carried out with a 230 MeV protons up to a fluence of 5.60×10^{11} and no events were recorded. Non–destructive Single Events

Table 6.8: Irradiation and post isochronal annealing results.

	HIGHSENS			LOWSENS		
TID krad	Start Hz/rad	End Hz/rad	%	Start Hz/rad	End Hz/rad	%
0-10	320	254	-20	59.6	47.7	-20
After isochronal annealing at 300 °C						
10-15.7	281	-	-12	51.9	-	-12

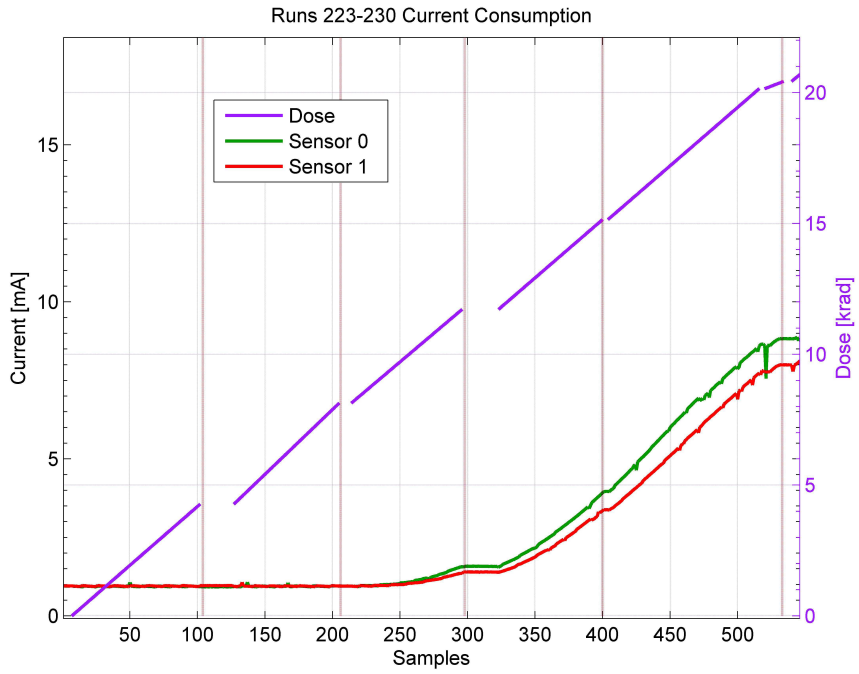

Figure 6-26: Current consumption of two sensors up to 20 krad. Current increase up to 9 mA at 20 krad.

have been recorded on the SPI digital registers storing the temperature value of the sensor embedded in the FGDOS. The spikes that occasionally appear on the output frequency of the sensor are considered as Single Events too. If one counts those events (50 in total), the cross sections of the registers can be estimated as $7 \times 10^{-11} cm^2$ with 1σ uncertainty of 15%. Nonetheless, those soft single events are not an issue since the registers are refreshed at each reading cycle.

The tests with a 230 MeV proton beam have been carried out also at 3 different dose rates 530 rad/h, 13 krad/h and 30 krad/h. It has been verified that the HIGHSENS configuration cannot work as from 13 krad/h, because the decharge of the floating gate becomes so fast that the sensor is continuously in recharge mode. For this reason the tests at 13 and 30 krad/h were carried out only on the LOWSENS configuration. The recharging process was normally done applying 18 V on the injector; however, during the irradiation at the highest dose rate (30 krad/h) the recharge voltage was incremented to 19 V to speed up the process. The results show a decrease of the sensitivity for the LOWSENS configuration of around 30 % due to the dose rate variation from 500 rad/h to 30 krad/h (Table 6.9).

A second test campaign was carried out to assess the dose rate effect also on the

Table 6.9: Sensitivity dependence on the dose rate for the LOWSENS configuration during proton irradiation.

LOWSENS		
Dose Rate [rad/h]	Sensitivity Hz/rad	Percentage %
529	76	0
13423	65.9	-13
31965	55.4	-27

HIGHSENS configuration. The dose rates are lower than those chosen in the previous test campaign and they are around 500 rad/h 2500 rad/h and 6000 rad/h (Table 6.10). All the tests have been carried out at 230 MeV. The important runs to look at are the Run 44,45 and 46, for which the irradiated sensors were completely new. Thus, there is no long term TID effect affecting them. There is a clear effect of the dose rate on the sensor sensitivity. The sensor sensitivity decreases up to 30 % going from a dose rate of 500 rad/h, taken as reference, to around 7500 rad/h. The results are confirmed also re-irradiating the same components in different dose rate conditions: Runs 47 to 51. In the Run 51 the sensor configured in Low Sensitivity mode was not working correctly and the value of sensitivity is lower than the one expected. These results confirm what already seen for the LOWSENS at higher dose rate. The two test campaigns showed an agreement of about 6% for the measurements of the sensitivity of the LOWSENS configuration at 500 rad/h.

Table 6.10: Sensitivity of the sensor for each run, highlighting the dose rate effects. The mean and the standard deviation are calculated for each sensor. *In the run 51 the sensor in Low Sensitivity configuration has a problem.

					HIGHSENS			LOWSENS		
Run	DUT	Energy	TID [rad]	Dose Rate [rad/h]	mean [Hz/rad]	std [Hz/rad]	% %	mean [Hz/rad]	std [Hz/rad]	% %
44	370 371	230	250	526	388.5	10.2	0	84.7	6.2	0
49	370 371	230	200.2	5859	301.9	4.3	-29	61	3.8	-39
50	370 371	230	150.7	2547	309.1	4.3	-26	63.6	2.4	-33
51	370 371	230	100.1	526	392.6	8.9	1	69.0*	8.6	-23*
45	372 373	230	250.4	2546	307.9	5	-26	69.3	7.2	-22
46	374 375	230	251.1	7860	296.7	3.6	-31	62.7	3.6	-35
47	374 375	230	100.1	515	375.5	9.7	-3	83.7	3.8	-1

6.3 FGDOS model and charge yield measurements

We have discussed about the different phenomena that cause a voltage drift on the FGDOS sensor. The most significant ones are the generation of electron-hole pairs which neutralize the FG charge and the charge trapping in the SiO_2. The phenomena of electrons (or holes) escaping from the floating gate, also called photo–emission [105], has a marginal effect on the FG voltage. The amount of electrons photoemissed is a function of the oxide electric field. For low–electric field $<< 0.5MV/cm$, as in our case, the percentage of charge yield due to photoemissed electrons(or holes) is nearly equal zero [106].

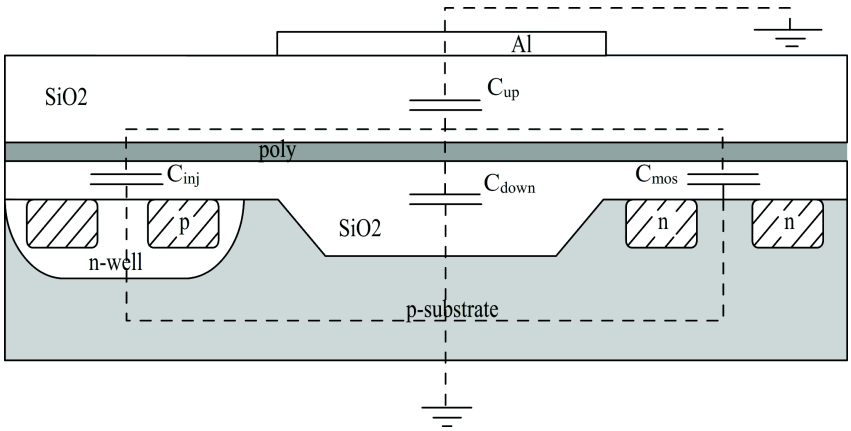

Figure 6-27: Schematic structure of the FGDOS with the capacitance model.

From the simple equation of a MOS capacitor we want to extrapolate the main parameters to model the FGDOS sensor considering the phenomenon of the electron-hole pairs decharing the floating gate. The ionizing radiation can be treated as a current flowing in the MOS capacitor as shown in (6.3):

$$i(t) = \frac{dQ_{coll}(t)}{dt} = -C_{sum}\frac{dV_{FG(t)}}{dt} \tag{6.3}$$

where C_{sum} is the sum of the capacitance associated with the floating gate, the reading MOS and the injector, $C_{up}, C_{down}, C_{mos}, C_{inj}$ (Figure 6-27). The terms V_{FG} is the floating gate potential measured by the reading MOS. The charge Q_{coll} collected during the exposure can be rewritten as:

$$Q_{coll} = g_0 f(En, Fi) D \sum_{1<i<sens} A_i t_i \tag{6.4}$$

The charge density g_0 created in the oxide by ionizing radiation has been measured

by Benedetto and Boesh [58] and is around $1.3 \times 10^{-6} C/cm^3/rad$. The term D is the dose received in rad, while the terms $f(En, Fi)$ is the fraction yield and weights the amount of charge that can escape recombination; the fraction yield is a function of the electric field Fi, the type of the incoming particles and its associated energy En. The charge collection depends on the volumes $\sum_{1<i<sens} A_i t_i$ where $sens$ is the number of sensitive volume present in the sensor. In the FGDOS the volume covered by the floating gate over the field oxide is bigger than the one represented by the reading MOS and the injector thus the equation (6.4) can be rewritten as:

$$Q_{coll} = g_0 f(En, Fi) D(t) A_{FG} [t_{down} + t_{up}] \tag{6.5}$$

The collection volume consists of two parts, the first is given by the area of the floating gate over the field oxide A_{FG} multiplied by the thickness (t_{down}) of the oxide from the substrate to the poly gate and the second one by A_{FG} multiplied by the thickness (t_{up}) of the oxide from the poly gate up to the aluminium shielding on the Metal 1 layer (Figure 6-28).

The floating gate potential can be rewritten as:

$$dV_{FG} = -\frac{g_0 f(En) A_{FG} [t_{down} + t_{up}] dD}{C_{sum}} \tag{6.6}$$

In the equation (6.6) the charge yield is considered independent on the electric field. This assumption is true for the FGDOS sensor because the variation of the floating gate potential is limited to a few hundreds of mV around the floating gate potential of around 4 V. Thus, the electric field over the oxide can be assumed as constant and equal to 0.06 MV/cm (low field). Integrating equation (6.6) and normalizing it as a function of the dose increment, we get:

$$\frac{V_{FG0} - V_{FG1}}{D_0 - D_1} = -\frac{g_0 f(En) A_{FG} [t_{down} + t_{up}]}{C_{sum}} \tag{6.7}$$

The equation (6.7) expresses the sensitivity of the sensor as V/rad which results to be $-33 \times f(En)$ mV/rad for the tested FGDOS prototype. In the last equation, the sensitivity is directly proportional to the area of the floating gate but inversely proportional to the sum of the capacitances. Since, the capacitance is directly proportional to the area, and the area of the injector and the reading MOS are very small compared to the one of the floating gate (C_{sum} is dominated by the C_{up} and C_{down}), equation (6.7) is not a function of the area of the floating gate. As a consequence, the sensitivity value of $-33 f(En)$ mV/rad is the same for both the LOWSENS and HIGHSENS configurations, and the increment of sensitivity between the two con-

figurations is only due to the trans–conductance of the reading MOS. Indeed, the HIGHSENS has a bigger reading MOS than the LOWSENS in order to achieve a higher sensitivity. Knowing the relation between the floating gate voltage and the output frequency (by means of a HSPICE simulation), the ratio between the variation of the gate potential and the dose is evaluated using the results of the test campaigns. These results are inserted in the analytic model to get the charge yield factor $f(En)$ for different types of particles and different energies.

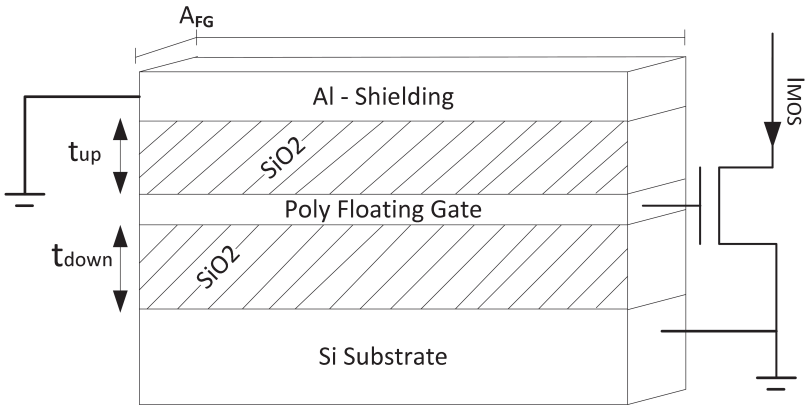

Figure 6-28: Schematic structure of the FGDOS without the injector.

The FGDOS structure is a good candidate to measure the charge yield at very low electric field at room temperature. Usually to measure the charge yield at low electric field, the tests are carried at low temperatures [111] because the hole transport is practically freezed but the work [112] was the first to demonstrate that temperature had a strong influence on the charge yield at low electric fields. The FGDOS structure has some advantages with respect to the usual MOS transistor; since the sensor is based on the annihilation of the holes in the floating gate, the key mechanism is the transport of the electrons to the floating gate, which is faster than the hole one and not so affected by the trapping in the oxide. For those reasons the decharging of the FG is a convenient way to measure the amount of charges that escape the initial recombination at room temperature.

The values of sensitivity in mV/rad found with the measurements ans with the help of HSPICE are matched with the theoretical one ($-33f(En)mV/rad$) to calculate the charge yield $f(En)$ parameter for protons at different energies and for the ^{60}Co gamma (Table 6.11) by using the equation 6.7. Both the values for the gamma and the proton irradiation are consistent with the ones found in [113]. The discrepancy of the $f(En)$ values for the HIGHSENS with respect to the LOWSENS configuration is due to uncertainty of the HSPICE simulation. The uncertainty on the measurements of the

charge yield can be estimated to around 20% and it depends on different factors, such as the sensors uncertainty, the accumulated TID, which was kept as low as possible to avoid any synergistic TID effects on the measurement, and the dose uncertainty of the facility.

Table 6.11: Charge yield at different proton energies and for ^{60}Co gamma for an electric field of 0.06 MV/cm.

	LOWSENS		HIGHSENS	
Energy MeV	Sensitivity mV/rad	$f(En)$	Sensitivity mV/rad	$f(En)$
230	2.37	0.07	2.78	0.08
101	2.02	0.06	2.23	0.07
60	1.62	0.05	1.85	0.06
^{60}Co	2.21	0.07	2.55	0.08

6.4 Summary

The physics behind the floating gate structure and the working principle of the floating gate dosimenter have been analyzed in this Chapter. The basic mechanism on which the sensor is based is the annihilation of the stored charges in the floating gate due to the radiation–induced charges in the SiO_2 surrounding the FG. The consequence of the floating gate discharging is a variation of the threshold voltage of the reading MOSFET. In the FGDOS sensor, the variation of V_{th} is converted in a frequency shift by means of an oscillator embedded in the same IC.

The sensor is defined as a SSOC because it has several configuration and several output that can be monitored. The complex system needed a sophisticated test setup to accommodate all the type of needed measurements. Moreover, because of its nature of mixed–signal chip (it embeds analog and digital part) a complete characterization for destructive and non–destructive effect was needed.

The sensor has been tested in ^{60}Co gamma field, proton beam and in a mixed radiation field facility at CERN. The first test was carried out in H4IRRAD, a mixed radiation field facility at CERN. The tests mainly focused on the verification of the working principle and the characterization of the sensor for destructive events in an environment very close to the one in which it might work. The sensor was cross–calibrated with a RadFet 400 nm and a sensitivity of 240 Hz/rad was measured. It has been shown that, despite the RadFet, it does not suffer of annealing, at least at very low TID. The test was not intended to be a calibration but it gave us a good

feedback on the possible use of the sensor in the RadMon system. The second step was to test the sensor with ^{60}Co gamma and protons. The tests were carried out to verify the long–term TID effect, the TID lifetime, the dose rate effect and finally the spread in the lot. The TID life–time resulted to be around 28 krad(Si) and 20 krad(Si) for the gamma and the proton irradiation, respectively. This discrepancy could be due to the combined effect of total dose and displacement damage caused by the protons. In a future prototype some mitigation techniques applied directly in the ASIC design, such as enclosed gate layout (ELT) of MOS transistors, will be applied to be more radiation tolerant.

One still open question is the change of the sensor sensitivity within 30% with the dose rate; to better understand this phenomenon other tests will be carried out in ^{60}Co, matching the same dose rates of the proton tests.

The proton tests, which were performed also to verify the SEE susceptibility of the sensor, showed that the chip is SEL free up to a fluence of 5.60×10^{11} of 230 MeV protons. The non-destructive cross sections of the output of the sensor is $7 \times 10^{-11} cm^2$. Nonetheless, those events are not an issue since the registers are refreshed at each reading cycle of 2 seconds.

An analytical model of the sensor has been presented and the theoretical sensitivity for the prototype of FGDOS has been evaluated. The model, which explains the working principle of the sensor, high–lightening the electrical and geometrical parameters affecting the sensor sensitivity, permitted to evaluate the charge yield at low electric field (0.06 MV/cm) with protons at energies ranging from 230 MeV down to 60 MeV and for ^{60}Co, obtaining results which are in good agreement with literature. Above all, this demonstrates that the sensor can be used as a charge yield measurement tool at room temperature for very low electric field.

The sensor could be a good candidate as a dosimeter at CERN due to its linearity and high resolution (around 30 mrad(Si) for HIGHSENS configuration considering 10 Hz of noise) which overcomes the resolution of a 100 nm RadFET (considering the RadMon V6) by a factor bigger than 100. The ease of integration in the actual RadMon system is another good advantage. The uncertainties due to the energy of the incoming particles, an issue also for the RadFETs, remains an uncertainty term to take in consideration when reporting the dose value. In the future a new development and new tests are foreseen to study different floating gate structures and sensors to reduce these uncertainties terms. The dose rate effect is still an open issue to be assessed with more radiation test and new development to understand the physical causes of that phenomenon.

Chapter 7

Conclusions and outlooks

This thesis is devoted to the study and development of the radiation monitoring instrument for the electronic components used in the LHC: the RadMon. The main objective of the RadMon is to measure the distribution and rates of the radiation levels in the LHC and its accelerator chains due to a harsh and unique radiation environment.

This work reports the efforts made to improve the radiation hardness and the accuracy of the RadMon. The precision of the dosimetry has been improved by accurate calibrations of the sensors and the continuous effort to improve the sensitivity and resolution of our system drove the investigation of new sensors.

In order to improve the radiation robustness of the hardware, a specific radiation testing strategy, needed to qualify radiation components was adopted. Thus, the RadMon has been qualified with the unique policy adopted at CERN in order to safely and reliably deploy the new system around the hot areas. The new version, the RadMon V6, has been developed to fulfill all the requirements of the previous version, solve the issues found in operation and improve the accuracy and resolution of the measurements carried out with the embedded sensors.

The new features of the RadMon V6 include the possibility to remotely select different configurations without needing an operator intervention in the tunnel, as it was the case for the previous version. The acquisition chain was improved in order to increase the resolution of the ADC and, consequently, of the analog sensors. Another ADC has been added to the RadMon and it is devoted to the self–diagnostic of the hardware.

All the components of the new version have been tested and qualified under radiation following the CERN policy. In this work the tests on the voltage regulators, FPGA, and the ADC have been reported and discussed. The measurement of the ENOB has been proposed as new testing methodology for ADCs, simulations and

measurements have been matched in order to record the SEUs and internal voltage reference drift. All the components have been tested separately and a system test has been carried out. Thanks to the right components selection the TID limit has been raised up more than a factor 3 with respect to the previous RadMon version.

Concerning the dosimetry, the accuracy and resolution of the TID measurements have been improved by means of an accurate ^{60}Co calibration of the RadFets. Two types of RadFets, with different gate oxide thickness (400 nm and 100 nm), have been calibrated. Two gate biasing conditions have been tested when the RadFet is irradiated: one with the gate at ground and the other at + 5 V. An increase of sensitivity of around a factor 3 has been measured using the +5 V biasing for both types of RadFets. It has been shown that the dose rate effects introduces an error smaller than 10%; and the test at two temperatures (25 °C and 40 °C) showed that the sensor response is not deeply affected by the absolute value of the temperature, provided that it does not change.

During the RadMon operation, a change of temperature is possible; therefore being the RadFet threshold voltage sensitive to the temperature, the measurement on temperature coefficient as function of the dose is necessary. The measurements showed that the temperature coefficient increases linearly with the dose. The linear fit for both the 400 nm and 100 nm can be easily implemented in software or in the firmware of the RadMon.

After the irradiation, the annealing rate of the 400 nm RadFet is higher than the 100 nm. This can have a big impact in operation when the accelerator is in shutdown and the information on the dose is partially lost.

The RadFets responses are strongly affected by the radiation environment; the applicability of the ^{60}Co calibration has been studied by means of several irradiation tests in experimental facilities at CERN and with a proton beam at different energies. Indeed, the latter showed that the thicker the RadFet oxide is the more sensitive to the incoming proton energies it is. This outcome has a strong impact in a mixed radiation field, like the one present at CERN, because of the wide energy spectra. For this reason the 100nm RadFet is preferred, which can have a resolution of 8×10^{-2} and 2.68×10^{-2} with GND and +5V bias respectevely.

The improvements on the dosimetry also include the HEH fluence measurements. Commercially available SRAM memories are used to measure the number of particles crossing the device. Two memories have been qualified and characterized: Toshiba and Cypress. They are from two different technology nodes and have a different cross sections. Several lots for the Toshiba memories have been characterized during these years. Two lots of SRAM memories have been qualified for the Cypress. The

Cypress memories have a proton cross section at 230 MeV, which is around a factor 10 higher than the Toshiba one. Moreover, it is demonstrated in this work that, being insensitive to the thermal neutrons, the Cypress, can achieve a higher accuracy for the HEH fluence evaluation in a mixed field environment. The Toshiba memories are sensitive to thermal neutrons since at low supply voltage (3 V) they have a high thermal neutron cross section. It was shown in the past the possibility to measure the thermal neutrons contribution by using the SRAM at two different voltages. This work showed how to get a simultaneous measurements of the HEH and thermal neutron fluence with a higher accuracy with respect to the previous RadMon version. In fact the HEH fluence resolution was improved by a factor $\sim$10.

The research of a more accurate and more sensitive device led to investigate a new type of silicon dosimeter, a floating gate dosimeter (FGDOS). This kind of sensor has been studied and characterized as a possible new sensor to be embedded in the future versions of the RadMon. The FGDOS, used in this work, embeds a floating gate structure and the readout circuit that converts the current variation from the bare sensor in a periodic signal. The working principle is based on the annhilation of the charges present on the floating gate rather than to the trapping of charges in the oxide. The sensor has been characterized in a CERN mixed radiation field test area, H4IRRAD, with ^{60}Co gamma and with protons to verify its dosimetric performances and also the susceptibility to single events and destructive events. The advantages of the sensor are its intrinsic re–usability and linearity; moreover, the sensor does not suffer of annealing because of its high charge retention. In this work the FGDOS sensitivity has been studied as a function of the cumulated TID. It was discovered that the sensor decreases its sensitivity with the cumulated TID beacause of the trapped charges in the field oxide. The dose rate effect has been studied too, though the phenomenon is not yet clear and further measurements are needed.

A physical model of the sensor has been developed to analytically extract the sensitivity of the device. This model, matched with the results from ^{60}Co and protons at different energies, permitted to accomplish the difficult measurement of the charge yield at low electric field and at room temperature.These preliminary results led to a concrete interest in the use of this kind of sensor in the next generation of the RadMon.

To date, the prototyping phase of the RadMon V6 is completed and a production of one hundred units has been installed in the LHC injection lines and in the new CERN test facility. Finally, the monitor will be adapted to achieve the standard space requirements to make it fly on a cubeSat mission.

List of Publications

The work performed during the doctoral thesis here presented has led to the publication of several IEEE TNS papers, some of which have been presented in international conferences. The published work is listed below.

- S. Danzeca, L. Dusseau, P. Peronnard, and G. Spiezia, "New Testing Methodology of an Analog to Digital Converter for the LHC Mixed Radiation Field" IEEE Transactions on Nuclear Science, 2013.

- S. Danzeca, J. Cesari, M. Brugger, L. Dusseau, A. Masi, A. Pineda, and G. Spiezia, "Characterization and Modeling of a Floating Gate Dosimeter with Gamma and Protons at Various Energies," IEEE Transactions on Nuclear Science, vol. 61, no. 6, pp. 3451Ű3457, Dec. 2014.

- S. Danzeca, G. Spiezia, M. Brugger, L. Dusseau, G. Foucard, R. G. Alia, P. Mala, A. Masi, P. Peronnard, J. Soltes, A. Thornton, and L. Viererbl, "Qualification and Characterization of SRAM Memories Used as Radiation Sensors in the LHC," IEEE Transactions on Nuclear Science, vol. 61, no. 6, pp. 3458Ű3465, Dec. 2014.

- G. Spiezia, P. Peronnard, A. Masi, M. Brugger, M. Brucoli, S. Danzeca, R. G. Alia, R. Losito, J. Mekki, P. Oser, R. Gaillard, and L. Dusseau, "A New RadMon Version for the LHC and its Injection Lines," IEEE Transactions on Nuclear Science, vol. 61, no. 6, pp. 3424Ű3431, Dec. 2014.

- J. Mekki, M. Brugger, S. Danzeca, L. Dusseau, K. Roed, and G. Spiezia, "Mixed Particle Field Influence on RadFET Responses Using Co-60 Calibration," IEEE Transactions on Nuclear Science, 2013.

- R. G. Alia, M. Brugger, S. Danzeca, V. Ferlet-Cavrois, C. Poivey, K. Roed, F. Saigne, G. Spiezia, S. Uznanski, and F. Wrobel, "SEE Measurements and Simulations Using Mono-Energetic GeV-Energy Hadron Beams," IEEE Transactions on Nuclear Science, vol. 60, no. 6, pp. 4142Ű4149, Dec. 2013.

- A. Masi, S. Danzeca, R. Losito, P. Peronnard, R. Secondo, and G. Spiezia, "A high precision radiation-tolerant LVDT conditioning module," Nuclear Instruments and Methods in Physics Research Section A: Accelerators, Spectrometers, Detectors and Associated Equipment, vol. 745, pp. 73Ű81, May 2014.

- G. Spiezia, M.Brugger, S. Danzeca, R.G. Alia, R. Gaillard, G.Foucard, P. Peronnard, R.Losito, A. Masi , J.Mekki, P.Oser, "Compendium of Radiation-Induced Effects for Candidate Particle Accelerator Electronics" , IEEE Radiation Effects Data Workshop (REDW), 2013

- S. Metzger, S. Hoeffgen, T. Kuendgen, M.Brugger, S. Danzeca, J.Mekki , G. Spiezia, P. Oser "Comprehensive Study of Parameters Influencing the Response of RadFETs", RADECs 2013 Conference Proceedings

- R. G. Alia, M. Brugger, S. Danzeca, V. Ferlet-Cavrois, C. Poivey, K. Roed, F. Saigne, G. Spiezia, S. Uznanski, and F. Saigne, "Energy Dependence of Tungsten-Dominated SEL Cross Sections," IEEE Transactions on Nuclear Science, vol. 61, no. 5, pp. 2718Ű2726, Oct. 2014.

- R. G. Alia, E. W. Blackmore, M. Brugger, S. Danzeca, V. Ferlet-Cavrois, R. Gaillard, J. Mekki, C. Poivey, K. Roed, F. Saigne, G. Spiezia, M. Trinczek, S. Uznanski, and F. Wrobel, "SEL Cross Section Energy Dependence Impact on the High Energy Accelerator Failure Rate," IEEE Transactions on Nuclear Science, vol. 61, no. 6, pp. 2936Ű2944, Dec. 2014.

Bibliography

[1] M. Brugger, R.G. Alia, S Danzeca, R. Denz, J. Mekki, P. Oser, P. Peronnard, J. P. De Carvalho Saraiva, G. Spiezia, Y. Thurel, and S. Uznanski. Radiation Effects, Calculation Methods and Radiation Test Challenges in Accelerator Mixed Particle and Energy Environments. *NSREC Short Course*, 2014.

[2] T. Wijnands, C. Pignard, and R. Tesarek. An on line radiation monitoring system for the LHC machine and experimental caverns, 2006.

[3] G. Spiezia, P. Peronnard, A. Masi, M. Brugger, M. Brucoli, S. Danzeca, R.G. Alia, R. Losito, J. Mekki, P. Oser, R. Gaillard, and L. Dusseau. A New RadMon Version for the LHC and its Injection Lines. *IEEE Transactions on Nuclear Science*, 61(6):3424–3431, December 2014.

[4] JEDEC. JEP133b, Guide for the Production and Acquisition of Radiation-Hardness- Assured Multichip Modules and Hybrid Microcircuits, 2005.

[5] T.R. Oldham and F.B. McLean. Total ionizing dose effects in MOS oxides and devices. *IEEE Transactions on Nuclear Science*, 50(3):483–499, 2003.

[6] Simon M. Sze and Kwok K. Ng. *Physics of Semiconductor Devices*. Wiley-Interscience, Hoboken, N.J, 3 edition edition, October 2006.

[7] P.J. McWhorter and P.S. Winokur. Simple technique for separating the effects of interface traps and trapped oxide charge in metal oxide semiconductor transistors. *Applied Physics Letters*, 48(2):133–135, 1986.

[8] F.W. Sexton and J.R. Schwank. Correlation of Radiation Effects in Transistors and Integrated Circuits. *IEEE Transactions on Nuclear Science*, 32(6):3975–3981, December 1985.

[9] J.F. Conley. Radiation Effects on Microelectronics course.

[10] D.F. Heidel, P.W. Marshall, K.A. LaBel, J.R. Schwank, K.P. Rodbell, M.C. Hakey, M.D. Berg, P.E. Dodd, M.R. Friendlich, A.D. Phan, C.M. Seidleck, M.R. Shaneyfelt, and M.A. Xapsos. Single-Event-Upset Test Results on 65 nm SOI SRAM. *IEEE Transactions on Nuclear Science*, 55(6):3394–3400, December 2008.

[11] ESA European Space Agency. ESCC25100, Single Event Effects Test Method and Guidelines - Issue 2, 2014.

[12] M. Moll. Radiation Damage in Silicon Particle Detectors - Microscopic Defects and Macroscopic Properties -, 1999.

[13] J.R. Srour and J.W. Palko. Displacement Damage Effects in Irradiated Semiconductor Devices. *IEEE Transactions on Nuclear Science*, 60(3):1740–1766, June 2013.

[14] K. Gill, G. Hall, and B. MacEvoy. Bulk damage effects in irradiated silicon detectors due to clustered divacancies. *Journal of Applied Physics*, 82(1):126–136, July 1997.

[15] F. Ravotti. Development and Characterisation of Radiation Monitoring Sensors for the High Energy Physics Experiments of the CERN LHC Accelerator, 2007.

[16] J. Mekki. Characterization and performance optimization of radiation monitoring sensors for high energy physics experiments at the CERN LHC and Super-LHC, 2009.

[17] M. Brugger and G. Spiezia. Strategy for Radiation Tolerance Assurance of the A&T electronic Equipment, 2014.

[18] CERN. Radiation working group RADWG, http://radwg.web.cern.ch/RadWG/.

[19] NASA. GSFC Radiation Data Base, http://radhome.gsfc.nasa.gov.

[20] Texas instrument. Texas instrument High-Reliability Radiation Data for Space, http://www.ti.com/lsds/ti/high-reliability/space/radiation-data.page.

[21] W. Hajdas, A. Zehnder, F. Burri, J. Bialkowski, L. Adams, B. Nickson, and R. Harboe-Sorensen. Radiation effects testing facility in PSI low energy OPTIS area. In *IEEE Radiation Effects Data Workshop, 1998*, pages 152–155, July 1998.

[22] M. Schippers and et all. The first year of operation of PSI's new SC cyclotron and beam lines for proton therapy, 2007.

[23] R. Garcia Alia. Radiation Fields in High Energy Accelerators and their impact on Single Event Effects, 2014.

[24] TRIUMF. TRIUMF, Proton Irradiation Facility, http://www.triumf.ca/pif-nif/proton-irradiation-facility.

[25] E.W. Blackmore. Operation of the TRIUMF (20-500 MeV) proton irradiation facility. In *Radiation Effects Data Workshop, 2000*, pages 1–5, 2000.

[26] L. Viererbl, J. Soles, Z. Lahodova, M. Kostal, and M. Vins. Horizontal Channel for Neutron Radiography and Tomography in LVR-15 Research Reactor. *Transactions of the RRFM/IGORR 2012*, 3:18–22, 2012.

[27] L. Viererbl, J. Soles, M. Vins, Z. Lahodova, and V. Klupak. Measurement of Thermal Neutron Beam Parameters in the LVR-15 Research Reactor. 15th meeting of the International Group On Research Reactors (IGORR 2013), Daejeon, Korea, 13. âĂŞ 18. 10. 2013, 2013. *15th meeting of the International Group On Research Reactors (IGORR 2013)*, 2013.

[28] Ralf Nolte and David J. Thomas. Monoenergetic fast neutron reference fields: I. Neutron production. *Metrologia*, 48(6):S263, December 2011.

[29] Ralf Nolte and David J. Thomas. Monoenergetic fast neutron reference fields: II. Field characterization. *Metrologia*, 48(6):S274, December 2011.

[30] CERN. CNRAD CERN Experimental Test Area for R2e Project, 2008. Available: http://radwg.web.cern.ch/ RadWG/Pages/CNRAD/cnrad_frame.htm: http://radwg.web.cern.ch/RadWG/Pages/CNRAD/cnrad_frame.htm.

[31] CERN. CNGS. CERN to Gran Sasso project: http://proj-cngs.web.cern.ch/proj-cngs/.

[32] Wijnands T. Functional Specification of the radiation monitoring for equipment in the LHC tunnel. https://edms.cern.ch/file/565013/0.2/LHC-PM-ES-0006-00-10.pdf.

[33] R.J. Tesarek et al. Experience from Fermilab. http://indico.cern.ch/conferenceDisplay.py?confId=a044378.

[34] Industrial communication networks: Profiles, 2007.

[35] CERN. CernFIP , http://www.ohwr.org/projects/cern-fip/wiki/WorldFIP, 2011.

[36] G. Penacoba, P. Alvarez, E. Gousiou, J. Palluel, J. Serrano, and E. Van der Bij. Design of an FPGA-based radiation tolerant agent for WorldFIP fieldbus. *Journal of Instrumentation*, 7(03):C03027, March 2012.

[37] G. Spiezia Oser, P. CEA Radiation Test Report LM317d2t, LM337imp, LM334, OPA2227, LM45, INA146, https://edms.cern.ch/document/1386559/1, 2013.

[38] E. Gousiou. nanoFIP Preliminary Radiation Tests - Test Report , https://edms.cern.ch/document/1144053/1.

[39] E. Gousiou. NanoFIP Large Scale Radiation Tests, https://edms.cern.ch/document/1184768/1.

[40] J.J. Wang, G. Kuganesan, N. Charest, and B. Cronquist. Biased-Irradiation Characteristics of the Floating Gate Switch in FPGA. In *2006 IEEE Radiation Effects Data Workshop*, pages 101–104, July 2006.

[41] Microsemi. Radiation-Tolerant ProASIC3 FPGAs Radiation Effects, http://www.microsemi.com/document-portal/doc_view/131374-radiation-tolerant-proasic3-fpgas-radiation-effects-report, 2010.

[42] Spiezia G. Danzeca S. ADC MAX11046 PSI report, https://edms.cern.ch/document/1171984/1, 2011.

[43] R. Velazco, R. Leveugle, and O. Calvo. Upset-like fault injection in VHDL descriptions: A method and preliminary results. In *2001 IEEE International Symposium on Defect and Fault Tolerance in VLSI Systems, 2001. Proceedings*, pages 259–267. IEEE, 2001.

[44] Melanie D. Berg, Stephen P. Buchner, Hak Kim, Mark Friendlich, Christopher Perez, Anthony M. Phan, Christina M. Seidleck, Kenneth A. Label, and Kirby Kruckmeyer. Enhancing Observability of Signal Composition and Error Signatures During Dynamic SEE Analog to Digital Device Testing. *IEEE Transactions on Nuclear Science*, 57(4):1958–1965, August 2010.

[45] T. L Turflinger and M. V Davey. Transient radiation test techniques for high-speed analog-to-digital converters. *IEEE Transactions on Nuclear Science*, 36(6):2356–2361, December 1989.

[46] K. Kruckmeyer, R. L Rennie, D. H Ostenberg, V. Ramachandran, and T. Hossain. Single Event Upset Characterization of GHz Analog to Digital Converters with Dynamic Inputs Using a Beat Frequency Test Method. In *2007 IEEE Radiation Effects Data Workshop*, pages 113–117. IEEE, July 2007.

[47] K. Kruckmeyer, R. L Rennie, and V. Ramachandran. Use of code error and beat frequency test method to identify single event upset sensitive circuits in a 1ghz analog to digital converter. In *9th European Conference on Radiation and Its Effects on Components and Systems, 2007. RADECS 2007*, pages 1–5. IEEE, September 2007.

[48] W.F. Heidergott, R. Ladbury, P.W. Marshall, S. Buchner, A.B. Campbell, R.A. Reed, J. Hockmuth, N. Kha, C. Seidleck, and A. Assad. Complex SEU signatures in high-speed analog-to-digital conversion. *IEEE Transactions on Nuclear Science*, 48(6):1828–1832, December 2001.

[49] S. Buchner, A. B Campbell, A. Sternberg, L. Massengill, D. McMorrow, and C. Dyer. Validity of using a fixed analog input for evaluating the SEU sensitivity of a flash analog-to-digital converter. *IEEE Transactions on Nuclear Science*, 52(1):462– 467, February 2005.

[50] IEEE. IEEE Std 1057-1994, Standard for Digitizing Waveform Recorders, Institute of Electrical and Electronic Engineers, 445. Technical report, 1994.

[51] S. Danzeca, L. Dusseau, P. Peronnard, and G. Spiezia. New Testing Methodology of an Analog to Digital Converter for the LHC Mixed Radiation Field. *IEEE Transactions on Nuclear Science*, Early Access Online, 2013.

[52] Holmes-Siedle Andrew. The space-charge dosimeter: General principles of a new method of radiation detection. *Nuclear Instruments and Methods*, 121(1):169–179, October 1974.

[53] Leonard Adams and Andrew Holmes-Siedle. The Development of an MOS Dosimetry Unit for Use in Space. *IEEE Transactions on Nuclear Science*, 25(6):1607–1612, December 1978.

[54] M. Soubra, J. Cygler, and G. Mackay. Evaluation of a dual bias dual metal oxide-silicon semiconductor field effect transistor detector as radiation dosimeter. *Medical Physics*, 21(4):567–572, April 1994.

[55] G.J. Brucker, S. Kronenberg, and T. Jordan. Tactical army dosimeter based on P-MOS single and dual gate insulators. In , *Second European Conference on Radiation and its Effects on Components and Systems, 1993.,RADECS 93*, pages 56–62, September 1993.

[56] M. Meguellati, F. Djeffal, D. Arar, T. Bendib, and L. Khettache. RADFET dosimeter design for environment monitoring applications. In *2012 24th International Conference on Microelectronics (ICM)*, pages 1–4, December 2012.

[57] F. Ravotti, M. Glaser, AB. Rosenfeld, M. Lerch, A G. Holmes-Siedle, and G. Sarrabayrouse. Radiation Monitoring in Mixed Environments at CERN: From the IRRAD6 Facility to the LHC Experiments. *IEEE Transactions on Nuclear Science*, 54(4):1170–1177, August 2007.

[58] J. M. Benedetto and H. E. Boesch. The Relationship between CO-60 and 10-keV X-Ray Damage in MOS Devices. *IEEE Transactions on Nuclear Science*, 33(6):1317–1323, 1986.

[59] R. C. Hughes. Hot Electrons in SiO2. *Physical Review Letters*, 35(7):449–452, August 1975.

[60] R. C. Hughes. Hole mobility and transport in thin SiO2 films. *Applied Physics Letters*, 26(8):436–438, April 1975.

[61] G.J. Brucker, E.G. Stassinopoulos, O. Van Gunten, L. S. August, and T.M. Jordan. The Damage Equivalence of Electrons, Protons, and Gamma Rays in MOS Devices. *IEEE Transactions on Nuclear Science*, 29(6):1966–1969, December 1982.

[62] G.J. Brucker, O. Van Gunten, E.G. Stassinopoulos, P. Shapiro, L. S. August, and T.M. Jordan. Recovery of Damage in Rad-Hard MOS Devices during and after Irradiation by Electrons, Protons, Alphas, and Gamma Rays. *IEEE Transactions on Nuclear Science*, 30(6):4157–4161, December 1983.

[63] E.G. Stassinopoulos, G.J. Brucker, O. Van Gunten, A R. Knudson, and T.M. Jordan. Radiation Effects on MOS Devices: Dosimetry, Annealing, Irradiation Sequence, and Sources. *IEEE Transactions on Nuclear Science*, 30(3):1880–1884, June 1983.

[64] E.G. Stassinopoulos, O. Van Gunten, G.J. Brucker, A R. Knudson, and T.M. Jordan. The Damage Equivalence of Electrons, Protons, Alphas and Gamma Rays in Rad-Hard MOS Devices. *IEEE Transactions on Nuclear Science*, 30(6):4363–4367, December 1983.

[65] T.R. Oldham. Analysis of Damage in MOS Devices for Several Radiation Environments. *IEEE Transactions on Nuclear Science*, 31(6):1236–1241, December 1984.

[66] E.G. Stassinopoulos, G.J. Brucker, and O. Van Gunten. Total-Dose and Dose-Rate Dependence of Proton Damage in MOS Devices during and after Irradiation. *IEEE Transactions on Nuclear Science*, 31(6):1444–1447, December 1984.

[67] W. J. Stapor, L. S. August, D. H. Wilson, T. R. Oldham, and K. M. Murray. Proton and Heavy-Ion Radiation Damage Studies in MOS Transistors. *IEEE Transactions on Nuclear Science*, 32(6):4399–4404, December 1985.

[68] R.L. Pease, Mayrant Simons, and P. Marshall. Comparison of pMOSFET total dose response for Co-60 gammas and high-energy protons. *IEEE Transactions on Nuclear Science*, 48(3):908–912, June 2001.

[69] P. Paillet, J. R. Schwank, M. R. Shaneyfelt, V. Ferlet-Cavrois, R. L. Jones, O. Flarrient, and E.W. Blackmore. Comparison of charge yield in MOS devices for different radiation sources. *IEEE Transactions on Nuclear Science*, 49(6):2656–2661, 2002.

[70] J.M. Aitken, D.J. DiMaria, and D.R. Young. Electron Injection Studies of Radiation Induced Positive Charge in MOS Devices. *IEEE Transactions on Nuclear Science*, 23(6):1526–1533, December 1976.

[71] T. P. Ma and Paul V. Dressendorfer. *Ionizing Radiation Effects in MOS Devices and Circuits*. Wiley, April 1989.

[72] F.B. McLean. A Direct Tunneling Model of Charge Transfer at the Insulator Semiconductor Interface in MIS Devices. *Harry Diamond Laboratories*, HDL-TR-1765, 1976.

[73] A. Modelli S. Manzini. Tunneling Discharge of Trapped Holes in Silicon Dioxide. *Elsevier Science Publishers*, Insulating Films in Semiconductors:p.112, 1983.

[74] T.R. Oldham, A.J. Lelis, and F.B. McLean. Spatial Dependence of Trapped Holes Determined from Tunneling Analysis and Measured Annealing. *IEEE Transactions on Nuclear Science*, 33(6):1203–1209, December 1986.

[75] Richard A. Reber and D.M. Fleetwood. Thermally stimulated current measurements of SiO2 defect density and energy in irradiated metal #x2010;oxide #x2010;semiconductor capacitors. *Review of Scientific Instruments*, 63(12):5714–5725, December 1992.

[76] J. G. Simmons and G. W. Taylor. High-Field Isothermal Currents and Thermally Stimulated Currents in Insulators Having Discrete Trapping Levels. *Physical Review B*, 5(4):1619–1629, February 1972.

[77] P.J. McWhorter, S.L. Miller, and W.M. Miller. Modeling the anneal of radiation-induced trapped holes in a varying thermal environment. *IEEE Transactions on Nuclear Science*, 37(6):1682–1689, December 1990.

[78] A Jaksic, K. Rodgers, C. Gallagher, and P. J. Hughes. Use of RADFETs for Quality Assurance of Radiation Cancer Treatments. In *2006 25th International Conference on Microelectronics*, pages 540–542, 2006.

[79] A Jaksic, G. Ristic, M. Pejovic, A Mohammadzadeh, and W. Lane. Characterisation of radiation response of 400 nm implanted gate oxide RADFETs. In *23rd International Conference on Microelectronics, 2002. MIEL 2002*, volume 2, pages 727–730, 2002.

[80] CERN. LHC statistics. 2012 http://lhc-statistics.web.cern.ch/LHC-Statistics/index.php#, 2012.

[81] A. Jaksic, G. Ristic, M. Pejovic, A. Mohammadzadeh, C. Sudre, and W. Lane. Gamma-ray irradiation and post-irradiation responses of high dose range RADFETs. *IEEE Transactions on Nuclear Science*, 49(3):1356–1363, 2002.

[82] S.H. Carbonetto, M.A. Garcia Inza, J. Lipovetzky, E.G. Redin, L.S. Salomone, and A. Faigon. Zero Temperature Coefficient Bias in MOS Devices. Dependence on Interface Traps Density, Application to MOS Dosimetry. *IEEE Transactions on Nuclear Science*, 58(6):3348–3353, December 2011.

[83] J. Mekki, M. Brugger, S. Danzeca, L. Dusseau, K. Roed, and G. Spiezia. Mixed Particle Field Influence on RadFET Responses Using Co-60 Calibration. *IEEE Transactions on Nuclear Science*, 60(4):2435–2443, August 2013.

[84] D. Lambert, J. Baggio, V. Ferlet-Cavrois, O. Flament, F. Saigne, B. Sagnes, N. Buard, and T. Carriere. Neutron-induced SEU in bulk SRAMs in terrestrial environment: Simulations and experiments. *IEEE Transactions on Nuclear Science*, 51(6):3435–3441, December 2004.

[85] R. Baumann. Silicon Amnesia - Terrestrial Effects. *Radecs Short Course*, 2001.

[86] R. Baumann. Soft errors in advanced computer systems. *IEEE Design Test of Computers*, 22(3):258–266, May 2005.

[87] R. Baumann, T. Hossain, E. Smith, S. Murata, and I. Kitagawa. Boron as a primary source of radiation in high density DRAMs. In *1995 Symposium on VLSI Technology, 1995. Digest of Technical Papers*, pages 81–82, June.

[88] C.S. Dyer, S.N. Clucas, C. Sanderson, A.D. Frydland, and R. T. Green. An experimental study of single event effects induced in commercial SRAMs by neutrons and protons from thermal energies to 500 MeV. In *Proceedings of the 7th European Conference on Radiation and Its Effects on Components and Systems, 2003. RADECS 2003*, pages 263–267, September.

[89] MoBl Cypress. http://www.cypress.com/?id=4&rID=26545.

[90] J.R. Schwank, P. E. Dodd, M. R. Shaneyfelt, J.A Felix, G. L. Hash, V. Ferlet-Cavrois, P. Paillet, J. Baggio, P. Tangyunyong, and E. Blackmore. Issues for single-event proton testing of SRAMs. *IEEE Transactions on Nuclear Science*, 51(6):3692–3700, December 2004.

[91] Ruben Garcia Alia, Ewart W. Blackmore, Markus Brugger, Salvatore Danzeca, Veronique Ferlet-Cavrois, Remi Gaillard, Julien Mekki, Christian Poivey, Ketil Roed, Frederic Saigne, Giovanni Spiezia, Michael Trinczek, Slawosz Uznanski, and Frederic Wrobel. SEL Cross Section Energy Dependence Impact on the High Energy Accelerator Failure Rate. *IEEE Transactions on Nuclear Science*, 61(6):2936–2944, December 2014.

[92] R.G. Alia, M. Brugger, S. Danzeca, V. Ferlet-Cavrois, C. Poivey, K. Roed, F. Saigne, G. Spiezia, S. Uznanski, and F. Saigne. Energy Dependence of Tungsten-Dominated SEL Cross Sections. *IEEE Transactions on Nuclear Science*, 61(5):2718–2726, October 2014.

[93] M.A. Clemens, B.D. Sierawski, K.M. Warren, M.H. Mendenhall, N.A. Dodds, R.A. Weller, R.A. Reed, P.E. Dodd, M.R. Shaneyfelt, J.R. Schwank, S.A. Wender, and R.C. Baumann. The Effects of Neutron Energy and High-Z Materials on Single Event Upsets and Multiple Cell Upsets. *IEEE Transactions on Nuclear Science*, 58(6):2591 –2598, December 2011.

[94] K. Roeed, M. Brugger, D. Kramer, P. Peronnard, C. Pignard, G. Spiezia, and A Thornton. Method for Measuring Mixed Field Radiation Levels Relevant for SEEs at the LHC. *IEEE Transactions on Nuclear Science*, 59(4):1040–1047, August 2012.

[95] D. Kramer, M. Brugger, V. Klupak, C. Pignard, K. Roeed, G. Spiezia, L. Viererbl, and T. Wijnands. LHC RadMon SRAM Detectors Used at Different Voltages to Determine the Thermal Neutron to High Energy Hadron

Fluence Ratio. *IEEE Transactions on Nuclear Science*, 58(3):1117 –1122, June 2011.

[96] T. Wijnands and C. Pignard. Radiation response of RADMON sensors. https://edms.cern.ch/document/1226507/1, 2005.

[97] L.Z. Scheick and G.M. Swift. Dose and microdose measurement based on threshold shifts in MOSFET arrays in commercial SRAMs. *IEEE Transactions on Nuclear Science*, 49(6):2810–2817, December 2002.

[98] D. Kramer, M. Brugger, V. Klupak, C. Pignard, K. Roeed, G. Spiezia, L. Viererbl, and T. Wijnands. LHC RadMon SRAM Detectors Used at Different Voltages to Determine the Thermal Neutron to High Energy Hadron Fluence Ratio. *IEEE Transactions on Nuclear Science*, 58(3):1117 –1122, June 2011.

[99] K. Roeed, M. Brugger, and G. Spiezia. An overview of the radiation environment at the LHC in light of R2e irradiation test activities, September 2011.

[100] K. Kahng and S.M. Sze. A floating gate and its application to memory devices. *IEEE Transactions on Electron Devices*, 14(9):629–629, September 1967.

[101] M. Holler, Simon Tam, H. Castro, and R. Benson. An electrically trainable artificial neural network (ETANN) with 10240 'floating gate' synapses. In , *International Joint Conference on Neural Networks, 1989. IJCNN*, pages 191–196 vol.2, 1989.

[102] Meinhard Knoll and Dietrich Braunig. MOS dosimeter, November 1988. U.S. Classification 257/428, 257/E31.091, 257/316, 257/E31.085, 250/370.07, 250/370.14; International Classification G01T1/02, H01L31/119, H01L31/113; Cooperative Classification H01L31/119, H01L31/1136; European Classification H01L31/113C, H01L31/119.

[103] Chenming Hu. Lucky-electron model of channel hot electron emission. In *Electron Devices Meeting, 1979 Internationa*, volume 25, pages 22–25, 1979.

[104] N M Ravindra and J Zhao. Fowler-Nordheim tunneling in thin SiO_2 films. *Smart Materials and Structures*, 1(3):197–201, September 1992.

[105] G. Cellere, A. Paccagnella, A. Visconti, M. Bonanomi, A. Candelori, and S. Lora. Effect of different total ionizing dose sources on charge loss from programmed floating gate cells. *IEEE Transactions on Nuclear Science*, 52(6):2372–2377, December 2005.

[106] G. Cellere, A Paccagnella, A Visconti, M. Bonanomi, P. Caprara, and S. Lora. A model for TID effects on floating Gate Memory cells. *IEEE Transactions on Nuclear Science*, 51(6):3753–3758, December 2004.

[107] A. Thomsen and M.A. Brooke. A floating-gate MOSFET with tunneling injector fabricated using a standard double-polysilicon CMOS process. *IEEE Electron Device Letters*, 12(3):111–113, 1991.

[108] J. Kassabov, N. Nedev, and N. Smirnov. Radiation dosimeter based on floating gate MOS transistor. *Radiation Effects and Defects in Solids*, 116(1-2):155–158, 1991.

[109] N.G. Tarr, K. Shortt, Yanbin Wang, and I. Thomson. A sensitive, temperature-compensated, zero-bias floating gate MOSFET dosimeter. *IEEE Transactions on Nuclear Science*, 51(3):1277 – 1282, June 2004.

[110] F. Saigne, L. Dusseau, J. Fesquet, J. Gasiot, R. Ecoffet, J-P David, R.D. Schrimpf, and K.F. Galloway. Experimental validation of an accelerated method of oxide-trap-level characterization for predicting long term thermal effects in metal oxide semiconductor devices. *IEEE Transactions on Nuclear Science*, 44(6):2001–2006, December 1997.

[111] T.R. Oldham and J.M. McGarrity. Comparison of Co-60 Response and 10 KeV X-Ray Response in MOS Capacitors. *IEEE Transactions on Nuclear Science*, 30(6):4377–4381, 1983.

[112] George A. Ausman. Field Dependence of Geminate Recombination in a Dielectric Medium. page 20, 1986.

[113] P. Paillet, J. R. Schwank, M. R. Shaneyfelt, V. Ferlet-Cavrois, R. L. Jones, O. Flarrient, and E.W. Blackmore. Comparison of charge yield in MOS devices for different radiation sources. *IEEE Transactions on Nuclear Science*, 49(6):2656–2661, 2002.